Development Of Alignment And Phasing System For India's Large Segmented Mirror Telescope

A Thesis
Submitted for the Degree of
Doctor of Philosophy (Technology)

Submitted by
RADHIKA DHARMADHIKARI

Department of Applied Optics & Photonics
University of Calcutta

2024

Dedicated to my Motherland
Bharat

Abstract

The segmented mirror technology has become the preferred choice for building moderate to large-size optical telescopes. For the segmented primary mirror to function like a single monolithic mirror, each segment must be co-aligned, co-focused, and co-phased. In any segmented mirror telescope, these tasks are accomplished by an Alignment and Phasing System (APS). The India's upcoming large optical-NIR telescope, will use a segmented primary mirror. This thesis explores the technology required to align and phase its mirror segments. To begin with, an end-to-end Python-based code is developed to carry out very detailed simulations on co-alignment, co-focusing, and co-phasing. The code generates realistic images for the telescope + APS system. The simulation results are used to estimate the achievable measurement accuracy by the APS. As a part of the thesis work, a Segment Alignment Device (SAD) has also been designed, developed, and tested for the one-meter class Prototype Segmented Mirror Telescope (PSMT).

For any large segmented mirror telescope to achieve diffraction-limited performance, its mirror segments must be phased with very high accuracy (in the order of a few nanometers). Phasing the mirror segments is one of the most challenging tasks, and as a part of this project, we have explored two different phasing techniques: the Dispersed Fringe Sensor (DFS) and the Optical Transfer Function (OTF) based phasing. For both techniques, we have first performed extensive simulations to test their feasibility under realistic conditions. And then, the simulation results are verified through laboratory experimentation. From our research work we have shown that the DFS, which is conventionally considered as a coarse phasing technique, can also be used for fine phasing. In laboratory experimentation, we have achieved a piston measurement accuracy of 2–3 nm. Similarly, we have explored the OTF-based phasing for which we achieved a piston measurement accuracy of 1.5-18nm through laboratory experiments. Through our extensive simulations and laboratory experiments, we have confirmed that both DFS and OTF can be used for coarse and fine phasing of mirror segments, thus eliminating the need to use two different phasing techniques as is done conventionally.

This thesis explores all three aspects of an APS and aims to understand and improve the alignment and phasing techniques so that this knowledge can be later implemented on the India's large segmented mirror telescope.

Contents

List of Publications

Refereed Journal Articles (related to this thesis)

1. **Building a large affordable optical-NIR telescope (I): an alternate way to handle segmented primary mirror**
   Radhika Dharmadhikari, Padmakar Parihar, Annu Jacob
   Experimental Astronomy, Volume 56, pages 569–604, (2023)
   DOI: https://doi.org/10.1007/s10686-023-09900-0

2. **Development of an alignment device for the Prototype Segmented Mirror Telescope**
   Radhika Dharmadhikari, Padmakar Parihar, Mohammed Muthahar Rafeeq Ahmed, Govinda Koravangala Venkatapathaiah, Madan Mohan Kemkar, Himanshu Kunjam
   Journal of Astronomical Telescopes, Instruments, and Systems (JATIS), Volume 10, Issue 1, 019002 (March 2024)
   DOI: https://doi.org/10.1117/1.JATIS.10.1.019002

3. **Dispersed Fringe Sensor for coarse and fine phasing of segmented mirrors**
   Radhika Dharmadhikari and Padmakar Parihar
   Under Preparation

Refereed Journal Articles (not related to this thesis)

1. **Bisymmetric pupil modification deconvolution strategy for differential optical transfer function (dOTF) wavefront sensing**
   Patrice Martinez and **Radhika Dharmadhikari**
   Astronomy and Astrophysics, Volume 680, December 2023
   DOI: https://doi.org/10.1051/0004-6361/202348435

2. **Design requirements of a Spectropolarimeter for solar Extreme-ultraviolet Observations and characterization of K-mirror based on Brewster's angle**
   Raveena Khan, **Radhika Dharmadhikari**, Harsh Mathur, Nagaraju K, Sinchana R. Jain, D. V. S. Phanindra, K Sagayanathan
   Accepted at Applied Optics

Conference Proceedings

1. **Simulation and experimental study of the OTF based alignment and phasing of segmented mirrors**
   Radhika Dharmadhikari and Padmakar Parihar
   Proc. SPIE 13094, Ground-based and Airborne Telescopes X, 1309427 (28 August 2024); DOI: https://doi.org/10.1117/12.3018465

2. **Differential optical transfer function (dOTF) wavefront sensing with the SPEED test bed**
   Radhika Dharmadhikari, Patrice Martinez, Carole Gouvret, Aurélie Marcotto, Alain Spang, Mathilde Beaulieu, Charles Sallard
   Proc. SPIE 13097, Adaptive Optics Systems IX, 130973Q (27 August 2024); DOI: https://doi.org/10.1117/12.3019044

3. **Optical design of FOSC and wide field aberration corrector for the prototype segmented mirror telescope**
   Radhika Dharmadhikari, Annu Jacob, Padmakar Parihar
   Proc. SPIE 12638, Women in Optics and Photonics in India 2022, 1263807 (11 May 2023); DOI: https://doi.org/10.1117/12.2669796

4. **Revisiting optical transfer function-based focal plane wavefront sensors for correcting non-common path aberrations**
   Patrice Martinez, **Radhika Dharmadhikari**, Alain Spang
   Proc. SPIE 13097, Adaptive Optics Systems IX, 130973P (27 August 2024); DOI: https://doi.org/10.1117/12.3019041

5. **Study on segmentation and alignment related effects in a 10m class telescope**
   Annu Jacob, Padmakar Singh Parihar, Melvin K James, **Radhika Dharmadhikari**
   Proc. SPIE 12182, Ground-based and Airborne Telescopes IX, 1218224 (29 August 2022); DOI: https://doi.org/10.1117/12.2629948

6. **Design and development of a mirror support system for prototype segmented mirror telescope**
   KV Govinda, Padmakar Parihar, PMM Kemkar, Abhishek Goudar, DS Sandeep, R Muthahar, K Sagayanathan, **Radhika Dharmadhikari**, PH Divya
   Proc. SPIE 12182, Ground-based and Airborne Telescopes IX, 121821F (29 August 2022); DOI: https://doi.org/10.1117/12.2628875

Presentations

Oral

1. *Simulation and Experimental study of the OTF based alignment and phasing of segmented mirrors* at SPIE Astronomical Telescopes + Instrumentation, Yokohama, Japan, June 2024

2. *Experimentation on the Dispersed Fringe Sensor based phasing of mirror segments* at Network of Young Researchers in Instrumentation for Astronomy (NYRIA), Laboratoire d'Astrophysique de Marseille, Marseille, France, November 2023

3. *Development of an Alignment device for the Prototype Segmented Mirror Telescope* at the 41^{st} Meeting of Astronomical Society of India, IIT Indore, March 2023

4. *Phasing Segmented Primary Mirror using the Dispersed Fringe Technique* at the 39^{st} Meeting of Astronomical Society of India, Online, February 2021

5. *Alignment and Phasing of Large Segmented Mirror Telescopes* at Network of Young Researchers in Instrumentation for Astronomy (NYRIA), Online, October 2020

Posters

1. *Co-Phasing of Segmented Mirrors using the Dispersed Fringe Sensor* at National Space Science Symposium (NSSS), Goa University, February 2024

2. *Optical Design of FOSC and Spherical Aberration Corrector for the Prototype Segmented Mirror Telescope* at Raman Research Institute, Bangalore, December 2022

3. *Differential optical transfer function (dOTF) wavefront sensing with the SPEED test-bed* at SPIE Astronomical Telescopes + Instrumentation, Yokohama, Japan, June 2024

4. *Revisiting optical transfer function-based focal plane wavefront sensors for correcting noncommon path aberrations* at SPIE Astronomical Telescopes + Instrumentation, Yokohama, Japan, June 2024

List of Figures

List of Tables

List of Abbreviations

ADU Analog to Digital Units

APS Alignment and Phasing System

ARIES Aryabhatta Research Institute of Observational Sciences

BARC Bhabha Atomic Research Centre

BLDC Brushless Direct Current

CAD Computer Aided Design

CCD Charge Coupled Device

CMOS Complementary Metal Oxide Semi-conductor

DFA-LSR Dispersed Fringe Accumulation based Left Subtract Right

DFS Dispersed Fringe Sensor

DOT Devasthal Optical Telescope

ELT Extremely Large Telescope

FWHM Full Width at Half Maximum

GMT Giant Magellan Telescope

GTC Gran Telescopio Canarias

GUI Graphical User Interface

HCT Himalayan Chandra Telescope

HET Hobby-Eberly Telescope

HFOSC Himalayan Faint Object Spectrograph and Camera

IAO Indian Astronomical Observatory

IBF Ion Beam Figuring

IIA Indian Institute of Astrophysics

IUCAA Inter-University Centre for Astronomy and Astrophysics

JWST James Webb Space Telescope

LAMOST Large Sky Area Multi-Object Fiber Spectroscopic Telescope

LASER Light Amplification by Stimulated Emission of Radiation

LED Light Emitting Diode

M1CS Primary Mirror Control System

MACE Major Atmospheric Cherenkov Experiment Telescope

MMT Multiple Mirror Telescope

MOSFET Metal Oxide Semi-conductor Field Effect Transistor

MPP Main Peak Position

MTF Modulation Transfer Function

NRT New Robotic Telescope

NTT New Technology Telescope

OPD Optical Path Difference

OTF Optical Transfer Function

PCS Phasing Camera System

PRL Physical Research Laboratory

PRNU Photo Response Non-Uniformity

PSF Point Spread Function

PSMT Prototype Segmented Mirror Telescope

PSoC Programmable System on Chip

PTF Phase Transfer Function

PWM Pulse Width Modulation

QE Quantum Efficiency

RC Ritchey Chretien

ROC Radius Of Curvature

RMS Root Mean Square

SAD Segment Alignment Device

SALT South African Large Telescope

SH Shack-Hartmann

SMT Segmented Mirror Technology

SNR Signal to Noise Ratio

TIFR Tata Institute of Fundamental Research

TMT Thirty Meter Telescope

UPSO Uttar Pradesh State Observatory

VBT Vainu Bappu Telescope

VCM Voice Coil Motor

VLT Very Large Telescope

Chapter 1
Introduction

Our country, India, historically known as *Bharat*, has a rich tradition of knowledge. The Sanskrit word *Bharat* can be broken down as *Bha-* meaning light or knowledge and *Rata-* meaning devoted to. Thus, Bharat translates to a nation that is devoted to the search of knowledge. Our country has a rich heritage in astronomy; several ancient Indian astronomers/ mathematicians have devoted their lives towards understanding the true nature of this universe. Ancient India has had several genius mathematicians and astronomers, such as Aryabhatta, Varahmihir, Bhaskaracharya, and many more. In modern times, this legacy of our country is being taken forward by several astronomical institutes spread all across the country. Among these institutions, the Indian Institute of Astrophysics (IIA) is the oldest astronomical institute in modern India, which traces its roots back to the Madras Observatory which was established in 1792.

For astronomy, the most essential instrument required is the telescope. Currently, we have several telescopes in our country, the largest one being the Devasthal Optical Telescope (DOT), which is 3.6m in size. To achieve better resolution and sensitivity, we need even larger telescopes. Therefore, considering India's growing astronomical community, IIA proposed a large telescope project in the year 2007. The upcoming large telescope will be 6-10m in size and will use Segmented Mirror Technology (SMT). To achieve the desired diffraction-limited image quality with the segmented mirror, it is important to align the primary mirror segments very precisely to the orders of a very small fraction of the observing wavelength. To achieve this, a specialised instrument called the Alignment and Phasing System (APS) is required, which defines the reference positions for the segments. Once the alignment process is completed, then the primary mirror control system (M1CS) maintains the segment positions over a period of several weeks. Compared to a monolithic primary, the segmented mirror technology provides ease of manufacturing and maintenance; however it comes with additional challenges. Therefore, considering the upcoming India's large segmented mirror telescope project, we explore the alignment and phasing related aspects of the segmented mirrors, through this thesis work.

1.1 Optical Astronomy in India

The earliest records of Astronomy in India are found in the *Vedas*, where astronomical observations were used as a precise source of timekeeping. However, the invention of telescopes revolutionised astronomy, and the earliest record of the use of a telescope in India dates back to 1651 by Jeremiah Shakerley, who observed the transit of Mercury from Surat (Hasan, 2014). Later, in 1792, the East India Company established an observatory at Madras. One of the significant discoveries of this observatory was the discovery of Helium. The helium element was discovered here through solar observations during the eclipse of August 1868. Towards the end of 19^{th} century, the operations from the Madras Observatory were shifted to the Kodaikanal Observatory. The first observations were commenced at Kodaikanal in 1901. In 1945, the Government of India appointed a committee of scientists to examine and recommend the steps towards the development of astronomical studies in our country. Around the time of independence, this committee envisioned the idea of having a 100inch telescope in India (Bhattacharyya and Rajan, 1992). In the 1960s, M. K. Vainu Bappu initiated a site surveying project for the proposed 100inch telescope in southern India; simultaneously, efforts towards technology development were also started. In 1972, a 1m size Zeiss telescope was installed in Kavalur. This was also the time around which the Astrophysical Observatory of Kodaikanal was transformed into an autonomous research Institute called the Indian Institute of Astrophysics (IIA). After several years of technology development by M.K. Vainu Bappu and his team, the 93inch Vainu Bappu Telescope (VBT) was inaugurated in 1986. After independence, the development of astronomical facilities was not confined to IIA alone; several other Indian institutions, such as Uttar Pradesh State Observatory (UPSO), Osmania University, PRL, IUCAA, TIFR and BARC, also contributed towards enriching astronomical resources. At present, we have about a dozen 1-4m size optical telescopes equipped with verities of instruments in India.

During the 1980s, several 4-6m size telescopes were built successfully all around the world (Schroeder, 1987), and by the end of 90s multiple 8-10m size telescopes such as VLT, Subaru, Keck and HET were operational. This inspired Indian astronomers to find the most suitable site within the country and install a large optical telescope there. Hence, the hunt for a favourable site in the trans-Himalayan regions was initiated in late 90s. As a result of this site survey, Hanle, Ladakh, was identified as one of the most suitable sites for hosting a large optical and near-infrared telescope. The Indian Astronomical Observatory (IAO) was then established, and the 2m size Himalayan Chandra Telescope (HCT) saw its first light in the year 2000 as a precursor to the larger facility. Almost two decades of operation of the HCT telescope, coupled with extensive site characterization efforts using various instruments, have strongly confirmed that IAO Hanle is one of the best astronomical sites in the world (Sharma

et al., 2017; Surendran et al., 2018).

1.2 India's Large Optical NIR Telescope Project

Presently, the largest optical telescope in India is the 3.6m Devasthal Optical Telescope (DOT) of ARIES, Nainital. For more than two decades, international communities have been doing forefront research using 8-10m class telescopes equipped with state-of-the-art back-end instruments. Therefore, to keep pace with the global astronomical communities and to cater the needs of Indian astronomers, India requires its own large optical near infrared telescope installed at the best available site within the country. In the 1990s, IIA proposed a 6.5m telescope, considering this, site surveying was started in the upper and trans-Himalayan regions. As a result, Hanle, Ladakh was identified as a suitable site, and the IAO was established there, which now hosts the 2m HCT. The successful operation of the HCT since 2003 and the establishment of the necessary infrastructure at IAO inspired IIA astronomers to revive the project of building a 10m class large optical telescope in 2007 (Anupama et al., 2022). As the proposed telescope will be 6-10m in size, hence the segmented mirror technology is adopted. At the same time, in 2010, India proposed to join the 30m TMT project, with an aim to give an impetus for Indian astronomers to be able to participate in forefront research areas. The Indian partnership with TMT has helped in the development of several aspects of the segmented mirror technology such as, segment polishing, design and fabrication of segment support assembly, in the country. However, in order to build a complete telescope, it is important to understand, develop, and test all the aspects of a segmented mirror telescope. Therefore, before embarking on the large and expensive segmented mirror telescope, a prototype telescope project is taken up so that the complexities of the segmented mirror technology can be understood through laboratory experimentation. Hence, in 2015, the Prototype Segmented Mirror Telescope (PSMT) (Parihar et al., 2018) project was started as a technology demonstrator for the upcoming large telescope.

In addition to conducting R&D on segmented mirror technology, parallel efforts have also been put towards conceptualising the opto-mechanical design aspects of the large telescope. The optical design of the telescope is not yet finalised, and considering the science cases as well as budgetary constraints, it is going through several changes. The initial design of the telescope is a RC based optical design, with a 10m size primary mirror, which comprises 60 hexagonal segments of 1.4m size each (Anupama et al., 2022). This design would cover a field of view of 10arc-min with a telescope focal ratio of F/15. The proposed first light instruments for this 10m size telescope include, a seeing limited 0.3–1μm low-medium multi-object spectrometer camera, a 0.9–5μm spectrometer camera and a high resolution (R$\approx$50000–120000) spectrometer in the 0.3–1μm range(Anupama et al., 2022).

Another alternate design option now being explored is a massively multiplexed wide-field telescope suitable for spectroscopic and imaging surveys. To save the cost as well as construction time, the size of the telescope is reduced to 6.2m, and the primary mirror is expected to be made of 18 segments (Deshmukh et al., 2024). Figure 1.1 shows the three dimensional models of the 10m and 6.2m designs of the telescope. The new design is a wide-field optical IR spectroscopic survey telescope. The telescope is designed to provide a 2.5^o field of view, achieved through a system of wide-field corrector lenses. The telescope provides a F/3.61 beam which is suitable for directly feeding optical fibers. This would allow the use of integral field spectrographs to record the spectra in a broad range of resolutions (R≈3000-40000). This telescope can work in two configurations : Prime and Cassegrain mode.

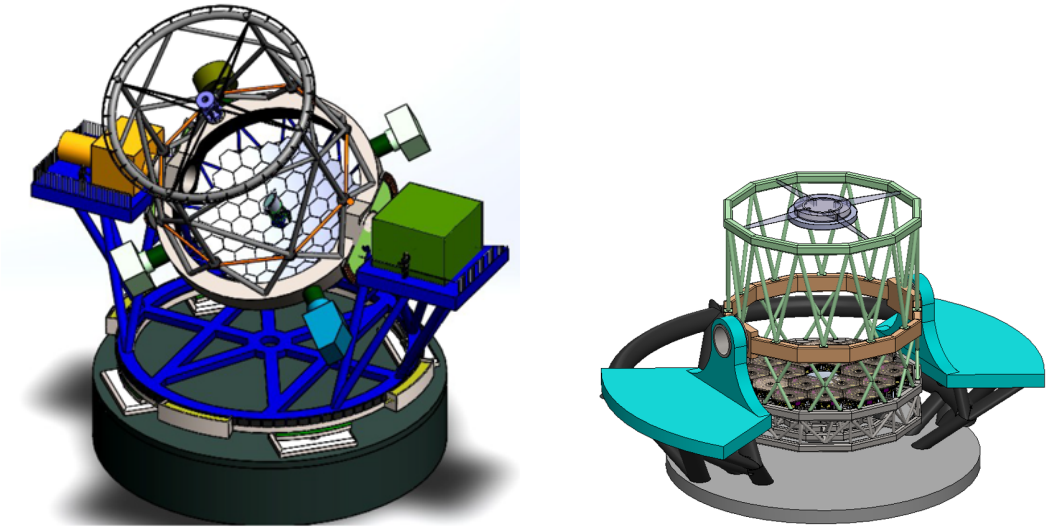

Figure 1.1: 3-D models of the India's proposed large segmented mirror telescope. Initial design with 10m primary mirror (left). New, alternate design with 6.2m primary mirror (right, *Credit:* Prasanna Deshmukh).

Since the telescope optical design is not yet finalized, therefore, in this thesis work we have considered the 10m size telescope design, which is described in detail in section 2.2. The alignment and phasing is an important aspect of the segmented mirror telescope and we have tried to explore and understand it through this thesis work.

1.3 Segmented Mirror Telescopes

The diameter of the telescope plays the most important role as it decides the sensitivity as well as the resolution of the telescope. For a telescope of diameter D, under seeing limited case, the image resolution obtained is decided by the atmospheric seeing or the Fried parameter (r_o) and the image FWHM is λ/r_o and the light collecting

power is proportional to D^2. However, with advancement in adaptive optics, the diffraction-limited resolution of λ/D can be achieved, and the sensitivity improves as D^4. Thus, D is one of the most critical parameters, and in order to have higher resolution and better sensitivity, one needs to build larger telescopes. However, manufacturing and maintaining a monolithic primary mirror larger than 8m, introduces several challenges and risks. The key challenges are as stated (Oswalt and McLean, 2013): (i) Manufacturing large mirrors is expensive as it requires a larger vacuum chamber for coating, and tool costs and fabrication costs are also higher; (ii) The probability of mirror breakage increases; (iii) Larger mirrors are subject to larger deformations and hence large optical aberrations from thermal and mechanical changes; (iv) Shipping a very large mirror to the observatory site may be impractical.

Considering the high risks and difficulties associated with a large monolithic mirror, using a segmented primary mirror is more feasible for large telescopes. Therefore, instead of using one large mirror, the primary mirror is made using multiple smaller mirrors called the segments. Although, the segmented mirror technology provides an ease of manufacturing and maintenance of the primary mirror, however, it also imposes a few challenges, which are listed below (Oswalt and McLean, 2013),

- Due to a large number of segments, the number of components increases.
- Figuring/Polishing the segments is difficult because they are off-axis sections of a parent conical figure and are not locally axis-symmetric.
- Inter-segment gaps lead to increased diffraction effects and thermal background effects.
- The segments must be optically aligned very precisely, and their positions must be maintained over time.

These challenges impose a requirement for a few extra sub-systems that help to achieve and maintain the image quality with the segmented primary mirror, which is discussed in detail in the section 1.5.

The first recorded use of segmented optics for astronomy was by Horn d'Arturo in Italy. In 1952, he made a 1.8m mirror out of 61 hexagonal segments (Bonoli, 2018). Later, the 6.5m Multiple Mirror Telescope (MMT) (Beckers, Ulich, and Williams, 1982) initially used six 1.8m telescopes on a common mount, which follows the idea of segmented mirrors to some extent. All these developments further led to the conceptual design study for a 10m segmented mirror telescope for the Keck observatory (Nelson et al., 1985). The first Keck telescope became operational in 1993, and the Keck 2 was completed in 1996. The success of the twin Keck telescopes gave birth to several other moderate (4-6m) as well as large (10m) size telescopes that came up around the early 2000s. These include the HET (Ramsey et al., 1998), SALT (Buckley et al., 2006), GTC (Alvarez, Rodríguez Espinosa, and Sánchez, 1998) and

LAMOST (Cui et al., 2010). Moderate-size telescopes such as SEIMEI (Nagata and Kurita, 2020) and NRT (Gutiérrez et al., 2021) have also adopted the segmented mirror technology. The excellent performance achieved by these 10m size telescopes led to further extension of the telescope sizes, and today, we have landed in the era of extremely large mega telescopes (Andersen et al., 2003; Dierickx et al., 2003). The upcoming mega telescopes such as the Thirty Meter Telescope (TMT)(Nelson and Sanders, 2006), Giant Magellan telescope (GMT) (Johns, 2006) and the Extremely Large Telescope (ELT) (Gilmozzi and Spyromilio, 2008), all have effective primary mirror diameter of 24-40m. Achieving such a large size of primary mirror would have been impossible without using the segmented mirror technology.

1.4 Segmented Mirror Technology

The segmented mirror telescope uses multiple smaller mirror segments that work together like a large monolithic primary mirror. To achieve this, the primary task is to align all the segments precisely so that they follow the profile of the parent monolithic primary mirror. This requires defining as well as maintaining the segment positions to the orders of a few nano-meters. Each mirror segment, which can be considered as a rigid body, is subjected to six degrees of freedom (three translation and three rotation). Thus, the segmented mirror technology requires two important elements: the Alignment and Phasing System (APS), which helps to align all the mirror segments precisely, and the Primary Mirror Control System (M1CS) for maintaining the alignment.

1.4.1 Alignment and Phasing System (APS)

The APS is an optical instrument that measures the tip-tilt and piston errors of individual segments optically. This is done by using a suitable wavefront sensing technique that provides the segment tip-tilt and piston errors in the form of wavefront errors. Based on the telescope requirements, the APS may use any one of the wavefront sensing techniques. The APS is primarily responsible for defining the reference position for the tip-tilt and piston, required to achieve the diffraction-limited image quality. The in-depth exploration of alignment and phasing schemes is the main objective of the current thesis work, and a brief overview of different techniques opted to develop an APS can be found in section 1.5.

1.4.2 M1CS

Once the desired segment positions are known from the APS, then the next task is to maintain these positions with time over varying external disturbances such as gravity and winds. This task of maintaining the primary mirror shape is carried out by the

primary mirror control system or the M1CS. The M1CS is an electronic control system which consists of high precision actuators and edge sensors. Each hexagonal segment is equipped with three actuators on its back surface, which facilitate the movement of the segment along three degrees of freedom, i.e., tip, tilt, and piston. Figure 1.2 shows the placement of the M1CS components on the segments. The edge sensors are placed on the inter-segment regions between two segments. Two edge sensors are mounted on each inter-segment gap; these edge sensors measure the displacement between the two segments and, hence, measure the segment positions precisely. In real-time, the measurement from the edge sensors is given as feedback to the M1CS and then the actuators are used to correct the segment tip-tilt and piston errors. Depending on the efficiency and accuracy of the M1CS, the primary mirror alignment can be maintained up to a period of a few weeks to a month, after which the alignment and phasing process has to be performed again by the APS.

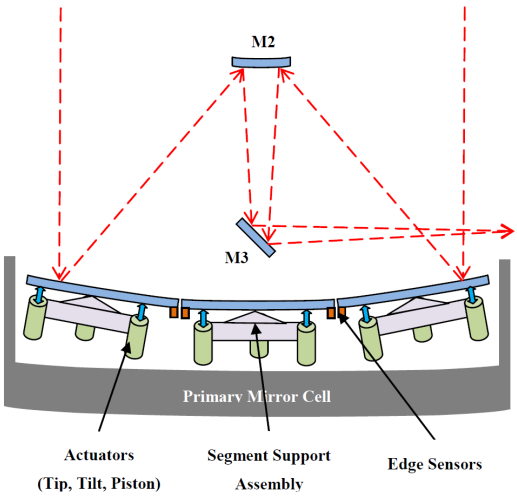

Figure 1.2: Schematic showing the components of the M1CS, including actuators, edge sensors and the segment support assembly. *Credit:* Deshmukh et al. (2016).

1.4.3 Challenges with Segmented Mirror Technology

Achieving the desired alignment accuracy and then maintaining the shape of the segmented primary is the most challenging task. Telescopes such as the HET (Palunas et al., 2006) and SALT have experienced several challenges in maintaining the segment alignment using the M1CS. For example, for the SALT, the initial design of the M1CS used capacitive edge sensors, which showed a degradation in performance under varying environmental conditions. Later on, these edge sensors were replaced by inductive edge sensors to meet the desired image quality requirements (Gajjar et al., 2006; Buous, Menzies, and Gajjar, 2008). Apart from the primary mirror control, phasing the mirror segments with nano-metric accuracy is also a challenging task.

The twin Keck telescopes and the JWST are the only telescopes that are regularly phased. Whereas other 10m class telescopes such as the HET, SALT, and GTC, all work under the seeing limited domain, where a phasing accuracy of a few microns is found to be sufficient. Only after one and a half decades of operation, the GTC team is now upgrading the system for more precise alignment and phasing of segments (Castro et al., 2024). Therefore, considering the complexities involved in the segmented mirror technology, it is imperative to first explore the criticalities associated with the SMT and then implement it on the Indian large segmented mirror telescope, so that risk of failure can be eliminated/minimized. Taking this into account, the current thesis primarily deals with the phasing related challenges. The emphasis is to first understand different phasing techniques through simulations and laboratory experiments and then, choose the most suitable technique which can be implemented in the proposed large telescope.

1.5 The Alignment and Phasing System

To make the segmented primary mirror work like a single monolithic mirror, it is important to align all its segments precisely. The alignment (which primarily means co-alignment, co-focusing, and co-phasing of mirror segments) is performed by a specialised optical device called the Alignment and Phasing System (APS). The APS sets up a reference for the segment tip-tilt and piston positions. Figure 1.3 shows an array of seven segments in which the center segment has tip-tilt and piston errors. Once the alignment procedure is completed by the APS, then subsequently, the primary mirror control system (M1CS) maintains the segment alignment with the help of actuators and edge sensors. The M1CS maintains the segment alignment over variable gravity, wind forces, and changes in the environmental conditions. The alignment and phasing process in any segmented mirror telescope primarily involves three major tasks: i) co-alignment, ii) co-focusing, and iii) co-phasing.

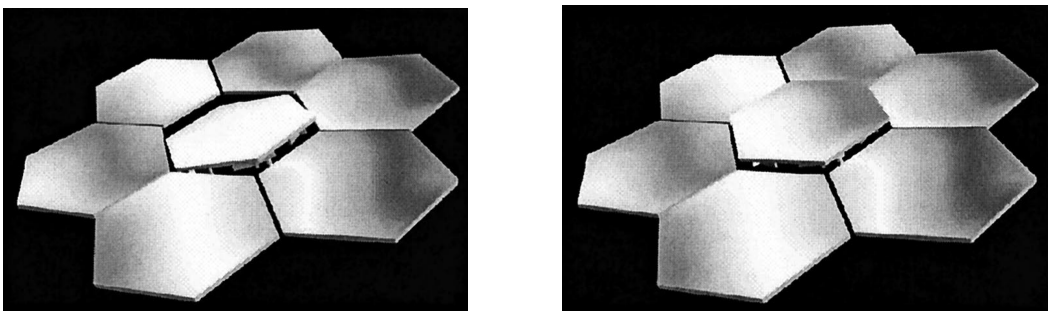

Figure 1.3: Depiction of segmented primary with center segment subjected to tip-tilt (left) and piston error (right). *Credit:* Pizarro et al. (2002).

1.5.1 Co-alignment and Co-focusing

The co-alignment of the segments deals with the removal of segment tip-tilt errors Figure 1.4. In the presence of tip-tilt errors, the image formed by each segment falls at different position on the detector/ focal plane. Figure 1.5 shows the simulated telescope PSF in the presence of tip-tilt errors for a 19 segment primary. By correcting the tip-tilt errors, these images are stacked together onto a single point so that all the segments form a single image of the object. The tip-tilt correction is applied with the help of three actuators capable of moving the segment with a few nanometer accuracy.

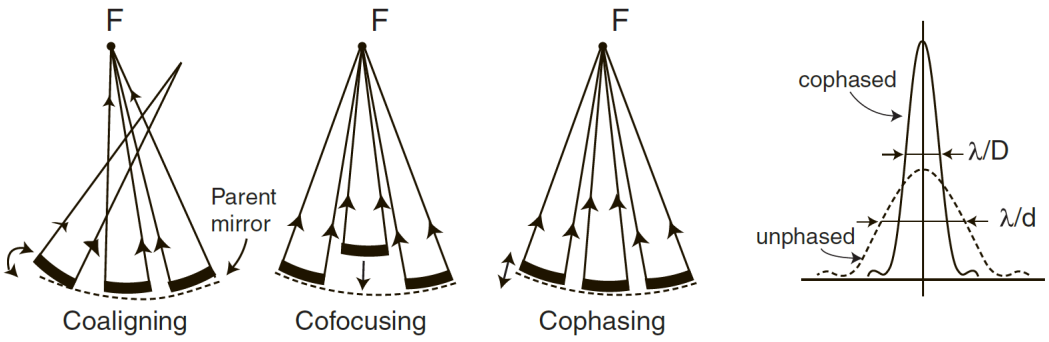

Figure 1.4: Illustration of segment alignment, focusing and phasing errors (left). Effect of segment phasing on imaging performance of the segmented mirror telescope (right). *Credit:* Bely (2003).

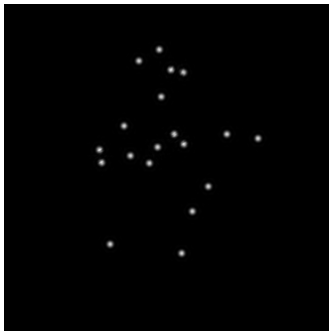

Figure 1.5: Simulated telescope PSF in presence of RMS tip-tilt errors of 1.5arc-secs.

The second error that is corrected by the APS is the Radius of Curvature (ROC) error or the defocus error, and the process is called co-focusing. In case of a mismatch between the segment ROCs, the PSF formed by different segments on the detector plane are unequal in size. This is because the ROC error of an individual segment is manifested as a longitudinal defocus on the detector plane. Thus, co-focusing deals with the ROC adjustment of the segments so that each of their PSFs becomes equal in size. The ROC correction is applied with the help of a warping harness, which is also used to correct the segment figure errors. The error in the segment ROC is directly linked to the longitudinal defocus error by a factor of 1/2. Hence, the terms

ROC and defocus errors are used interchangeably throughout the text.

In general, the task of co-alignment and co-focusing is performed by measuring the segment tip-tilt and defocus errors using a conventional Shack-Hartman (SH) based wavefront sensor. After the co-alignment and co-focusing procedures are completed, the spatial resolution achieved by the telescope would be equivalent to that of a single segment (λ/d, where d is the diameter of a single segment).

1.5.2 Co-phasing

The third task, co-phasing of the segments, involves the removal of very small piston errors (or the height difference) between any two adjacent segments. In the presence of piston errors, the wavefront reflected from different segments gets subjected to OPD/phase errors. Thus, at the focal plane, the reflected wavefront from each segment is superimposed incoherently, and this limits the telescope resolution to $1.22\lambda/d$, where d is the diameter of a single segment (Figure 1.4). In order to achieve the diffraction-limited resolution of the telescope with the whole primary ($1.22\lambda/D$, D is the diameter of the complete primary), the segments must be phased by reducing the piston errors in the order of a few nanometers. Figure 1.6 shows the simulated telescope PSF (in log scale) and intensity plots before and after the phasing process is performed.

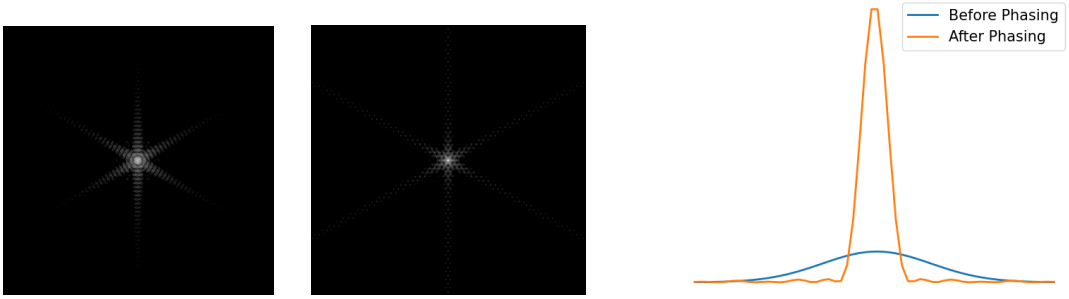

Figure 1.6: Effect of phasing on telescope PSF: Simulated PSFs, in logarithmic scale, before (left) and after (middle) phasing. Intensity plots for PSFs before and after phasing (right). Note: Plots are not to scale.

1.5.3 Co-alignment and Co-focusing Techniques

The APS is a dedicated optical instrument that performs the tasks of co-alignment, co-focusing, and co-phasing. Depending on the alignment requirements of the telescope, the basic principle of error measurements may vary. The co-alignment and co-focusing tasks are usually performed by a SH wavefront sensor. Several other wavefront sensing techniques, such as the Pyramid sensor, interferometry, and phase retrieval, can also provide the segment tip-tilt and focusing errors. However, these techniques have a limited measurement range of $\pm\lambda/4$. Hence, they cannot be used when the alignment

errors are large. Therefore, the most preferable technique for tip-tilt and ROC error measurements is the SH sensor based wavefront sensing because the construction of the device is fairly simple, and its measurement range as well as accuracy can be easily controlled by playing with very few design parameters. Additionally, by increasing the number of spots per segment, the SH can also be used to get the higher-order aberrations that are required to correct the segment figure errors. The SH sensor is an array of micro-lenses which sample the light from small wavefront regions and re-images it on the detector plane. Under ideal conditions, when there are no alignment errors, a uniform array of spots is obtained on the detector plane; these are the reference spots. In the presence of wavefront errors, the incoming wavefront is distorted, and hence, the spot distribution on the detector plane is disturbed. By comparing the position of these spots with respect to the reference spots, the wavefront slopes can be determined, and hence, the corresponding tip-tilt and defocus (or ROC) error of the segment can be derived.

When the alignment device is placed at the telescope focal plane, the telescope pupil is de-magnified and re-imaged to get the collimated beam from the star light. A sampling aperture mask is placed in this beam, which samples the light from the center of the segments. Depending on the alignment requirement, the mask can be designed to sample light from multiple sub-aperture regions on a single segment. For example, the Keck Phasing Camera System (PCS) (Chanan et al., 1994) has four different modes of operation, each one of which uses different number of spots per segment depending on the phasing mode. The passive tilt mode uses one sub-aperture per segment to stack the PSFs from individual segments together. The fine screen mode uses 13 spots per segment which is used for the secondary mirror alignment. The ultra-fine mode uses 217 spots per segment, which measures the surface figure of each segment. The fourth mode is the phasing mode, which is used for the measurement of segment piston errors and is described in subsection 1.6.2.

Another type of SH-based alignment device is the one where the device is placed at the ROC plane of the primary mirror, and an internal illuminating source is used in this case. The light from the telescope ROC plane is re-imaged, and the SH is used for tip-tilt and co-focusing measurements. The SALT (Wirth et al., 2004) and HET (Wolf et al., 2003) telescopes have used this kind of alignment device, where a separate tower is constructed to place the device at the ROC plane of the primary mirror.

1.5.4 Co-phasing Techniques

Since SH is insensitive to piston errors, it can not be directly used to phase the mirror segments. Utilizing the principle of physical optics, the Keck group led by Garry Chanan came up with two innovative phasing schemes, named narrow-band (Chanan, Ohara, and Troy, 2000) and the broad-band (Chanan et al., 1998) phasing

techniques. The broad-band phasing technique has a large measurement range but lower accuracy. In contrast, narrow-band can work over a small range ($< \lambda/4$) but provides an extremely accurate measurement of the segment piston errors. Though, after Keck, many segmented mirror telescopes have been built and are operating. However, it is only the twin Keck telescopes, whose mirror segments are regularly phased, and hence, it delivers close to diffraction-limited imaging in infrared using an adaptive optics system. Despite its successful implementation, the Keck phasing scheme suffers from a few limitations, such as the need for two different techniques, complexities of the device, the requirement for a higher SNR, long execution time to phase the mirror segments, etc. Therefore, considering the upcoming large segmented mirror telescope projects, where the number of segments to be phased is expected to be much larger than the 36 segments of the Keck telescopes, many groups have been trying to devise alternate ways of phasing mirror segments. The pyramid sensor (Esposito and Devaney, 2002), phase retrieval (Ragland and Gers, 2022), Dispersed Fringe Sensor (Shi et al., 2004a), and OTF (Baron et al., 2008; Guerri et al., 2010) based phasing techniques are a few examples. A brief overview of a few important co-phasing schemes is given in the subsequent section.

1.6 Review of Phasing Techniques

1.6.1 Classification of Phasing Techniques

The segment phasing schemes are basically wavefront sensing techniques, that rely on physical optics. Considering the specific requirements of existing and/or upcoming segmented mirror telescope projects, a verity of segment phasing techniques are being developed by different groups. The phasing techniques are generally classified as focal plane or pupil plane techniques. This classification is based on the position at which the phase measurement is made. For the focal plane techniques, the image at the focal plane is directly used for the phase measurements, this includes techniques such as phase retrieval (Gonsalves, 1976) and the curvature sensor (Orlov et al., 2000). Whereas the pupil plane techniques use the re-imaged telescope pupil to derive the wavefront phase information. This includes the techniques such as, the Keck broad and narrow-band phasing schemes (Chanan, Ohara, and Troy, 2000; Chanan et al., 1998), the Zernike phase contrast sensor (Surdej, Yaitskova, and Gonte, 2010) and the pyramid sensor (Esposito et al., 2005).

Irrespective of this classification, we found that one of the major problems with all these phasing techniques is that they have a strong trade-off between their measurement range and accuracy. Most of the phasing techniques that use a monochromatic light source, have the inherent problem of phase wrapping, that arises because the optical wavefront phase follows a sinusoidal function. Since the sine function has a 2π

periodicity, the same is translated to the wavefront phase. The wavefront phase (ϕ) is further related to the optical path difference $\Delta\lambda$ by the relation,

$$\phi = \frac{2\pi\Delta\lambda}{\lambda} \tag{1.1}$$

Thus, the 2π periodicity in phase is translated as a periodicity of λ in terms of the Optical Path Difference (OPD). When a piston error of δ is present between two segments, it leads to an OPD of 2δ on the wavefront due to reflection on the mirror surface (Figure 1.7). In this thesis, whenever we refer to the piston error δ, it indicates the physical height difference between the two segments, and hence the OPD/ wavefront error will be 2δ.

$$\Delta\lambda = 2\delta \tag{1.2}$$

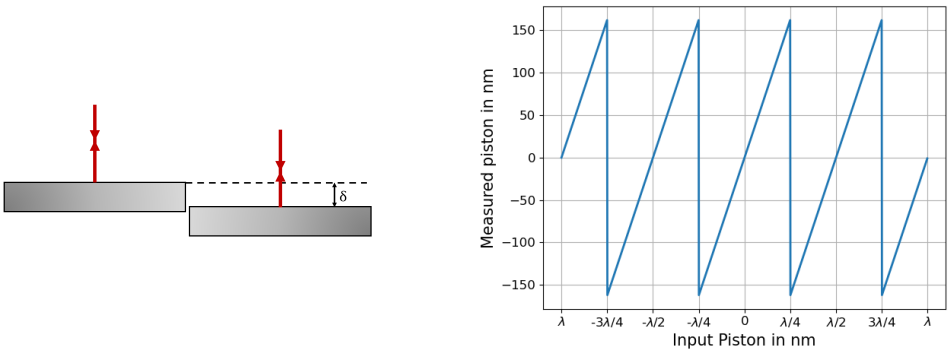

Figure 1.7: Relation between piston error and OPD or wavefront phase between two segments (left). Variation of input and measured piston values due to phase wrapping (right).

Due to this relation, the periodicity of λ in OPD gets transmitted as a periodicity of $\lambda/2$ in terms of piston. Figure 1.7 shows the variation of the measured vs. the input piston values where the effect of $\lambda/2$ phase wrapping can be clearly observed. Due to this, the measurement range of many phasing techniques (that require a monochromatic source) gets restricted to $\pm\lambda/4$. But the advantage of these techniques is that they can provide an extremely high measurement accuracy (in the range of just a few nanometers). The natural solution to extend the measurement range of the phasing techniques is to use a broad-band light source so that the $\pm\lambda/4$ ambiguity can be resolved. For broad-band light, the measurement range is decided by the coherence length (l) of the filter being used, which is defined as,

$$l = \frac{\lambda^2}{2\Delta\lambda} \tag{1.3}$$

where, λ is the central wavelength and $\Delta\lambda$ is the band width of the filter used. Such phasing techniques can have a large measurement range of up to a few tens of microns, but their phasing accuracy falls in the range of a few hundreds of nanometers. Hence,

the techniques that use a broad-band light source provide a large capture range ($\approx 100 - 200\mu$m), but their accuracy is of the order of $\lambda/10$. Thus, these techniques do not meet the phasing requirement of <10nm. Whereas the monochromatic phasing techniques have the desired accuracy, however, they suffer from phase wrapping, due to which their measurement range gets limited to $\pm\lambda/4$. Therefore, based on the measurement range and accuracy of the phasing techniques, we can classify them as coarse and fine phasing techniques.

- Coarse phasing techniques: High measurement range (of the order of tens of microns), low accuracy (of the order of a few hundreds of nano-meters)
- Fine phasing techniques: High accuracy (of a few nano-meters), measurement range $< \pm\lambda/4$

Due to this strong trade-off between the measurement range and accuracy of the phasing techniques, most of the existing telescopes are bound to use two different phasing techniques to achieve their phasing requirements. For example, the Keck telescopes use the broad-band phasing for coarse and narrow-band phasing for fine piston measurements (subsection 1.6.2). Similarly, the JWST uses the DFS for coarse phasing and the phase retrieval for fine phasing (Acton et al., 2022). In the following sub-sections, we discuss a few phasing techniques that have been either experimented in the laboratory only and/or implemented/tested on real telescopes. So far, the twin Keck telescopes and the JWST are the only telescopes that have been phased successfully to achieve the diffraction-limited imaging performance.

1.6.2 The Keck Phasing Technique

The twin Keck telescopes are the only ground-based telescopes that have been regularly phased successfully with an RMS error of about 30-50nm. The phasing of the Keck telescope is performed by the Phasing Camera System (PCS) (Chanan et al., 1994) instrument, which uses the modified SH approach for the phasing, in which sub-aperture masks are used to sample the light from the inter-segment regions. The Keck phasing technique involves two types of phasing schemes: the narrow-band and broad-band phasing.

1.6.2.1 Narrow-band Phasing

The Keck narrow-band phasing uses natural star light with extremely narrow band-pass filters . The telescope pupil plane is re-imaged, and a sub-aperture mask is placed in the pupil plane to sample the light from 78 inter-segment regions. The sub-aperture mask at each inter-segment edge is followed by a prism array that gives distinct SH images on the detector plane. The diffraction pattern for each inter-segment edge is recorded. The secondary peak intensity of the diffraction pattern varies cyclically

with the applied piston error. For any given piston value, the diffraction pattern is recorded, and then it is correlated with eleven artificially generated templates for phase errors between 0 to $\lambda/2$ (Figure 1.8). The template which gives the highest correlation coefficient provides the piston value for that particular pair of mirror segments.

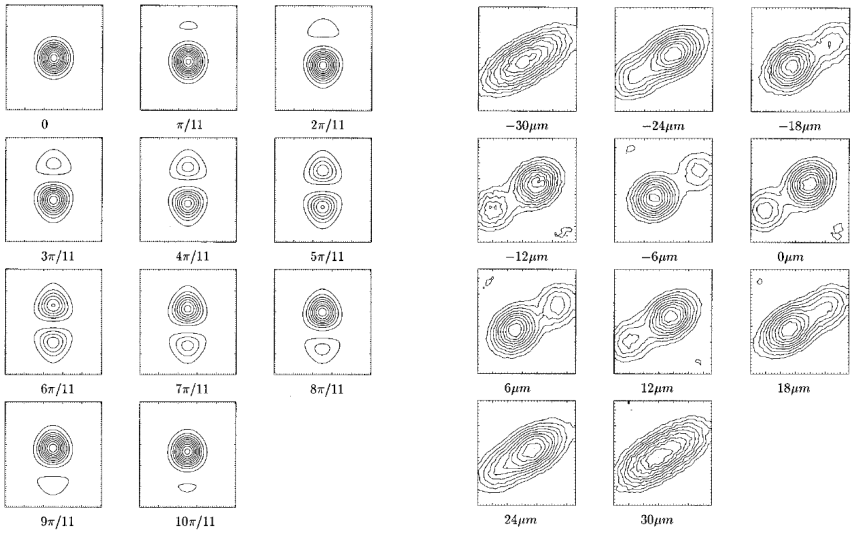

Figure 1.8: Theoretical diffraction patterns for Keck narrow-band (left) and broad-band (right) phasing technique for varying piston errors. *Credit:* Chanan et al. (1998).

Since the piston error appears as a phase error in the wavefront, it follows a sinusoidal cyclicity of $\pm\lambda/4$. Therefore, the measurement range of narrow-band phasing gets limited to $\pm\lambda/4$ only. The piston error measurement as accurate as 6nm RMS has been reported using the PCS instrument mounted on the telescope (Chanan, Ohara, and Troy, 2000). However, since the measurement range of the piston error is limited to $\pm\lambda/4$, the Keck group, led by Gary Channan, devised an alternate phasing scheme that provides a larger capture range.

1.6.2.2 Broad-band Phasing

The broad-band phasing technique is very similar to the narrow-band phasing except that the narrow-band phasing considers light to be strictly monochromatic while, in the broad-band, the finite spread of the filter response function is taken into consideration. For a filter with a band width of $\Delta\lambda$, the coherence length l is given by $\lambda^2/2\Delta\lambda$. Hence, the measurement range now becomes $\pm l$. To measure the piston error, eleven known edge steps are applied on the segment from the initial piston value and for each step, the broad-band diffraction patterns are recorded. Figure 1.8 shows the theoretically generated diffraction patterns for broad-band phasing. The recorded images are correlated with the narrow-band templates, and then the coherence parameter (which is the difference between the maximum and the minimum correlation coefficients) is calculated. The coherence parameter follows a Gaussian distribution

with the applied edge step height. The peak of this Gaussian curve gives the segment piston value. The broad-band phasing technique is found to have a comparatively lower measurement accuracy (of 30nm) as compared to narrow-band (which has an accuracy of 6nm) (Chanan et al., 1998). Hence, initially, it was planned to use the broad-band phasing scheme to bring down the piston error within the $\pm\lambda/4$ range. Then, the narrow-band phasing can be further used for the fine phasing of segments.

The narrow-band phasing has several advantages over broad-band phasing. It is faster and more accurate (statistical uncertainties of better than 10nm vs. 30nm for the most accurate broad-band mode), and it is passive; that is, it does not require perturbation of the primary mirror segments using the actuators. However, it lacks robustness due to which, practically, only the broad-band algorithm is used on the telescope. A thorough investigation into the lack of robustness of the narrow-band algorithm has now shown that it results from systematic errors ($\approx$ 20nm on average) that are wavelength-dependent (Chanan and Troy, 2018). The cause of these errors is mainly attributed to the presence of Ion Beam figuring (IBF) plateaus. The rotational misalignment of the phasing mask with respect to the pupil is another reason and there appears to be at least one additional cause that is currently not understood (Chanan and Troy, 2018). Thus, despite having better accuracy, the narrow-band phasing is not used on the Keck telescopes.

Although the broad-band phasing technique provides the desired phasing accuracy, but it has certain limitations: (i) it requires bright stars of 4^{th} to 7^{th} magnitude, (ii) it requires movement of segments in 11 steps to obtain piston value (iii) The complete phasing procedure takes a few hours of the precious telescope time. These limitations make the phasing procedure a bit complex and time consuming, thus creating a scope of improving/ developing new phasing techniques.

1.6.3 Pyramid Sensor Based Phasing

The pyramid sensor is generally used in adaptive optics systems for high precision wavefront sensing. It can measure the segment piston, tip-tilt, and wavefront aberrations simultaneously from a single set of observation. The basic principle of a pyramid sensor is that when any beam falls at the tip of the pyramid, it splits into four parts, which can be imaged on four different pupils (Figure 1.9). When an ideal spherical wavefront is incident on the pyramid, it falls exactly on the tip of the pyramid and hence gives four identical pupil images. If the incoming wavefront has any aberrations (including piston error), the intensity distribution of the four pupil images changes accordingly. The piston value can be extracted by analysing these four intensity distributions along the x and y co-ordinates on the pupil plane. The capture range of the pyramid sensor is primarily $< \pm\lambda/4$, which can be extended to some extent by using multiple wavelength observations. The advantage of this technique is that it does not require any specialised mask as light from the complete pupil is sampled at

once and all segments are measured simultaneously. However, manufacturing a pyramid sensor with a very precise tip and four faces is challenging and costly. Another major limitation of this technique is the linearity of the sensor; in order to increase the linearity range, modulation techniques are used, which basically involves rotation of the pyramid in circular motion. Although modulation helps to improve the linearity of the sensor, however, it makes the system complex and time consuming.

Although the pyramid sensor is widely used in adaptive optics applications, but it is hardly used for phasing of any segmented mirror telescope. In laboratory experiments, a piston measurement accuracy of 10-15nm has been achieved with the pyramid sensor (Esposito et al., 2005). The pyramid sensor based phasing experiment was also performed in our laboratory at IIA by Annu Jacob as part of her PhD thesis work, where a measurement accuracy of 20nm was achieved (Jacob et al., 2018). Figure 1.9 shows an example of the pupil image obtained in the laboratory experiment.

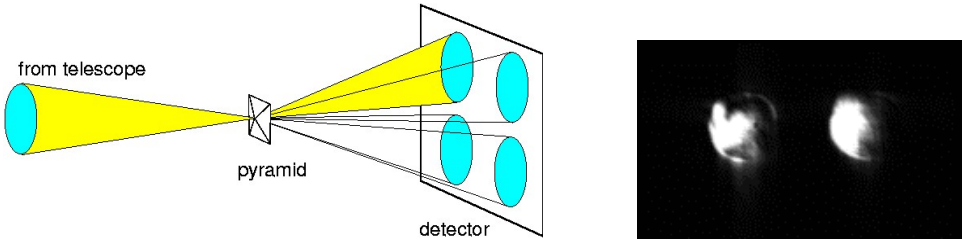

Figure 1.9: Schematic of splitting of a beam into four equal parts by the pyramid sensor (left). *Credit:* Tokovinin (2001). An example of pupil images obtained from the pyramid sensor experiment in our laboratory at IIA (right). *Credit:* Annu Jacob.

1.6.4 Phase Retrieval Technique

The phase retrieval technique is an image-based wavefront sensing technique, which uses a point source image to derive the wavefront phase (Gonsalves, 1976). Using the recorded PSF, an initial estimate of the wavefront phase is applied, and then an iterative process is followed until the measured and derived PSFs match closely. To remove the sign ambiguity of phase, a second PSF is recorded by defocusing the image plane. This technique strongly relies upon the iterative phase estimation algorithm. Since a monochromatic light source is used, the phase wrapping problem is also seen in this case, and hence, the measurement range is limited to $\pm\lambda/4$. However, the capture range can be extended slightly by using images obtained using multiple wavelengths. Due to the limited range and high accuracy, the phase retrieval technique is used for fine phasing of segments. The same technique is also used for the fine phasing of the JWST mirror segments (Dean et al., 2006; Acton et al., 2022). By using the DFS-based coarse phasing technique, the initial piston error of JWST mirror segments are first brought down to less than $1\mu m$, then the fine phasing procedure is initiated by applying the phase retrieval technique. In this scheme, by using the same science

imaging device, a set of PSFs are recorded for defocus values of $\pm 8\lambda$ and then phase retrieval algorithm is applied to obtain the wavefront phase. Figure 1.10 shows the simulated defocused PSFs for $\pm 8\lambda$ and their corresponding phase maps obtained after applying phase retrieval for JWST (Acton et al., 2012). Since the phase retrieval gives the complete pupil phase map, it can measure all segments simultaneously. Additionally, it can also be used to measure the higher order wavefront errors and hence correct for the overall complete primary mirror RMS error. For the JWST, an RMS wavefront error of about 44nm was achieved for the complete primary after the fine phasing procedure was completed using phase retrieval (Acton et al., 2022).

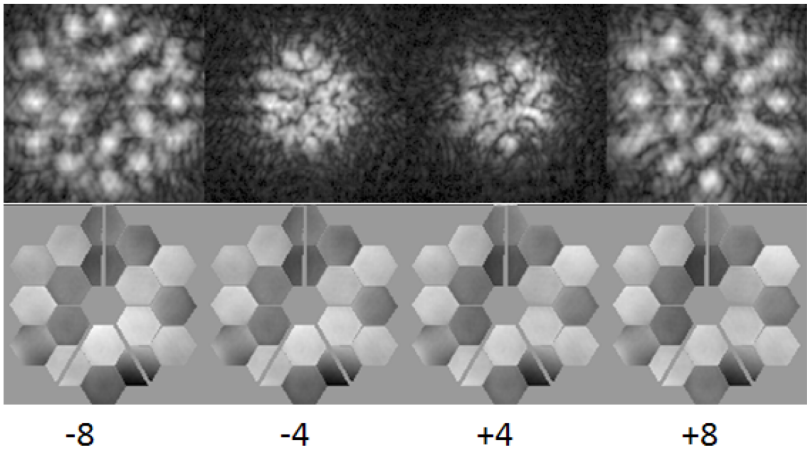

Figure 1.10: Sequence of simulated defocused images for the JWST science instrument (top). Depiction of piston errors of 18 JWST mirror segments derived using the phase retrieval method (bottom). *Credit:* Acton et al. (2012).

1.6.5 Zernike Phase Contrast Sensor

The Zernike phase contrast sensor uses a Zernike phase mask, which is placed at the focal plane of the telescope. The phase mask is a cylindrical pellet etched into a substrate. The diameter of the pellet is of the order of the seeing disk, and the depth of the pellet is a small fraction of the wavelength (Figure 1.11). Thus, a phase shift is introduced between the center of the PSF and its outer rings. This helps to filter out the low frequency components of the wavefront, and only the high frequency components, such as piston errors (corresponding to the wavefront discontinuities) are transmitted. The wavefront phase information is obtained as intensity variations on the detector plane (Figure 1.12). The capture range of this technique is again limited to $\pm\lambda/4$, thus making it a fine phasing technique. A phasing accuracy as good as nearly 7nm has been achieved with this technique (Surdej, Yaitskova, and Gonte, 2010).

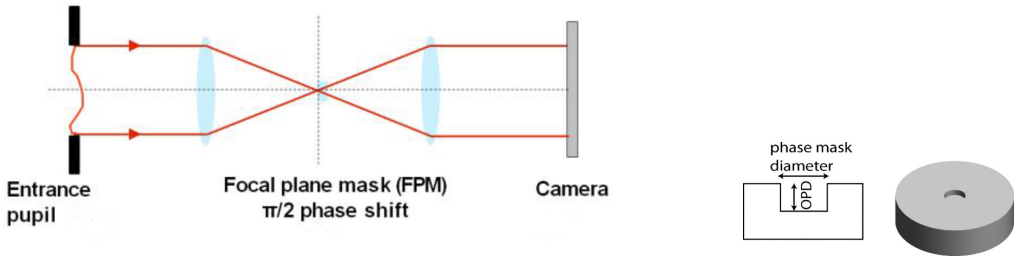

Figure 1.11: Schematic showing Zernike Phase contrast sensor (left) *Credit:* El Hadi et al. (2016). The phase mask used at focal plane (right) *Credit:* Surdej, Yaitskova, and Gonte (2010).

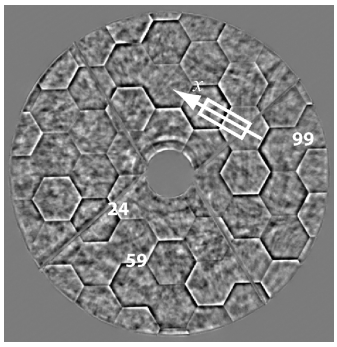

Figure 1.12: Example of an pupil image obtained from the on-sky testing of Zernike phase contrast sensor. *Credit:* Surdej, Yaitskova, and Gonte (2010).

1.6.6 Interferometric Phasing

The interferometric phasing technique (Pizarro et al., 2002) uses the basic principle of interferometry to measure the segment piston error. The interferometer design may be based on the Mach Zehender interferometer, the Michelson interferometer, or the Twyman Green Interferometer. All these interferometers work on the same concept, i.e., it has two beams, namely, the measurement beam and the reference beam (Figure 1.13). The measurement beam falls on the inter-segment gap, and the reference beam is made to fall on one of the segment surfaces close to the inter-segment gap. Due to the piston error, the part of the measurement beam falling on the other segment has an extra path difference with respect to the part that falls on the same mirror as the reference beam. This causes a lateral shift in the fringe position, which is used to extract the piston value (Figure 1.13). The shift can be easily noticed in the case of white light; another advantage of using white light is that, it removes the $\lambda/4$ ambiguity. The same fringes can also be used for tip-tilt measurement of the mirrors because a tilt in the system causes the fringe period to change, and a tip causes the fringes to deviate from vertical. Experiments have shown that a measurement range of 12μm and accuracy of up to 5nm can be achieved with this technique (Pizarro et al., 2002). Another form of interferometric measurements is based on the principle of shearing interferometry as discussed in Voitsekhovich, Bara, and Orlov (2002). The

SEMEI telescope also uses a slightly modified version of the interferometric phasing for piston measurements (Kurita et al., 2020).

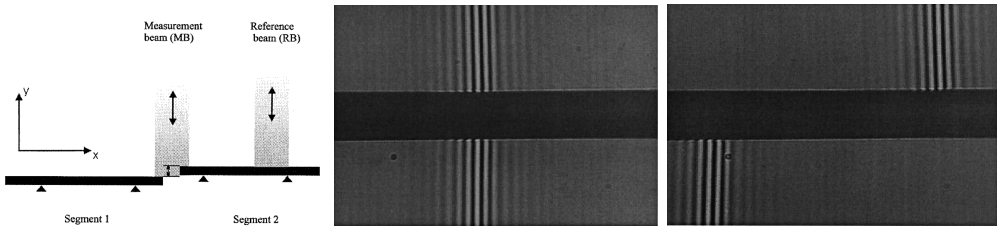

Figure 1.13: Interferometric phasing of segments: Reference and measurement beam falling on inter-segment gap (left), White light interferometric fringes for zero piston (middle) and 8μm piston error (right). *Credit:* Pizarro et al. (2002).

1.6.7 Dispersed Fringe Sensor

The Dispersed Fringe Sensor uses a broad-band light source and generates a source spectrum by using a dispersive element. The basic idea of this technique is that in the presence of piston errors, the source spectrum is modulated by sinusoidal fringes. The period of these fringes can be related to the piston error. A deeper exploration of the DFS phasing scheme is a part of this thesis work and its detail can be found in chapter 4.

1.6.8 Optical Transfer Function based Phasing

The Optical Transfer Function (OTF) is defined as the Fourier transform of the PSF. Since the OTF is a complex quantity, it has two components: the magnitude and phase. Both of these components contain information about the phase of the wavefront. We have conducted an extensive study on the OTF for alignment and phasing of mirror segments. The details about this scheme can be found in chapter 5.

1.6.9 Phasing Schemes at a Glance

Based on the literature survey carried out for the various phasing techniques, they can be compared for their advantages as well as disadvantages. Table 1.1 summarises the comparative analysis for some of the phasing techniques. A few of the important criteria considered here are the measurement accuracy, range, feasibility for simultaneous measurement of all segments, and capability of tip-tilt measurements. Based on their measurement range and accuracy, the conventional classification of these techniques as coarse or fine phasing is also mentioned.

Table 1.1: Comparative analysis of various phasing techniques. Shades of green colour indicate the advantages of the technique and orange colour indicate the limitations.

Phasing Technique	Accuracy	Capture Range	Feasibility for Multi segment Sampling	Capability of Tip-tilt Measurement	Classification
Keck Narrow Band	6nm	$\pm\lambda/4$	Requires prism array	No	Fine Phasing
Keck Broad Band	30nm	30µm	Requires prism array	No	Coarse Phasing
Pyramid Sensor	10-15nm	$\pm\lambda/4$	All segments measured simultaneously	Yes (range limited to $\pm\lambda/4$)	Fine Phasing
Phase Retrieval Technique	30-50nm RMS Wavefront error	$\pm\lambda/4$	All segments measured simultaneously	Yes (range limited to $\pm\lambda/4$)	Fine Phasing
Zernike Phase Contrast Sensor	7nm	$\pm\lambda/4$	All segments measured simultaneously	Yes (range limited to $\pm\lambda/4$)	Fine Phasing
Interferometric Phasing	5nm	12µm	Feasible	Yes (range limited to $\pm\lambda/4$)	Fine Phasing
DFS (Dispersed Fringe Sensor)	90nm	50µm	Requires prism array	No	Coarse Phasing (conventional)
OTF based Phasing	11nm	200µm	Feasible, by use of suitable mask	Yes (can measure larger tip-tilt errors)	Coarse Phasing (conventional)

1.7 Motivation of the Thesis

India is venturing to build a large optical-NIR telescope made of segmented primary mirror, ingeniously. Since segmented mirror technology is not yet standardised, so there is a need to carry out exploration/research on several key aspects of the technology. One of the most critical requirements of any SMT-based telescope is to align and phase its mirror segments with unprecedented accuracy. Therefore, under this thesis, we decided to explore different alignment and phasing techniques and identify one that would be most suitable for the proposed large Indian telescope. From our preliminary study, we find that the DFS and the OTF-based phasing schemes have many advantages over other techniques and they also have the potential to be used for both coarse and fine phasing of mirror segments. Therefore, we decided to conduct an in-depth study on these two phasing schemes through simulations (Dharmadhikari, Parihar, and Jacob, 2023) and laboratory experimentation (Dharmadhikari and Parihar, 2024).

In any segmented mirror telescope, to meet the intended imaging performance, not only phasing but also a very precise co-aligning and co-focusing of mirror segments becomes equally important. Therefore, as a pilot project of the large upcoming telescope, we have also designed and developed a SH-based alignment device for the PSMT project (Dharmadhikari et al., 2024). Hence, through this thesis work we have tried to explore and gain knowledge about all three key aspects of the APS.

1.8 Outline of the Thesis

This thesis aims to explore, understand, and develop the alignment and phasing related techniques for the proposed 10m class Indian large telescope. This thesis is structured as follows: In Chapter 2, we start with defining the alignment requirements for the telescope and then use simulations to test the feasibility of the designed APS. In Chapter 3, we discuss the design and testing related details of the segment alignment device developed for the PSMT. Further, we move on to the phasing related aspects of the APS. Chapter 4 and Chapter 5 describe the simulations as well as experimental results obtained for the DFS and OTF-based phasing techniques, respectively. Finally, Chapter 6 summarizes the thesis by outlining the conclusions drawn from all the studies presented. This chapter also enlists the novel aspects of these studies and discusses the future prospects.

Chapter 2
Simulations on APS

Building a large affordable optical-NIR telescope (I): an alternate way to handle segmented primary mirror
Radhika Dharmadhikari, Padmakar Parihar, Annu Jacob, **Experimental Astronomy**, Volume 56, pages 569–604, (2023)

2.1 Introduction

The Alignment and Phasing System (APS) is the heart of any segmented mirror telescope. It is responsible for optically measuring the segment alignment errors, as discussed in section 1.5. Thus, once the mirror segments are co-aligned, co-focused, and co-phased optically, then the primary mirror control system (M1CS) continuously monitors and maintains these segment positions over time. For the telescope to achieve the desired image quality, it is important to align the mirror segments precisely as per the alignment requirements. The optical design of the APS must ensure that it meets the required measurement accuracy and range. We have developed an end-to-end simulation code in Python to study and predict the practically achievable performance of the APS for the India's upcoming segmented mirror telescope. The simulation also helps to define the alignment requirements for the proposed telescope. In this chapter, we discuss the alignment requirements and the results of extensive simulation work carried out to understand the performance of the APS for the Indian 10m class segmented mirror telescope.

2.2 The Telescope Design

For the simulations and analysis, we consider the initial 10m size design option, proposed for the Indian large segmented mirror telescope, which is a Ritchey-Chretein based optical design (section 1.2). The effective size of the primary mirror is 11.6m in diameter, made of 60 hexagonal segments of 1.4m size each. The primary as well as

the secondary mirror, both have a hyperbolic profile and a flat tertiary fold mirror is used to get the Nasmyth focus. The design gives diffraction-limited image quality up to a 5arc-min (diameter) field of view, beyond this the image performance degrades due to the off-axis aberrations like coma, astigmatism and field curvature. The optical design parameters are given in Table 2.1, and the ZEMAX generated optical layout is shown in Figure 2.1.

Table 2.1: Optical design details of the India's Large Segmented Mirror telescope

Parameter	Value
Primary Mirror	
ROC	35m
F/#	1.5
Diameter	11.6m
Conic Constant	-1.00308462
Secondary Mirror	
ROC	4.57m
Diameter	1.4m
Conic Constant	-1.66165862
Working F/#	12.5361
Effective focal length	145.409m
Plate scale	1.4185"/mm
Primary secondary distance	15.49m
Secondary tertiary distance	10.14m
Back focal length	6.561m
Focal plane ROC	2.053m

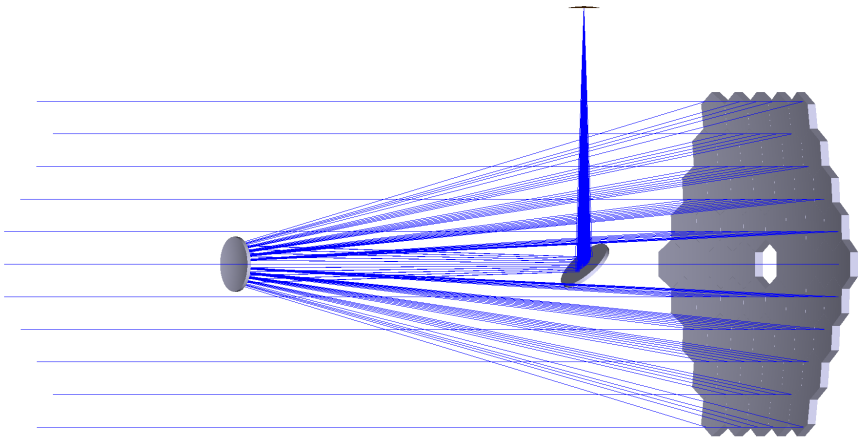

Figure 2.1: Optical design layout of the 10m size India's Large Segmented Mirror Telescope.

2.3 Alignment Requirements

Allocating the error budget for the segment alignment is very crucial as that would decide the final telescope image quality. For the 10m class segmented mirror telescope we have attempted to come up with the requirements by making use of simulations as well as by referring to the practically achieved values in the existing segmented mirror telescopes. We use a Python ZEMAX interfacing based tool to find alignment requirements for the India's large segmented mirror telescope (with optical parameters given in the Table 2.1). In order to give the alignment errors in ZEMAX, we use a specially developed segmentation tool (Jacob, Parihar, and James, 2020). This tool generates a grid sag surface with random tip-tilt, defocus and/or piston errors. The grid sag surface is then imported to ZEMAX where the image quality parameters such as the Strehl ratio, D50 and D80 are derived. All the image quality parameters obtained from the simulations are at a wavelength of 632.8nm.

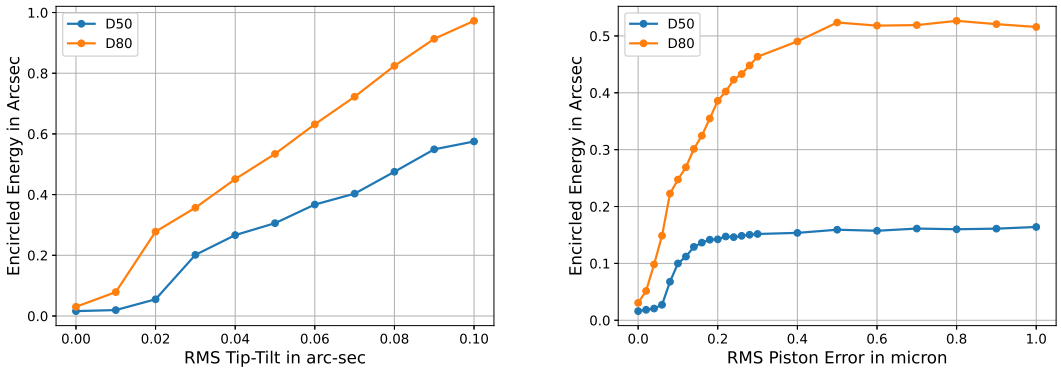

Figure 2.2: Variation of D50 and D80 values with RMS tip-tilt error (left) and RMS piston error (right).

Figure 2.2 shows the variation of the image D50 and D80 values in presence of tip-tilt alignment errors and piston errors. Thus from the plots, it is clear that under seeing-limited condition, a tip-tilt error up to 0.03arc-sec (it would degrade the seeing-limited FWHM by less than 1%) is allowable. Whereas, under diffraction limited condition we restrict the Strehl ratio to be >0.9 for which the RMS tip-tilt error must be <0.01arc-sec. In case of piston errors, the D80 is strongly affected as compared to D50. Both the D50 and D80 values degrade rapidly till piston error of about 0.3μm ($\lambda/2$) after that it becomes nearly constant up to a piston error of 25μm. Hence, for the seeing limited case, the piston error can be tolerated up to 25 to 30μm. Beyond this, the piston error falls under the domain of the focus error which can be measured using SH mode of APS and is corrected with the help of segment support actuators. Under seeing-limited condition, phasing of mirror segments is not required, but for diffraction-limited imaging, since we restrict the Strehl ratio to be >0.9 hence the

segments must be phased with an accuracy of 30nm or better. For co-focusing, we found that the ROC error of the individual segment must be <150μm, this has been discussed in detail in subsection 2.4.4.

The HET has an alignment requirement of 0.065arc-sec and requires a piston accuracy within 25μm (Wolf et al., 2003). Similarly for SALT the segment tilt error after fine alignment must be within 0.04arc-sec with a piston requirement of 20μm (Wirth et al., 2004). The point to be noted here is that, both HET and SALT telescopes are aimed to work in seeing limited domain and hence precise phasing of mirror segments is not needed. Whereas, for the Keck telescopes, which are designed to work in the diffraction limited mode, the tip-tilt error must be within 0.014arc-sec (Chanan, Nelson, and Mast, 1986). Keck segments are phased using the device called PCS which is capable of measuring piston errors down to 5-6nm in narrow-band mode (Chanan, Ohara, and Troy, 2000). From the simulations, as well as by studying few of the above mentioned cases, we have an estimate that the tip-tilt error requirement for our system would be approximately 0.03arc-sec for seeing-limited case and close to 0.01arc-sec for diffraction-limited case. The co-focusing requirement for the ROC errors are of the order of 150μm (discussed in details in subsection 2.4.4). The diffraction-limited imaging is only possible with the warping harness and it requires very small ROC errors (or defocus error), as well as other high orders segment figure errors. For co-phasing of the segments, under the seeing-limited case, the piston error can be of the order of 20-25μm and for diffraction-limited case it should be of the order of a few tens of a nano-meters. The typical requirement of alignment and phasing for a 10m class segmented mirror telescope for seeing-limited as well as diffraction-limited imaging is given in the Table 2.2.

Table 2.2: Alignment requirements for 10m class segmented mirror telescope

Alignment Error	Seeing-Limited Mode	Diffraction-Limited Mode
Co-aligning/ Tip-tilt error	$\leq$0.03arc-sec	$\leq$0.01arc-sec
Co-focusing/ ROC error	$\leq$150μm	$\leq$150μm
Co-phasing/ Piston error	$\leq$25-30μm	$\leq$30nm

2.4 Simulations on APS

Once the alignment requirements of the telescope are defined, the APS is designed as per the required measurement range and accuracy. However, under practical conditions, many external effects such as the stellar magnitude, atmospheric turbulence, external noises etc, play an important role in defining the performance of the APS. We have developed a Python-based simulation program that can be used to explore

the performance of any APS system, subjected to varieties of external effects. The simulation methodology and its applications are explained in detail in the subsequent sections.

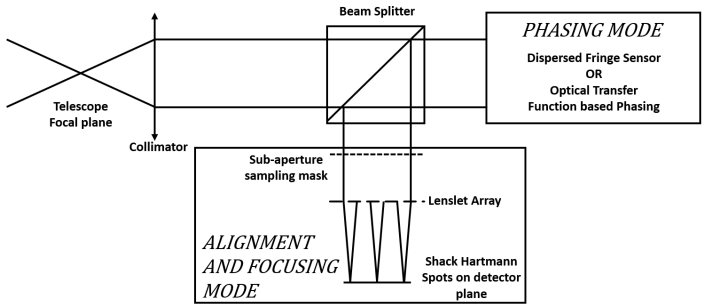

Figure 2.3: Schematic representation of two modes of the APS.

The schematic diagram for a generalised APS is shown in Figure 2.3. The APS would work in two different modes, namely, the alignment and co-focusing mode and the phasing mode. The light from the telescope focal plane enters into the APS, goes through a collimator, the collimated beam is then further split into two, using a beam splitter. One part of the beam enters the alignment and focusing section of the instrument, while the other part goes to the phasing instrument. For the alignment and focusing mode, a SH kind of setup with customized lenslet array is used. By assigning 1, 3 or 7 lenslets per segment, we can measure the tip-tilt error very precisely (Figure 2.11). Whereas, for defocus measurement, we need to have a minimum of 7 to 9 lenslets per segment to get precise measurements. For the phasing mode, we consider two phasing techniques, the Dispersed Fringe Sensor (DFS) and the Optical Transfer Function (OTF) based phasing. The phasing mode of the APS is described in detail in chapter 4 and chapter 5.

2.4.1 Simulation Methodology

While developing the simulation tool, we assumed a very generic form of the APS, which uses SH sensor for co-aligning and co-focusing. For co-phasing we have considered two techniques, the DFS and the OTF based technique for our exploration (discussed in chapter 4 and chapter 5). In all these cases, we primarily need to generate realistic images/spectra formed by segmented mirror telescope + APS system. Our end-to-end simulation code, written in Python, considers most of the significant external effects, such as, light loss due to atmospheric extinction and telescope + instrument optics, smearing of the image due to atmospheric seeing, and noises getting injected in the image/spectrum from all different sources. The parameters, such as the star magnitude, exposure time, the sampling aperture diameter, telescope focal length, telescope F-number, re-imaging optics focal lengths, sky brightness magni-

tude, object-moon separation, phase of the moon, the atmospheric Fried parameter (r_o), detector specifications (pixel size, quantum efficiency, dark current, detector temperature, read out noise) are given as input to the system. They are used to predict the realistic performance results for the APS. Figure 2.4 summarises the steps involved in the simulations.

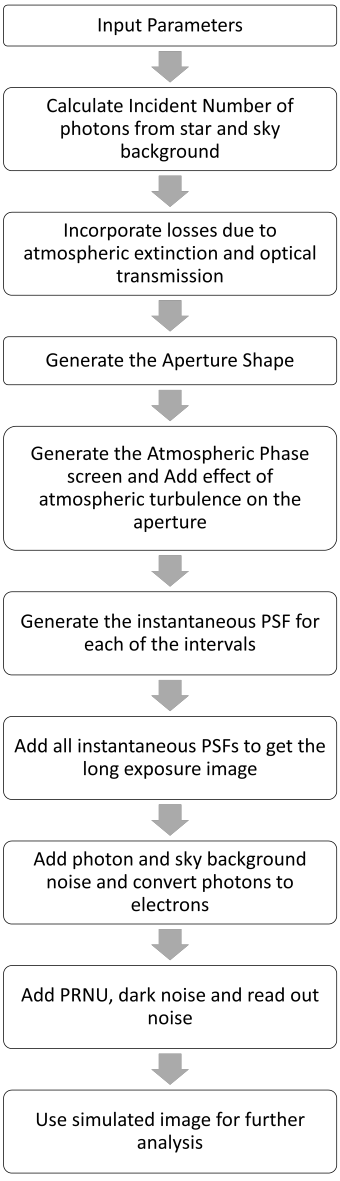

Figure 2.4: Flow chart explaining the simulation procedure for generation of simulated images for alignment and focusing mode.

Based on the external conditions, as well as requirements, the input parameters are given to the code. Using these parameters, we first calculate the incident number of photons from the star and then the aperture shape is created. Further, a random phase screen is generated using Python package AOtools (Townson et al., 2019), using

this phase screen, the average PSF is obtained, to which we add the photon noise, sky background noise and detector noises, the final image is obtained in ADU (Analog to Digital Units) counts. From this generated image the parameters such as SNR and centroiding accuracy are calculated. Since the atmospheric phase screen and all the noises generated have a random nature, hence to get a reliable value of SNR, we used Monte Carlo Simulations. The obtained PSF images are processed further in different ways to derive the tip/tilt, defocus and piston errors, the details of these are given in the corresponding sections.

2.4.2 Verification of Simulation Code

As one of the vital aspects of our code is generation of realistic images/spectra formed by telescope + instrument system. Therefore, before using the simulation tool for the APS system, we verified it on real astronomical observations from the 2m Himalayan Chandra Telescope, equipped with the Himalayan Faint Object Spectrograph and Camera (HFOSC) instrument of the Indian Astronomical Observatory. To verify the photometric simulations, we have used V-band observations of the M67 open stellar cluster, taken on three different nights with different atmospheric conditions. CCD images of 28 cluster members having different magnitudes and colours are generated using our Python simulation tool. The instrumental parameters used for the simulations are listed in the Table 2.3.

Table 2.3: Parameters for the HCT Observations

Parameter	Value
Wavelength Range	470-700nm (V-band)
Telescope Diameter	2.01m
Secondary mirror diameter	0.40m
Reflectivity of the mirror	90%
Number of Lens Elements	8
Transmittivity of lenses	95% at each element
Atmospheric Extinction (V-band)	$0.12 airmass^{-1}$
Sky Brightness	21.28 magnitude/$arc - sec^2$
Wind Speed	2.2m/s
Collimator and Camera Focal length	252mm and 147mm
Detector Pixel size	15μm
Detector Quantum Efficiency	85% @ 551nm
Detector Dark Noise	$0.3e^-$ per hour
Detector Read out Noise	$4.8e^-$
Detector Gain	$1.22e^-$/ADU
Image Scale	0.296arc-sec/pixel
Dispersive element	Grism 8 with 600 lines/mm

Other parameters such as the seeing, phase of the moon, object zenith angle, exposure time are obtained from the image files and given as input to the simulations. The synthetic stellar fluxes/magnitudes, match very well with the observed magnitudes and it nearly follows the relation y=x as shown in the Figure 2.5. The difference between synthetic and observed fluxes for all 28 stars of magnitude range 10-18, observed in three nights are within 15% (except 2-3 little deviant points). Figure 2.6 shows the comparison of the real and simulated images for a star of 16^{th} magnitude. Furthermore, we compared the radial profile of synthetic and observed stellar images (Figure 2.7) which remarkably matches in both x and y directions.

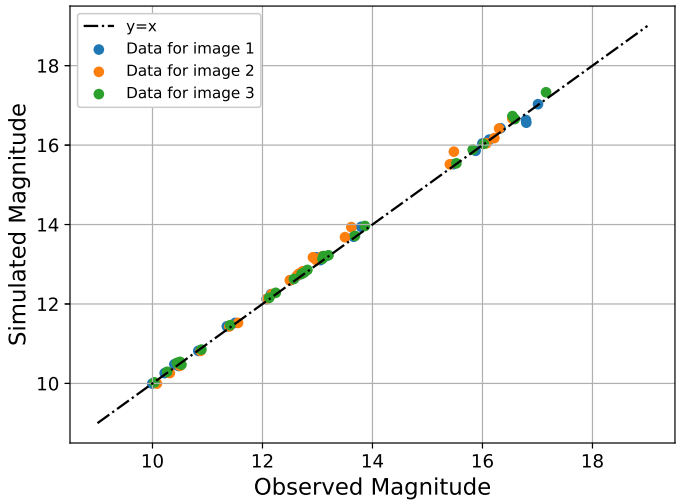

Figure 2.5: Plot showing the observed stellar magnitude vs simulated stellar magnitude.

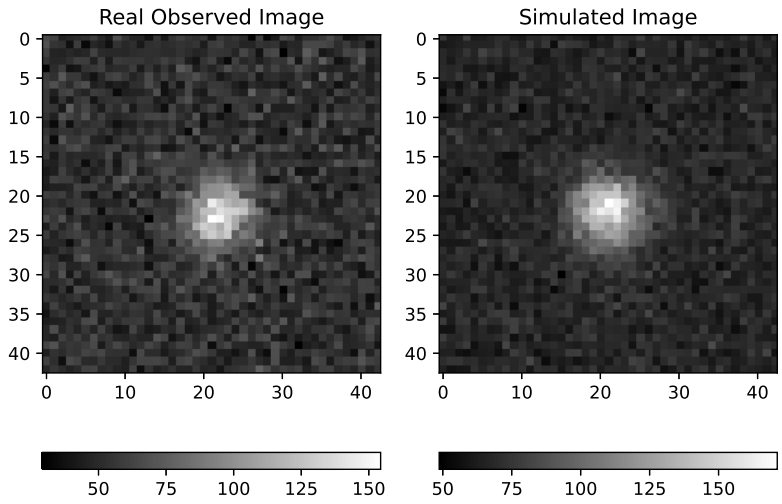

Figure 2.6: Real observed image (left) and simulated image (right) for stellar magnitude of 16.68 and exposure time of 5sec.

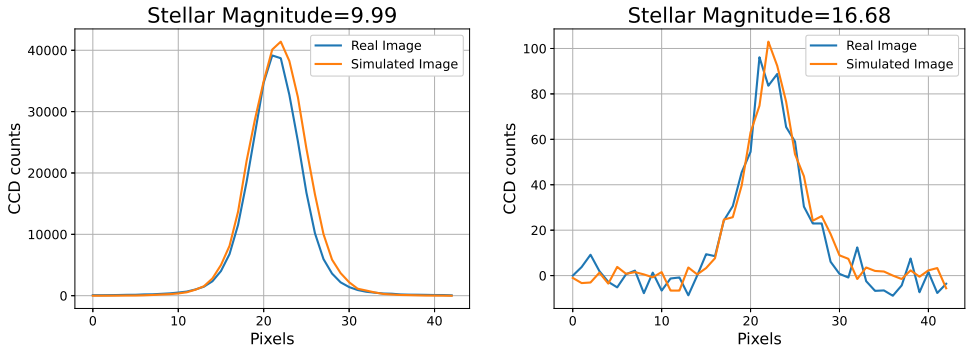

Figure 2.7: Intensity plots for simulated and real observed images for two different stellar magnitudes (stellar magnitude=9.99 (left) and stellar magnitude=16.68 (right)).

Similar to the photometric simulations, we also verified the spectroscopic simulations required for DFS based phasing instrument. For this purpose, spectra of a standard star Feige-34, observed using the HFOSC instrument at HCT was used. Few additional inputs required in the simulation tool were wavelength dependent parameters such as atmospheric extinction, lens transmissivity, grism response and detector response etc. Figure 2.8 shows the observed spectra and the corresponding simulated spectra. One can clearly find that the continuum of the observed Fiege-34 spectrum very well matches with the simulated spectrum. The departures seen at a few places are due to the presence of absorption features, which are not considered in the simulation. Hence, it can be concluded that the simulations give realistic results which match very well with the observations (both, photometric and spectroscopic) and thus we use this tool confidently to verify the expected performance of the APS.

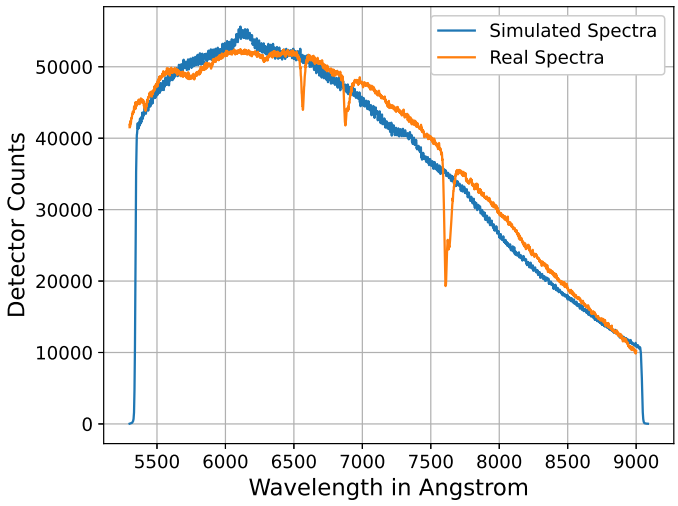

Figure 2.8: Plot showing the real observed spectra and the simulated spectra for spectroscopic standard star Feige 34.

2.4.3 Simulations on Co-alignment

The lenslet array of SH device samples light from different segments and generates an array of spots on the detector plane. Therefore, using our simulation tool, we generate realistic SH images subjected to different practical conditions. All the parameters used in the simulations are listed in Table 2.4.

Table 2.4: Parameters used in the Monte Carlo Simulations

Parameter	Value
Wavelength Range	470-700nm (V-band)
Sky Brightness	21.28 magnitude/$arc-sec^2$
Object-moon separation	45°
Moon Phase	Full Moon (ψ=0°)
Collimator Focal length	600mm
Lens Transmittivity	75% per lens
(assuming achromatic doublet lens)	
Wind Speed	9.5m/s
Detector:	
Pixel size	15μm
Quantum Efficiency	85%
Temperature	243K
Dark Noise	0.03e^- per pixel/second
Read out noise	2.3e^- per pixel
Detector gain	2
Camera focal length	37.659mm
Image scale on detector plane	0.339arc-sec per pixel

The camera focal length is chosen such that for 1arc-sec seeing the FWHM for the central wavelength covers 3 pixels approximately. This ensures the critical sampling of the image required to attain accurate centering. The location of the spots linked to segmented primary mirror are compared with corresponding reference spots and the deviation of the spot locations are used to measure the tip-tilt errors. The centroiding error will translate directly to the alignment error, hence we perform centroiding using the Photutils package which is an Astropy affiliated Python package for photometry (Bradley et al., 2021). The centroiding error is converted into the corresponding segment tip-tilt error using the detector plate scale. Figure 2.9 shows the steps involved in deriving the segment tip-tilt errors from the generated PSF images.

2.4.3.1 Effect of Size and Number of Sub-apertures

Using the simulation tool we have first explored the effect of the size of sub-aperture on Signal to Noise Ratio (SNR) of the spots. SNR is derived with and without considering

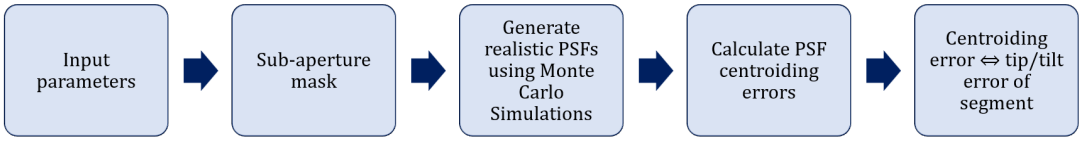

Figure 2.9: Flow chart for deriving the segment tip-tilt errors from simulated PSFs.

the atmospheric seeing effect. Figure 2.10 shows the variation of SNR with increasing aperture diameter for a 16^{th} magnitude star. As expected, SNR linearly increases with the sub-aperture diameter, which would improve the centroiding accuracy for the SH sensor. From Figure 2.10 it is clear that sensitivity and hence SNR reduces as seeing effect is introduced. For long exposure we obtain the seeing limited image and hence increasing the sampling aperture size does not change the FWHM of the PSF but only increases the SNR which proves to be very useful when working with the fainter stars. For each individual segment, we can have SH lenslet arrangement

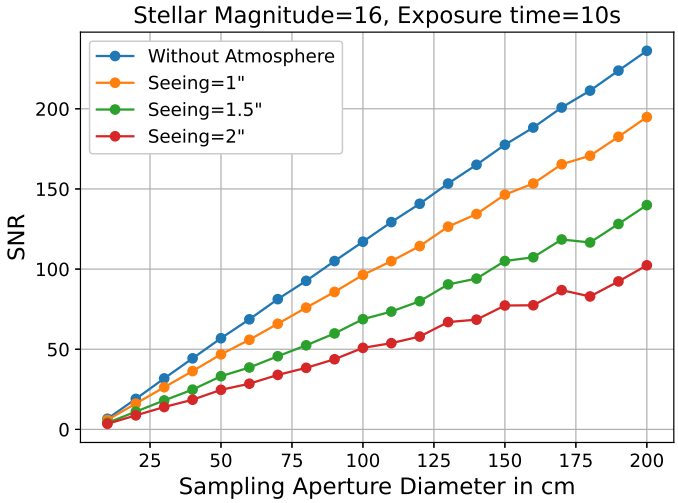

Figure 2.10: Variation of SNR with aperture diameter for 16^{th} magnitude star with 10sec exposure time.

in such way that light from the segment can be sampled using variable number of sub-apertures. In order to explore the effect of number of sub-apertures that one can fit into a segment, we carried out simulations with three different cases i) Seven spots with aperture diameter = 41.5cm each, ii) Three spots with aperture diameter = 62.3cm each and iii) Single spot with aperture diameter = 120cm, which covers the complete segment. Figure 2.11 shows the sub-aperture sampling position over a segment for each case and Figure 2.12 shows these simulated SH images for the three cases.

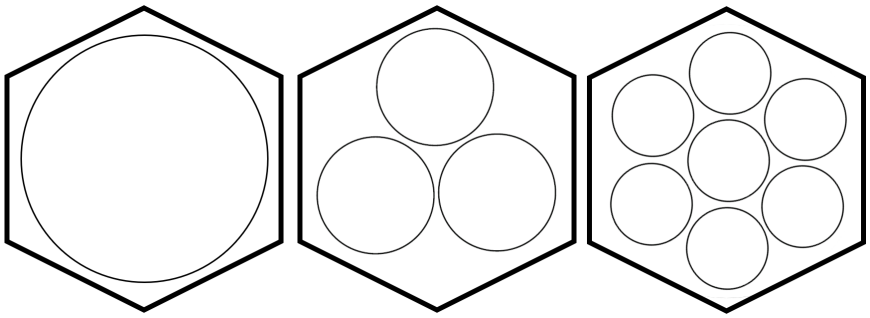

Figure 2.11: Sub-aperture masks for 1 spot (120cm diameter), 3 spots (62cm diameter) and 7 spots (41cm diameter) per segment used for alignment and focusing.

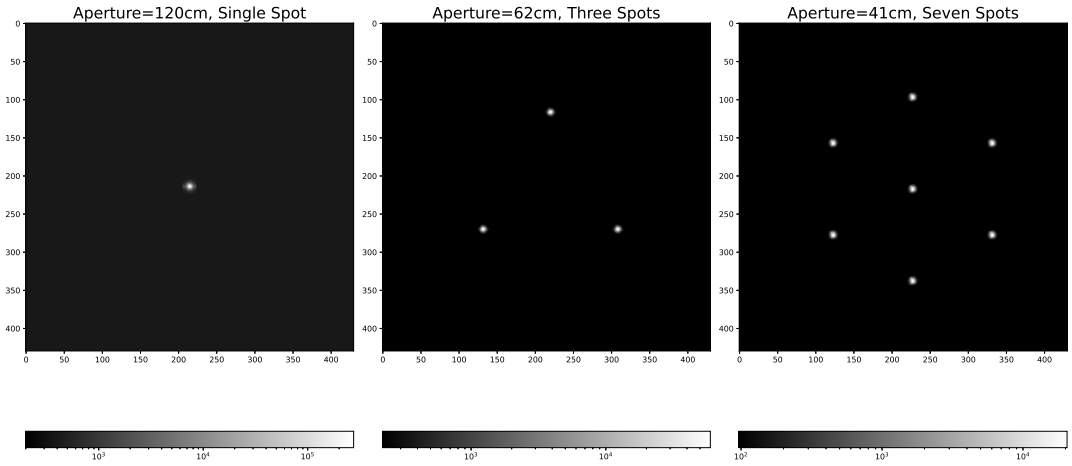

Figure 2.12: Simulated SH spot images (logarithmic normalisation) for single spot (left), 3 spots (middle) and 7 spots (right) per segment. The stellar magnitude is 10 with exposure time of 10sec for an atmospheric seeing of 1arc-sec.

The Atmospheric seeing is a crucial parameter which can very much influence the performance of the APS. Therefore, we have carried out very extensive studies on effect of seeing in measuring the segment tip-tilt errors (Simulations were carried out for three different seeing conditions of 1arc-sec, 1.5arc-sec and 2arc-sec). In all the cases (single and multiple spots), tip-tilt error increases as seeing degrades. For the brighter stars (10 to 13^{th} magnitude), SNR is always very high and centroiding error remains nearly constant. After that, the error increases rapidly when we move to fainter domain. It is observed that under all seeing conditions a single largest sub-aperture gives the least error (Figure 2.13).

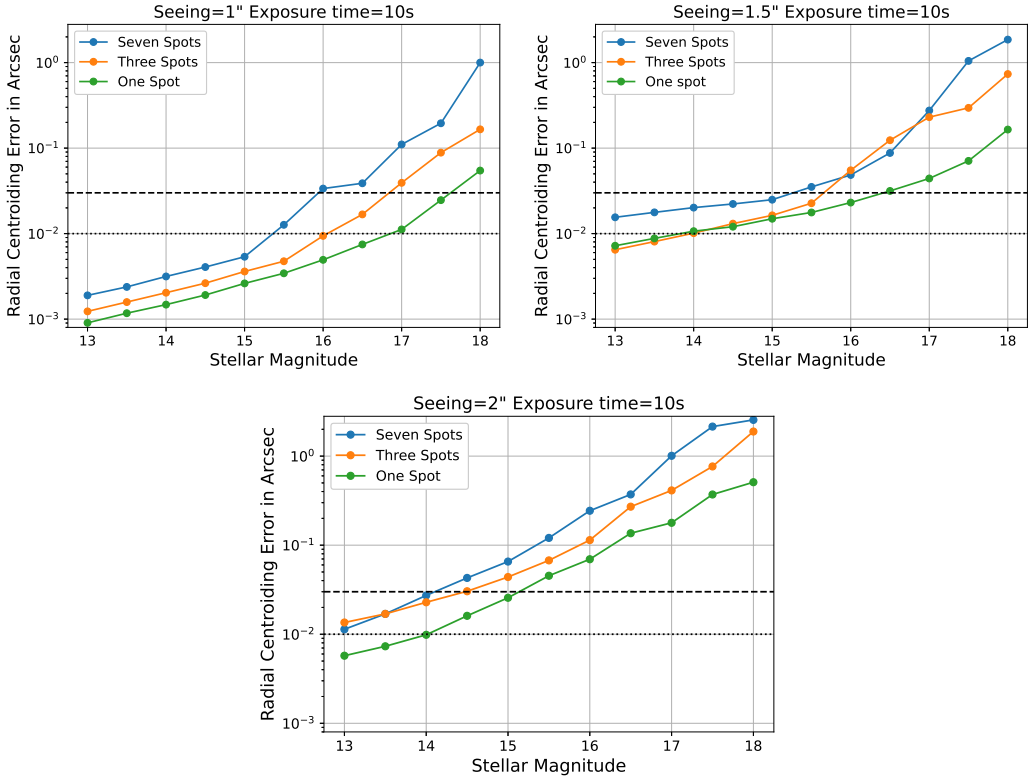

Figure 2.13: Variation of tilt error with stellar magnitude for the exposure time of 10sec with different number of spots per segment (1, 3 and 7 spots) and atmospheric seeing conditions of 1arc-sec (top-left), 1.5arc-sec (top-right) and 2arc-sec (bottom). Dashed line indicates the tilt requirement of 0.03arc-sec for the seeing limited case and the dotted line indicates the tilt requirement of 0.01arc-sec for the diffraction limited case.

For the seeing limited imaging, the tilt measurement requirement of 0.03arc-sec can be achieved by using 17.5, 16 and 14.5 magnitude stars at seeing of 1, 1.5 and 2arc-sec respectively. However, for diffraction limited case, where the requirement is to have tip-tilt error <0.01arc-sec, higher SNR would be needed and hence brighter stars of 13 - 15^{th} magnitude must be used. As far as the tilt error measurement is concerned, the largest aperture with single spot is found to be the best.

In the presence of randomly distributed segment tilt errors, the telescope image obtained is a convolution of the seeing-limited PSF and the PSF due to alignment errors, hence the resultant FWHM can be estimated by quadrature summing of the FWHM values for these two sources of image smearing effect. Therefore, to get a qualitative measure of degradation due to segment alignment error, we have computed the percentage change in the image quality (FWHM) for the largest aperture (120cm) for three different seeing conditions and plotted it against the stellar magnitudes (Figure 2.14). From the plot it is clear that up to 15.5 magnitude the percentage image degradation will not be more than 1% for all the seeing conditions. Which means, alignment error will have no impact on image quality and it is still seeing,

which will supersede. For 1arc-sec seeing, one can use relatively fainter star (17^{th} magnitude) for the tilt measurement. However, with poor seeing like 1.5arc-sec or larger, one needs to use stars of 15^{th} or brighter magnitudes to get the image which is still dominated by the atmospheric seeing and not by segment tilt errors. Here we have considered the total allowed image degradation by all the alignment errors to be about 10% of the seeing.

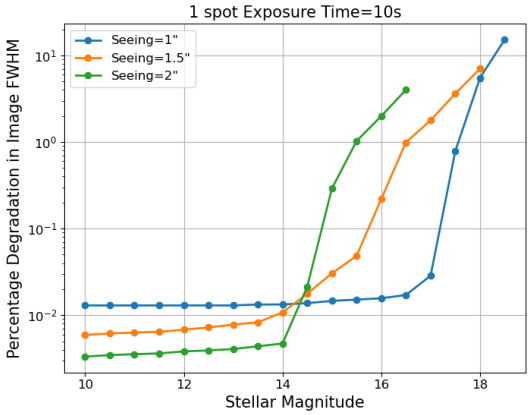

Figure 2.14: Percentage degradation in image quality due to tip-tilt alignment error for seeing limited case.

2.4.4 Simulations on Co-focusing

The co-focusing of the segments deals with the segment ROC errors, which leads to longitudinal displacement of the segment focal point, thus degrading the image quality. If the segment support uses warping harness then the ROC error can be easily corrected by adjusting the segment figure. However, in the absence of warping mechanism, for the seeing-limited telescope the large piston and ROC error can be corrected to some extent by differential movement of the segments (same as classical telescope focusing exercise). The co-focusing of segments also uses the SH sensor. In this case, the SH spots show a radial shift with respect to the reference spots, hence multiple spots per segment would be required. In order to obtain the segment defocus from the spot shifts, first the wavefront slopes are measured and then, through modal wavefront reconstruction method, wavefront error is decomposed using the Zernike polynomials. The Zernike coefficient Z_2^0 corresponds to the defocus aberration and this value is then converted to the longitudinal defocus of the segment (Mahajan, 2013).

Similar to the segment alignment errors, the accuracy of defocus measurement would depend on the spot centroiding accuracy which in turn affects the Zernike fitting. The source of centering error can trace its roots to the poor signal, due to non availability of suitable bright stars, atmospheric seeing, increased background as well as noisy detector. All these sources of errors can individually and/or collectively

influence accuracy of centroid measurement. Therefore, instead of explicitly using all these sources of errors in our defocus related simulation studies, we have used their combined effect in the form of centering error which can be as poor as 1 pixel (15μm) maximum. In order to estimate the accuracy of defocus measurement, we consider an array of 3X3 spots per segment and random centroiding error is introduced for each of these nine spots. Simulated spot positions are then compared with the reference spots and aberrated wavefront is reconstructed. By fitting Zernike polynomials the defocus values represented by Z_2^0 coefficient are obtained for different values of the centroiding errors (over the range of 1/50 - 1 pixel). For each given centroiding error, we have the derived values of Z_2^0 coefficient which are fed to the segmentation tool that generates a grid sag surface for the corresponding RMS defocus error. Finally, the grid-sag surface is imported into our 10m telescope ZEMAX model to derive the image quality related parameters (D50, D80 and Strehl ratio). Figure 2.15 summaries this process of simulations through a flow chart. Figure 2.16 shows the variation of D50, D80 and Strehl ratio values with the centroiding error and corresponding defocus error.

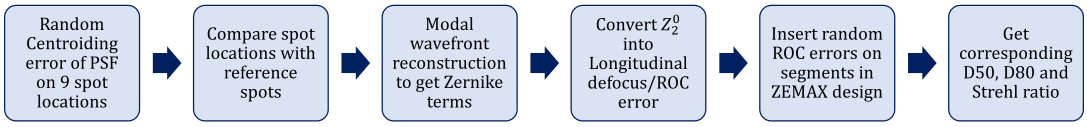

Figure 2.15: Flow chart for deriving the segment co-focus errors from simulated PSFs.

From the simulation results (Figure 2.16) we observe that all three image quality parameters remain nearly unchanged up to ROC error of 25μm. This indicates that the telescope performance remains diffraction limited despite of individual segments being subjected to large ROC error. Further increase in the ROC error gives marginal degradation in the image quality. For diffraction limited imaging, where the Strehl ratio must be > 0.9, the ROC error must be within 150μm.

2.4.5 Simulations on Phasing

After alignment and co-focusing, co-phasing of the segments is crucial for achieving the diffraction-limited image quality. In the case of segment phasing, the piston errors need to be reduced to 30nm or better. After reviewing many phasing techniques such as Keck narrow and broad-band, pyramid, etc., we decided to carry out a detailed study on the Dispersed Fringe Sensor (DFS) and the Optical Transfer Function (OTF) based phasing schemes. The extensive simulations carried out for both these techniques are described in chapter 4 and chapter 5.

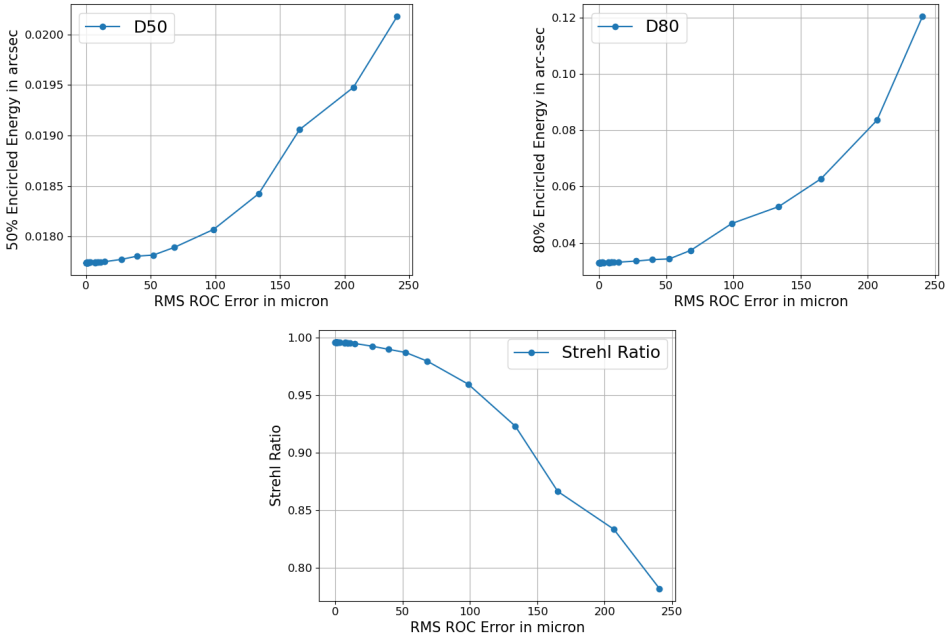

Figure 2.16: Variation of D50 (top left), D80 (top right) and Strehl ratio (bottom) with RMS ROC error.

2.5 Summary

Before designing the APS, it is important to know the alignment and phasing requirements for a 10m telescope. Thus, we started by defining the alignment requirements for the 10m size Indian large segmented telescope. Once the alignment requirements were known, we used Python-based simulations to verify the practicability of the APS. Using the Python-based scripting tool, we have developed a very generic simulation code that can be used to check the performance of any APS. The simulation tool can generate realistic images/spectra for any telescope + APS system. For the tip-tilt and defocus measurements, we have considered a SH wavefront sensor, whereas, for phasing the mirror segments, we have chosen the DFS and OTF-based phasing schemes for our exploration. Using this simulation tool, we predicted the achievable values of tip-tilt, defocus, and piston measurement accuracies for the APS under realistic conditions.

Chapter 3
Development of Segment Alignment Device for PSMT

Development of an alignment device for the Prototype Segmented Mirror Telescope
Radhika Dharmadhikari, Padmakar Parihar, Mohammed Muthahar Rafeeq Ahmed, Govinda Koravangala Venkatapathaiah, Madan Mohan Kemkar, Himanshu Kunjam, **Journal of Astronomical Telescopes, Instruments, and Systems (JATIS)**, Volume 10, Issue 1, 019002 (March 2024)

3.1 Introduction

The Prototype Segmented Mirror Telescope (PSMT) is a 1.3m sized telescope being developed at the Indian Institute of Astrophysics. The primary objective of the PSMT is to get acquainted with the segmented mirror technology and use the knowledge in constructing India's proposed large 10m class segmented mirror telescope. For any segmented mirror telescope, it is important to align the mirror segments very precisely to attain the desired image quality. Thus, we designed and developed a Segment Alignment Device (SAD) for the PSMT. The optical design of this instrument is inspired from the SALT alignment system (Wirth et al., 2004). The task of aligning the segments mainly involves co-alignment (or tip-tilt correction), co-focusing, and co-phasing; the details of each of these procedures are mentioned in section 1.5.

3.2 Prototype Segmented Mirror Telescope (PSMT)

The Prototype Segmented Mirror Telescope is a technology demonstrator of the India's Large Segmented Mirror Telescope. The PSMT project mainly aims to indigenously develop and test the segmented mirror technology within India. The PSMT design has a 1.3m size primary mirror which will be segmented in nature. Thus, we would be able to test the various elements of segmented mirror technology on this

telescope, such as the optical alignment and phasing systems, the electronic control system (which involves edge sensors and actuators) and also the mechanical segment support systems. For further simplifications, we divided the PSMT project into two phases, the first phase is to mainly test the primary mirror control system called the M1CS and the second phase would be the complete 1.3m telescope. Hereafter, we refer to the PSMT phase I as the M1CS test-bed and the phase II as the PSMT. The design details of both the phases are discussed in the following sub-sections.

3.2.1 The PSMT

The PSMT is a full fledged telescope having a segmented primary mirror, with seven hexagonal segments of size 500mm each. The effective diameter of the primary mirror will be 1.3m. To have a simplest optical configuration which can meet the sole requirement of the PSMT as a technology demonstrator, we proposed a two mirror optical design of the telescope. In this design primary mirror is spherical and an oblate ellipsoidal secondary is used to correct very large spherical aberrations introduced by the primary. A rotating tertiary fold mirror is then used to get the dual Nasmyth focus. The primary mirror ROC is 6350.71mm and the telescope F/# is 11. The optical layout for PSMT is given in Figure 3.1 and Figure 3.2 shows the 3-D model for the PSMT. The optical design details of PSMT are given in Table 3.1. The segment alignment device will be placed at the Nasmyth focal plane of the PSMT to facilitate the tip-tilt correction and co-focusing of the segments.

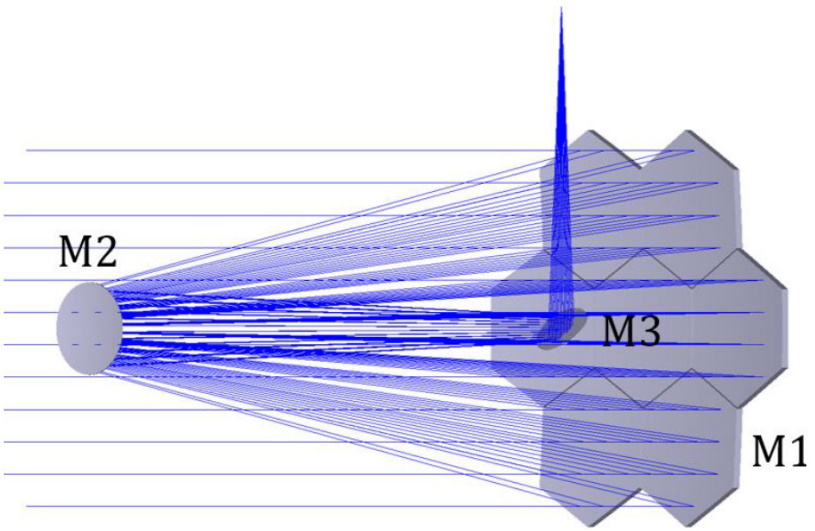

Figure 3.1: Optical Design Layout for PSMT.

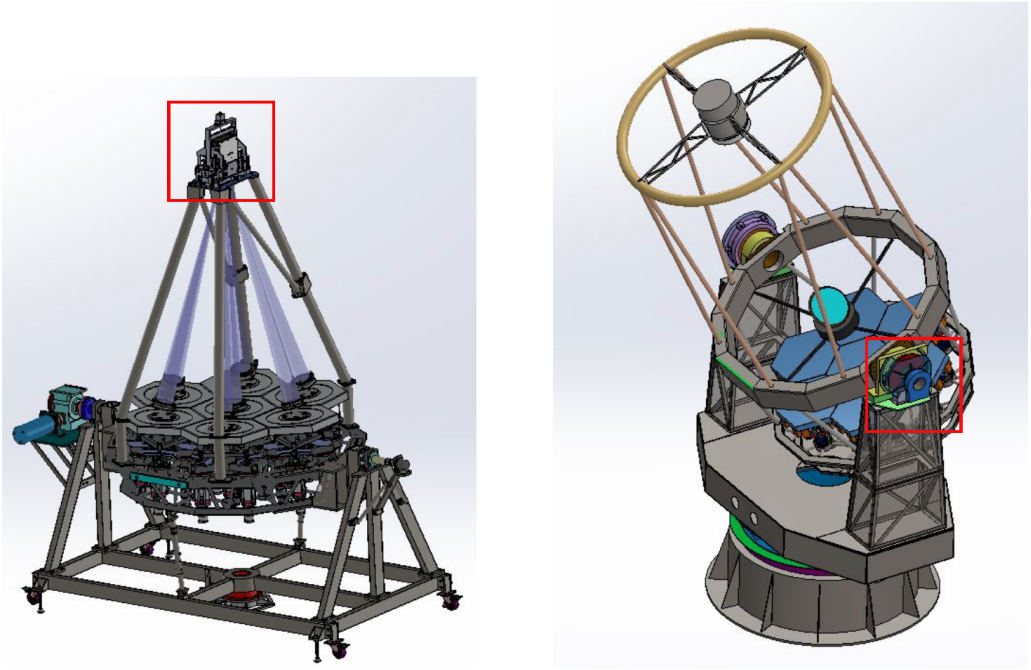

Figure 3.2: 3-D models of the M1CS test-bed (left) and the Prototype Segmented Mirror Telescope (right). Red boxes indicate the position of the segment alignment device.

Table 3.1: Design specifications of the M1CS test-bed and the PSMT optics

Parameter	M1CS test-bed	PSMT
Primary mirror diameter	1m (effective)	1.3m
Segment diameter	100mm	500mm (hexagonal)
Telescope F/#	1.4	11
Primary Mirror ROC	1400mm	6350mm
Placement of SAD	at ROC plane	at Nasmyth focal plane

3.2.2 The M1CS Test-Bed

The M1CS test-bed is the phase I of the PSMT project where, the main goal is to test the performance of the primary mirror control system of the PSMT, including the actual edge sensors, actuators and mirror support system. Thus, to minimize the overall size and cost of the system, we decided to use a compact and simplified system compared to the PSMT. Therefore, instead of using complete PSMT segments with a 500mm diameter and a large ROC of 6350mm, we decided to use smaller circular mirrors with a 100mm diameter and a 1400mm ROC for the M1CS test-bed. A comparison of the design details of the M1CS test-bed and the PSMT is

given in Table 3.1. The M1CS test-bed uses the complete segmented primary mirror system of the PSMT, which includes the mirror cell, seven segment support assemblies, 21 actuators and 24 edge sensors, except the mirror segments. The test-bed uses seven small mirrors of 1400mm ROC and 100mm diameter, which are installed on the segment support systems. Each segment support system is driven by three actuators, and 12 inductive edge senors are mounted on the edges of the segments, as shown in Figure 3.2.

We have designed, developed and extensively tested a SH based segment alignment device, which will be installed at the prime focus of the M1CS test-bed and at one of the Nasmyth focal planes of the PSMT. The details about our alignment tool, its opto-mechanical design and analysis and the test results are presented in the further sections of this chapter.

3.3 Design Requirements for the SAD

An APS is the most basic instrument that any segmented mirror telescope needs, and it is usually a custom-designed and built device. The APS, which we require, should primarily measure the segment tip/tilt as well as focus (and piston) errors precisely and efficiently. The top level design requirements of the PSMT segment alignment device are given in Table 3.2. A large capture range is needed to handle the tilt errors, which may initially be of the order of a few degrees. It must work in two modes, namely, the lenslet/wavefront mode and the imaging mode. Once the mirror segments are tip-tilt corrected and co-focused, the imaging mode will be used to check the PSF quality of the telescope. The PSMT is expected to work in the seeing limited domain without segment phasing; however, we would like to perform on-sky testing of the Keck phasing scheme using at least one pair of segments of the PSMT. Therefore, the device must be able to facilitate the phasing experiment, which may require the use of additional special pupil mask and an optical filter. The device must also have a provision to align the pupil mask precisely with the inter-segment regions on which piston measurements need to be carried out. The instrument should be designed such that the gravity and temperature induced deformations have minimal effects on the measurements. To make the device very cost effective, the design should utilize readily available off-the-shelf components only. All the alignment requirements are derived considering that a 1% degradation in the image quality parameter D80 (which is the diameter for the 80% encircled energy) is acceptable.

3.4 Optical Design and Analysis of the SAD

The alignment device uses a SH wavefront sensor for the segment tip-tilt and defocus measurements. The basic principle of a SH wavefront sensor is that the incident

Table 3.2: Design requirements of the alignment device

Requirement	Value
Tilt Measurement Range:	
With semi-transparent screen	up to 5^o
Coarse Alignment	up to 6arc-min
Fine Alignment	up to 10arc-sec
Tilt Measurement Accuracy:	
Coarse Alignment	<0.20arc-min
Fine Alignment	<0.04arc-sec
Accuracy of defocus measurement	$<5\mu m$ for M1CS test-bed and $<20\mu m$ for PSMT
Temperature range	-25 to 30^oC

wavefront is sampled at multiple positions by a microlens array, which focuses light on the detector plane to give multiple spots. For an ideal plane reference wavefront, the distribution of these spots is uniform, while in the case of an aberrated wavefront, the spot position deviates from the ideal position. Thus, we first record the reference spots, and then the wavefront slope at each point can be obtained by measuring the deviation of each spot with respect to the corresponding reference spot. After obtaining the wavefront slopes, the modal wavefront reconstruction technique (Cubalchini, 1979) is used to obtain the Zernike coefficients.

3.4.1 ZEMAX Optical Design and Analysis

The optical design and analysis of the device were performed using ZEMAX ray tracing software and only off-the-shelf components were used in the design. The initial ZEMAX design was done using sequential mode, where the primary mirror was considered monolithic and subsequently the mixed mode was used, where the seven segments of the primary mirror were designed in the non-sequential mode. After the basic design was completed, we also performed the tolerance and thermal analysis for the device.

3.4.1.1 The Optical Design

For the M1CS test-bed, the Segment Alignment Device (hereafter, M1CS-SAD) will be placed at the ROC plane of the telescope and an external light source will be required for illumination (see Figure 3.3). Thus, the optical design includes a point source placed at the ROC of the primary mirror, which is also the ROC of the reference

mirror. A beam splitter is used to split the light from the source into two parts (the reference arm and the test arm) so that both, the reference and the primary mirror are illuminated. The reflected light from both mirrors is sent to the SH unit, which includes a collimator, a lenslet array and a detector. In the lenslet mode, we obtain an array of spots on the detector plane, which are used for the tip/tilt and defocus error measurements of the primary mirror segments. The reference spots and the primary mirror spots are recorded one at a time. Hence, the light from one of the mirrors needs to be blocked when the measurements are carried out on the other mirror. For this purpose, an electronically controlled, rotating mechanical shutter is used. For the imaging mode, the lenslet is replaced by a doublet lens to get a single image. For this, the lenslet and imaging lens are mounted on a linear actuator that facilitates their movement in and out of the optical beam path. The optical layout for the M1CS-SAD design is shown in Figure 3.3 for the lenslet mode and the imaging mode, and the details of the optical components used are given in Table 3.3.

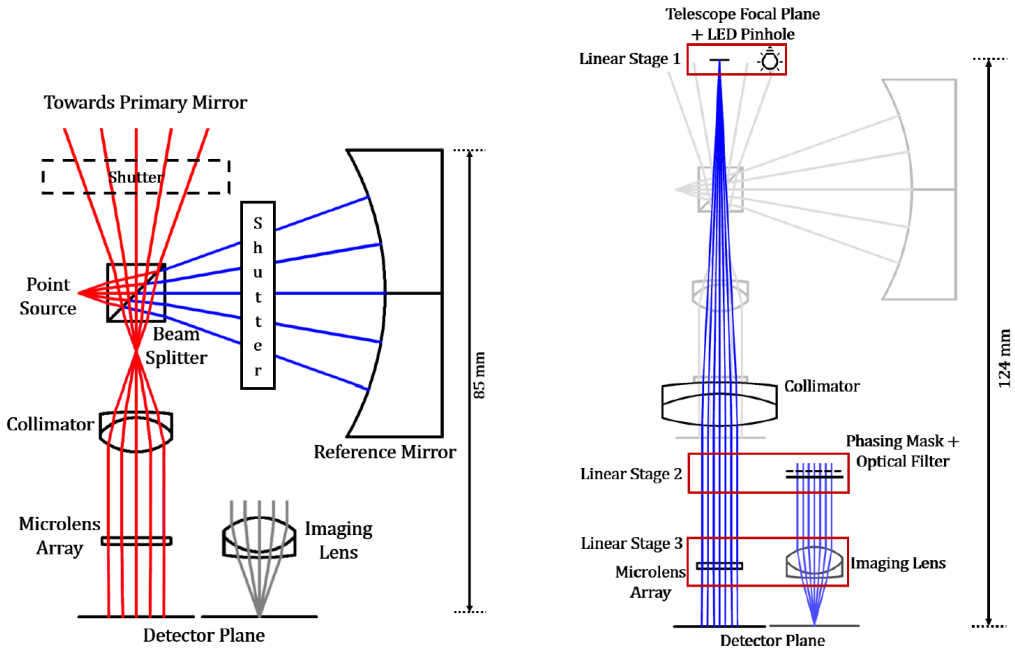

Figure 3.3: Optical layout of the Segment alignment device for M1CS test-bed (left) and PSMT (right). The imaging mode of the device is shown in gray color. For comparison, along with the PSMT-SAD layout, the M1CS-SAD design layout is also shown as a gray watermark.

During the optical design it was observed that since the beam splitter does not receive a collimated beam and the primary mirror has a very fast F number (F/1.4), the beam splitter introduces a large amount of aberrations in the system. Thus, a comparative study was carried out for a cube beam splitter and a Pellicle beam splitter. A Pellicle beam splitter is a thin (2-10μm) nitrocellulose membrane that is

Table 3.3: Specifications of optical components and the detector used in the SAD

Component	Parameter	Specification
LED Source	Wavelength	595nm
Pinhole	Diameter	$10\mu m$
Cube Beam Splitter	Size	10mm
	Glass type	N-BK7
Collimator and Imaging Lens	Type	Achromatic Doublet
	Effective focal length	15mm
	Diameter	12.5mm
Collimator for PSMT-SAD	Type	Achromatic Doublet
	Effective focal length	75mm
	Diameter	25mm
Microlens Array	Pitch	$300\mu m$
	Focal length	14.6mm
Reference Mirror	ROC	50mm
	Diameter	50mm
CMOS Detector	Pixel size	3.45μm
	Resolution	4096X3000
	Quantum Efficiency	67.2% @ 540nm

stretched over a flat metal frame. The ZEMAX analyis confirmed that the Pellicle beam splitter provided close to ideal image quality for the system. However, due to its very thin structure, the Pellicle beam splitter is extremely sensitive to external disturbances and acoustical vibrations, which can make the system performance unpredictable. Additionally, the thin membrane makes cleaning and handling the beam splitter very difficult. Finally, considering all these drawbacks of pellicle beam splitter, a cube beam splitter was chosen for the design. To minimise the aberrations caused by the cube beam splitter, the ZEMAX design was optimised by adjusting the beam splitter thickness and the separation between the source and the primary mirror. The mirror segment used in the M1CS test-bed is circular in shape, and its diameter is 100mm. The seven 100mm segments fill the primary mirror diameter sparsely, and only 9 spots per segment can be accommodated. The spot diagrams for the reference mirror and the primary mirror of the M1CS-SAD are shown in Figure 3.4 and Figure 3.5. In the imaging mode of the M1CS-SAD design, the RMS spot radius with the reference mirror is 18.3μm, and that with the segmented primary mirror is 13.58μm. Figure 3.3 shows the optical layout when the device is used in the PSMT telescope.

The design of the PSMT segment alignment device (hereafter referred to as the

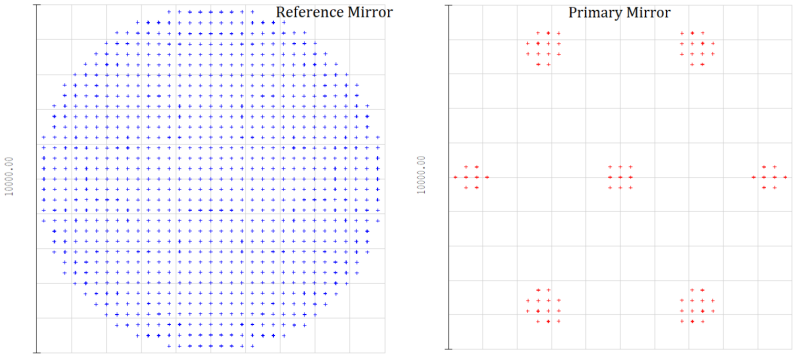

Figure 3.4: Spot diagrams for reference (left) and primary mirror (right) in lenslet mode for M1CS test-bed.

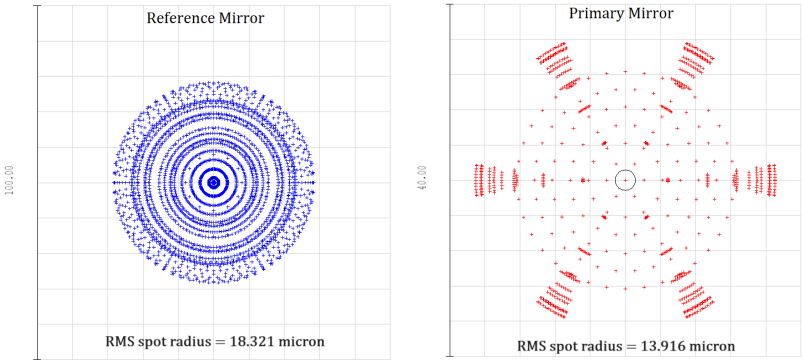

Figure 3.5: Spot diagrams for reference (left) and primary mirror (right) in imaging mode for M1CS test-bed.

PSMT-SAD) requires slight modifications due to the large difference in the F-numbers for the M1CS test-bed and the PSMT telescope (for the M1CS test-bed, the F/# is 1.4, while for the PSMT, it is ∼11). Thus, the collimator lens is replaced by a doublet with a larger focal length. Additionally, for PSMT, the alignment device will be placed at the telescope focal plane, and the primary mirror will be illuminated by the star light; hence, we do not require the beam splitter and the reference mirror. The reference spots for this mode will be obtained by placing an LED + pinhole source at the telescope focal plane. Since we also plan to use the same device for conducting the Keck phasing experiment with at least one pair of PSMT mirror segments, an additional pupil mask, optical filter and imaging lens will be needed in the optical train. The mask is expected to block the light from all parts of the pupil except from one of the inter-segment regions. The pre-aligned mask and a filter can be placed on a single linear stage. Finally, the image is formed on the detector plane by a precision doublet lens installed on another linear stage along with the lenslet array (see Figure 3.3).

Using the values of the parameters from the design, we calculated the achievable tip-tilt alignment accuracy and range for both the M1CS-SAD and the PSMT-SAD. Theoretically, the tilt measurement accuracy depends on the lenslet focal length, while the range of the device depends on the lenslet pitch (which is 300μm for our case) and the focal length. However, under practical conditions, many external factors, such as atmospheric turbulence and extinction, external noises and detector induced noises can affect the SNR as well as the measurement accuracy of the system. Therefore, to obtain a realistic estimate of the achievable accuracy of the device, we used our Python-based simulation code, which generates realistic images for any telescope + alignment system and can be used to obtain the achievable accuracy (chapter 2). The obtained values of accuracy and range for the designed device are given in Table 3.4.

Table 3.4: Calculated accuracy and measurement range of the alignment device in the coarse and fine modes

Alignment Mode	Parameter	M1CS test-bed	PSMT
Coarse Alignment mode	Tilt accuracy	0.0127”	0.0121”
	Tilt Measurement Range	±6.353’	±6.065’
Fine Alignment mode	Tilt accuracy	0.0041”	0.00169”
	Tilt Measurement Range	0.1796’	0.1714’
Defocus	Measurement Accuracy	1.7563μm	45.63μm

3.4.1.2 Tolerance Analysis

For any instrument design, it is important to know the allowable values of errors that might be introduced practically while manufacturing and assembling its components. Since all the optical elements used in our design are readily available off-the-shelf components, the manufacturing tolerances are fixed as provided by the manufacturers. To determine the permissible alignment errors, we performed a tolerance analysis using ZEMAX. Since we planned to use off-the-shelf optical components only, therefore, standard tolerancing values of the element tilt, decenter and thicknesses were considered in the analysis. The imaging mode of the device was used for the tolerance analysis, and we had three compensators: i) the separation between the primary mirror and the beam splitter, ii) the separation between the reference mirror and the beam splitter, and iii) the separation between the imaging plane and the imaging lens (i.e. adjustable focus). The tolerance values considered for different components are tabulated in Table 3.5.

From the tolerance analysis it was found that the ROCs of the optical components, such as the collimator lens, reference and primary mirrors, and the separation between the source and the beam splitter are the most sensitive parameters in the

Table 3.5: Parameters used for tolerance analysis in ZEMAX

Parameter	Tolerance Value
Primary mirror ROC for M1CS test-bed	±2.5mm
Primary mirror ROC for PSMT	±6mm (±0.02%)
Reference mirror ROC	±2mm
Doublet lens (Collimator and Camera):	
ROC	±1%
Center thickness	±0.1mm
Element Tlit	±15arc-min
Element Decenter	±0.1mm
Thickness	±0.1mm

design. For the M1CS-SAD design, the nominal value of the RMS spot radius was $18.321\mu m$. From the Monte Carlo tolerance analysis, we obtained a mean RMS spot radius of $18.402\mu m$, which corresponds to only a 0.44% increase from the nominal value. Similarly, for the PSMT-SAD design, the percentage increase in the RMS spot radius is found to be 1.41% from the nominal value.

3.4.1.3 Thermal Analysis

In the device, the reference beam is created internally, and due to varying ambient temperature, it is quite possible that the location of the SH reference spots may change, which in turn can affect the segment tilt and defocus measurements. Therefore, to understand the effect of temperature, thermal analysis was carried out in ZEMAX for the device when it works in the M1CS test-bed as well as for the PSMT. Since the M1CS test-bed is a laboratory setup, the nominal temperature was considered to be 20^oC with a variation of $\pm 20^oC$. In order to understand how each of the components affects the performance, we divided our analysis into five cases. In Case 1, only the reference mirror parameters were varied with temperature and all the other parameters were kept constant. For Case 2, only the beam splitter was considered; in Case 3 the collimator and lenslet array were considered; in Case 4 the effect of the Aluminum base plate was considered and finally, in Case 5, all these components together were considered for the thermal analysis. For each of these cases, the shift in the reference spots with respect to the nominal position was obtained through ZEMAX. These spot shifts were then further converted to the corresponding segment defocus, tip and tilt errors through modal wavefront reconstruction. From our analysis, we found that the tip-tilt errors introduced were of the order of a few milli-arcsecs; hence, they would have a negligible effect on the alignment measurements. The variations in the defcous

errors for five different cases with temperature are shown in Figure 3.6. The temperature effects of the base plate and other optical components were found to be working in opposite ways. Figure 3.6 clearly shows that the beam splitter is the most sensitive component in the entire design.

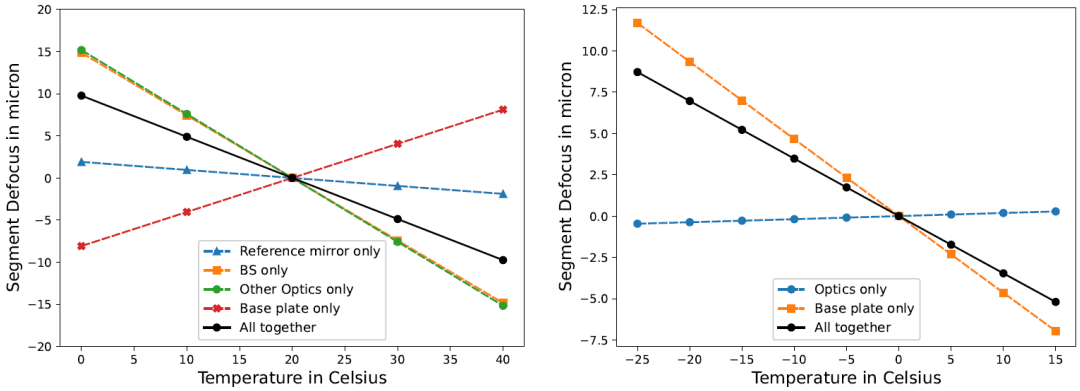

Figure 3.6: Variation of segment defocus error due to temperature changes for M1CS-SAD(left) and the PSMT-SAD (right).

Similar to the M1CS test-bed, for the PSMT-SAD also we considered three cases. In Case 1, only the optical effects were considered, for Case 2, the base plate was considered and for Case 3, all the components were considered together. The nominal temperature for the PSMT analysis was considered to be 0^oC and the variation was considered to range from -25^oC to 15^oC according to the Indian Astronomical Observatory (IAO), Hanle which is the proposed site for PSMT. The obtained segment defocus error for each case is shown in Figure 3.6. The image quality degradation that occurred due to the change in temperature was found to be $< 0.05\%$ for all the cases, which lies well within the tolerance limits of the telescope image quality.

3.5 Mechanical Design and Electronic Control

3.5.1 Mechanical Design and Alignment Requirements

The mechanical design of the device was carried out using the CAD software - SolidWorks. A small optical bench made of aluminum holds all the optical components, which comprises a reference mirror, a cubic beam splitter, a lenslet array, an imaging lens, an LED based light source and a CMOS based imaging device. Almost all optical components are mounted on customized holders, which are precision made according to the optical tolerances. The imaging lens and the lenslet array are installed on a linear translation stage driven by a stepper motor, whereas the shutter, which selectively blocks the light, is installed on the motorized rotation stage. Separate home and limit switches are used to provide reference positions as well as travel limits for

the linear stage, whereas for the shutter, which usually works in On/Off mode, only limit switches are used. An LED light source is used for which the illumination can be changed as per requirement. The reference mirror is held on a stationary mount. The mount for the CMOS camera and reference mirror has a provision to manually adjust for any small changes in the instrument focus. The whole optical bench is covered with five side walls. The controller and the stepper motor driver electronics are also kept inside the device and any heat generated by the electronics is directed out by using a fan. For the M1CS test-bed experiment, the alignment device is installed at the prime focus mount, as shown in Figure 3.2. The mount at the prime focus has five degrees of freedom, four of which are passive and one is active. During the initial installation, the device is aligned with respect to the primary mirror using passive tip/tilt and X-Y decenter stages, which have micrometers. The light injected from the M1CS-SAD will return after reflection from the segmented primary only when the device is properly aligned. The fifth axis is for focusing the device (adjusting the distance between the primary mirror and the M1CS-SAD), and it is motorized. The mechanical alignment range requirements of the device are given in Table 3.6. The three-dimensional mechanical design models of the full device and realized device are shown in Figure 3.7.

Table 3.6: Range and Fine adjustment requirements for the mechanical alignment for the SAD

Parameter	Required range	Required alignment accuracy
X-Y tilt	$\pm 5^o$	$\pm$1arc-min
X-Y decenter	$\pm$5mm	$\pm$0.1mm
Focus	$\pm$5mm	$\pm 10\mu$m

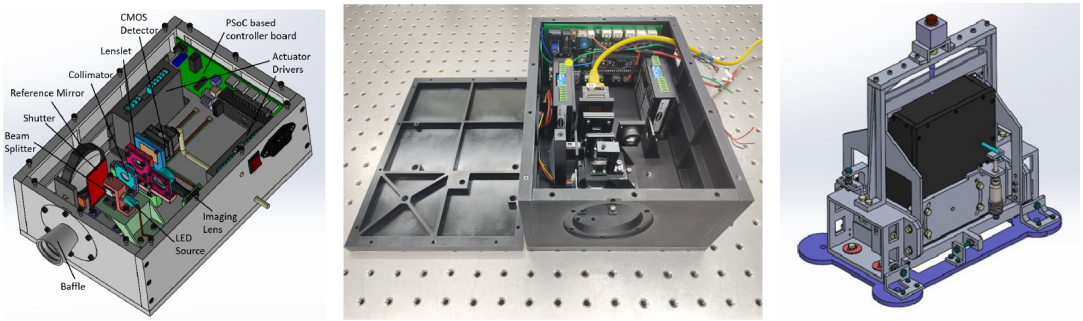

Figure 3.7: Three dimensional mechanical model of the alignment device (left) and the realized device (middle). 3D model of the alignment device installed with the 5 axes mount (right).

3.5.2 Electronic Control of the Device

The alignment device requires a few moving elements, such as translation and rotation stages, a stepper motor based instrument focus drive, an LED controlling mechanism and operation of a CMOS based imaging camera. Therefore, a customized controller hardware and a Python-based software have been designed and developed. The heart of the electronics board is the Programmable System on Chip (PSoC) which can simultaneously operate three stepper motor based stages. Figure 3.8 shows the block diagram for the PSoC based controller. In the M1CS-SAD, only one linear actuator will be used for moving the imaging lens and the lenslet array in and out of the optical beam path. Another requirement of the test-bed is to block the light from either the reference mirror or the primary mirror by using a motorized rotating shutter. Apart from this, when the device is used in the PSMT telescope, two additional linear actuators would be required. One for selecting filters for the Keck kind of phasing and the other for bringing the reference LED source in and out of the telescope focal plane so that reference and primary mirror SH spot images can be recorded. The controller not only turns the LED on/off but also controls the brightness of the LED by varying its voltage using a MOSFET based switching electronics and PWM. For the initial semi-transparent screen based manual alignment, very bright illumination will be needed, whereas for the SAD based, coarse and fine tip-tilt correction modes, the same LED will be used with comparatively less brightness.

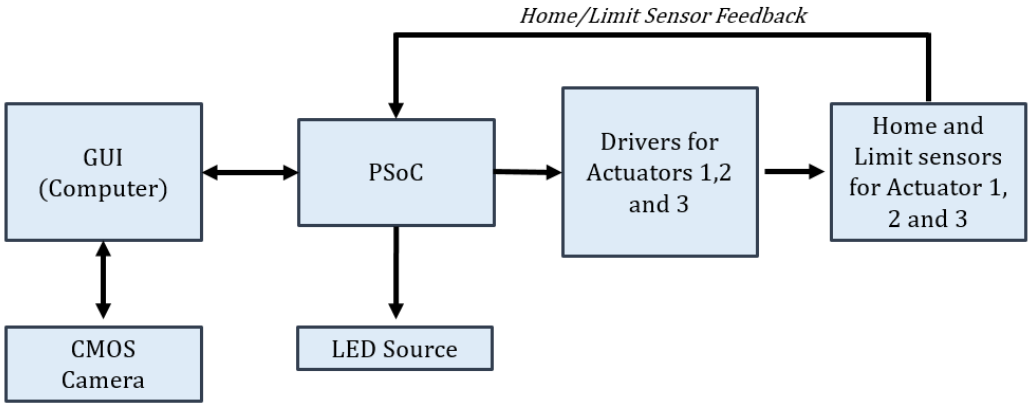

Figure 3.8: The block diagram showing the control of the instrument.

The instrument control software, which runs on the computer was developed using Python scripting language. A GUI has also been developed to make the device operation simple and user friendly (see Figure 3.9). The CMOS camera, which uses an Ethernet based interface is also operated using a Python code and the GUI. The GUI allows the user to control different aspects of the instrument, such as switching LED power, moving the actuators to select the imaging or lenslet mode, and setting

up the detector specifications such as the exposure time and gain etc. Once the device setup is complete, images can be captured and analysed through the GUI. The GUI provides an option for interactively examining the captured images and checking the image quality. Once the image quality of the reference and primary mirror images is found to be satisfactory, then modal wavefront fitting can be applied to obtain the first 10 Zernike coefficients. The GUI can display the results of the wavefront fitting as a vector plot, wavefront error map and bar graph showing the values of the Zernike coefficients. Finally, one can extract segment specific alignment and focusing errors.

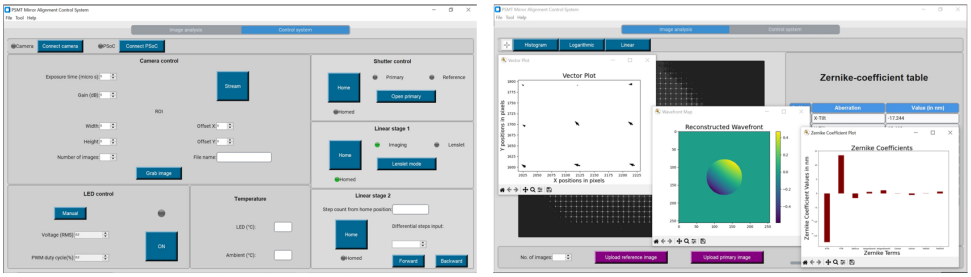

Figure 3.9: Snapshots of the Python-based GUI for device control.

3.6 Operation of the Device

The alignment device is meant for the measurement of small tip-tilt errors with high accuracy. However, during the initial setup, the amount of misalignment may be higher which will fall outside the measurement range of the device. To solve this issue, we plan to complete the alignment process in three successive steps, starting from large errors and then proceeding to coarse and fine alignment. For the preliminary alignment, we estimated the segment tilt error to be up to $\pm 5^o$. For such a case, the beam from the mirror would not enter the alignment device. Hence, to handle this condition, we plan to use a semi-transparent screen kept in front of the alignment device such that the light reflected back from the segments can be visually observed on the screen and the segment tilts can be minimised by manual observation with the naked eye (see Figure 3.10). Thus, for the M1CS-SAD design, in ZEMAX, a surface was added at a distance of 30mm before the beam splitter, which would be the approximate position of the screen. For this surface, the spot diagrams for the center and outer segments were studied for different tilt angles. Since the screen is not at the ROC plane, the spots from each of the seven segments would be finite in size. The calculated diameter of each of the spots was 3.12mm on the screen plane. Similarly, for the PSMT-SAD design, star light will be used for alignment; hence, the screen will be placed at the telescope focus and a bright star will be used for the initial screen-based alignment.

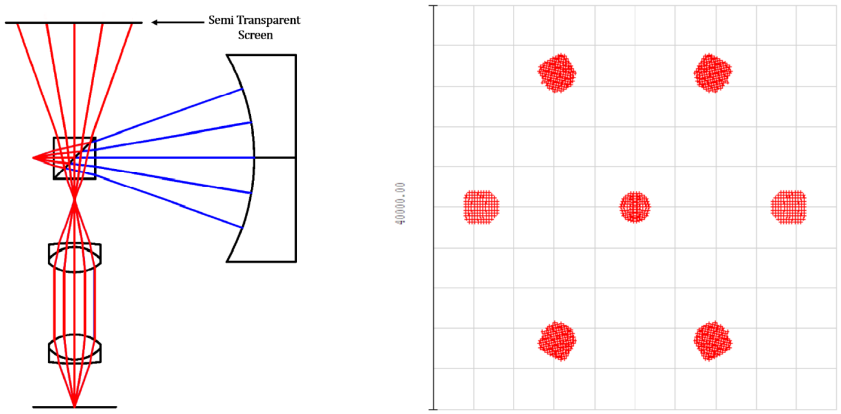

Figure 3.10: Location of semi-transparent screen (left) and spot diagram on the screen plane (right).

After completing the initial alignment with the help of the semi-transparent screen, we estimate the tilt error to be of the order of a few arc-minutes; however, this value lies beyond the capture range of the lenslet mode of the M1CS-SAD. Hence, for this coarse tip-tilt correction, we will use the imaging mode of the device. Thus, the seven spot images formed by each segment can be stacked together to bring the tilt errors within the capture range of the lenslet mode. Finally, the fine alignment mode (which uses 9 spots per segment for M1CS and 49 spots per segment for PSMT) will be used. For the M1CS test-bed, one spot corresponds to a sub-aperture diameter of 28mm on the segment and for the PSMT, we have 49 spots per segment, which correspond to a sub-aperture diameter of nearly 57mm on the segment. With such a large number of spots, the device can easily measure the higher order aberrations for the primary mirror but the PSMT segment support does not have a warping harness. Hence, the higher order aberrations cannot be corrected. Therefore, we restrict the measurements to the tip, tilt and defocus only.

3.7 Testing the SAD in the Laboratory

3.7.1 Lenslet tests

The lenslet array used in the device is from Thorlabs (model number MLA 300-14AR-M). Before using the microlens array in the segment alignment device, it was important to check its quality as well as its actual focal length because the focal length of the micro-lens array affects the device plate scale, which in turn determines the tilt measurement accuracy and range. However, lenslet image quality can influence the centroiding accuracy. Hence, we used the spherical wavefront calibration technique, mentioned in Kumar, Narayanamurthy, and Kumar (2013), to test and verify the focal length of the lenslet array. For the spherical wavefront test, a point source is placed

at a precisely known distance from the lenslet and the corresponding spot array is recorded. The same is repeated for different values of separation between the source and lenslet. For each given separation, the spacing between any two adjacent spots is related to the curvature of the incident wavefront; hence, this spacing can be related to the focal length of the lenslets given by equation Equation 3.1.

$$f = \frac{(Q_1 - P)(Q_2 - P)}{(Q_1 - Q_2)P}\Delta R \tag{3.1}$$

here, f is the lenslet focal length, Q_1 and Q_2 are the separations between two adjacent spots in the image for two different source positions, P is the pitch of the lenslet and ΔR is the separation between the two positions at which the images were recorded. The experimental set-up for the spherical wavefront test is shown in Figure 3.11. From this experiment, we found that the actual focal length of the lenslet is 15.38mm, which is slightly different from the manufacturer specified value 14.6mm. Therefore, the complete design and analyses was repeated with this new measured focal length. With the new measured focal length, the measurement accuracy of the device reduced by 5% as compared to that calculated using the focal length specified by the manufacturer.

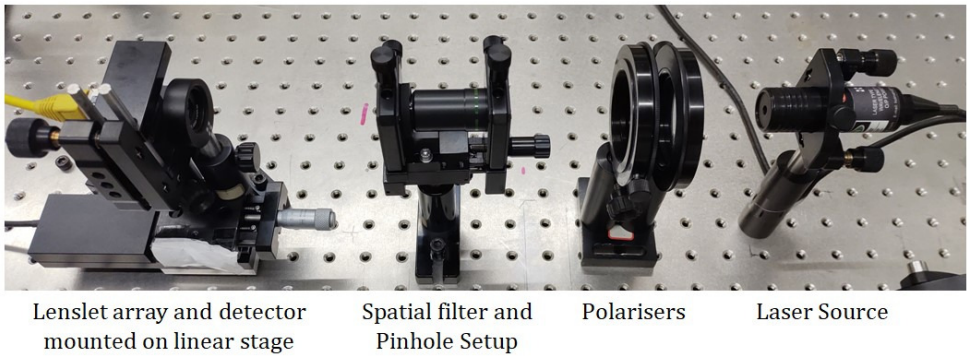

Figure 3.11: Experimental setup for the spherical wavefront to test the lenslet array.

Another important test conducted for the lesnslet was to check its image quality. For this purpose, the lenslet was illuminated with a LASER generated uniform collimated beam, and the focused spot arrays were recorded. The calculated FWHM for the lenslet spots was 24.67μm whereas, the measured average FWHM value from the recorded spots was found to be 24.45$\pm$ 0.29μm, which closely matches the calculated value. Almost all spots of the lenslet array showed similar FWHM (variation of approximately 1.2%). The illumination of all the spots also matches, showing less than 14% variation in the peak value of the intensity. Therefore, we can conclude that despite being an off-the-shelf component the lenslet array used in the device is of good quality.

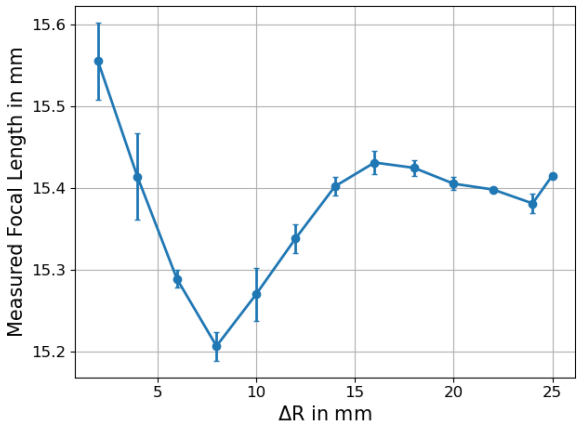

Figure 3.12: Variation of measured focal length with separation ΔR.

3.7.2 Testing the Device With a Single Segment

To test the working of the device and to determine the practically achievable measurement accuracy, we tested the device with a single segment (100mm in diameter) in the laboratory. The tilt and defocus measurements were made separately for the segment. In order to apply the defocus error, the alignment device was kept stationary on the optical bench and a segment was mounted on a precision Thorlabs linear stage that was moved along the optical axis. For the tilt measurements, a custom built, very high precision tilting stage was used. A schematic of the custom built tilt stage is shown in Figure 3.13.

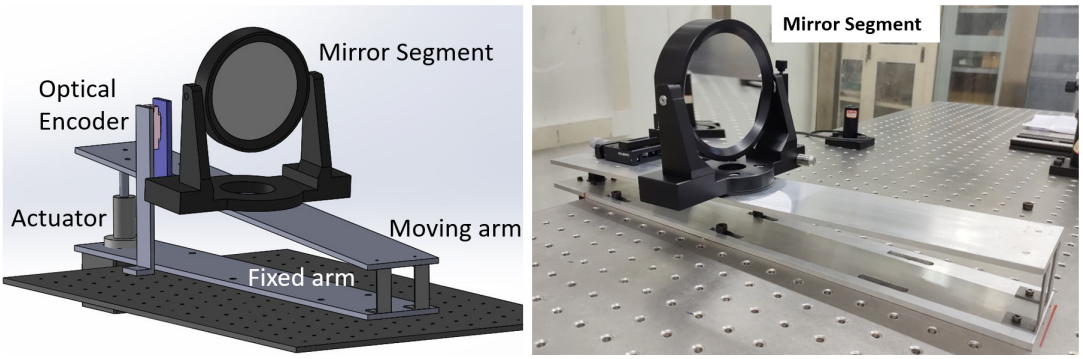

Figure 3.13: The customized high precision tilt mount used to conduct laboratory testing of segment alignment device.

The stage has two flat arms that are nearly 0.5m in length, one fixed and the other rotating about a pivot connecting the two arms. A stepper motor based linear actuator is interfaced at the other end of the pivoted arm which moves vertically, so that the segmented mirror mounted on it is tilted by a very small amount. By using a very high micro-stepping drive and an extremely high resolution optical encoder

(1.2nm), we could introduce very small tilt of the order of 0.01arc-seconds. The results obtained from the tests conducted to check the tilt and defocus measurement accuracies of the device are given in the subsequent sections.

3.7.2.1 Results Related to the Measurement of Segment Tilt Alignment

Using the tilt mount, we applied tilt of different amounts to the segment and for each case recorded the SH spots using our device. Introducing a few milli arc-seconds of tilt by using a very inexpensive customized device was indeed a challenging task; hence, a number of precautions were taken, such as maintaining the laboratory temperature and conducting experiment swiftly and in large numbers, on different days to ensure its repeatability. Further, the duration of the experiment was kept as small as possible to avoid the effects of any external disturbances. Additionally, the use of a very high precision external encoder helped to improve the measurement accuracy of the customized tilt mount. The recorded spot images (see Figure 3.14) were then compared with the reference spot locations to get the wavefront slopes. Figure 3.15 shows the vector plots in which the arrows represent the shift of the segment spots with respect to the reference mirror spots in presence of tilt errors of 0.5 and 1arc-sec.

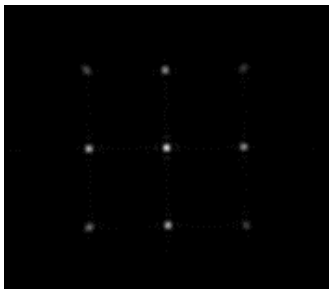

Figure 3.14: Real spot image captured during the experiment.

The wavefront slopes were further used to get the Zernike coefficients for the system using the modal wavefront reconstruction (Cubalchini, 1979). We plotted the applied tilt values (obtained from the encoder readings) against the measured tilt values (see Figure 3.16). The experiment was repeated for three different step sizes (0.021", 0.107" and 0.215"). After fitting a linear regression to this data, we found the slopes and the RMS values for different step sizes (see Table 3.7). As expected, the slopes were found to be close to unity. Whereas, the RMS values varied from 0.0148 to 0.0164arc-seconds. Considering that the applied tilt is error free, the RMS values can be treated as the tilt measurement accuracy of our segment alignment device. The average tilt measurement accuracy of the device turns out to be 0.015", which is found to be better than the design requirement but higher than the calculated accuracy of 0.0041". The difference between the measured and calculated accuracy

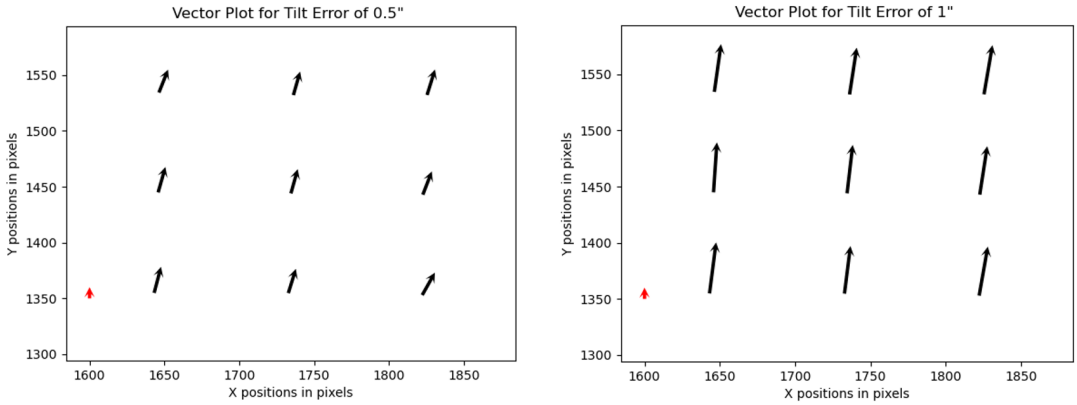

Figure 3.15: Vector plots showing the movement of primary mirror spots with respect to reference spot positions for tilt errors of 0.5 and 1arc-sec. Red arrow indicates a shift of 1 pixels (arrows scaled by 10 times).

can be probably linked to our tilt mount, which certainly has limitations on the smallest step size and stability. Therefore, by using a more precise tilt mount, the extreme performance of the segment alignment device can be checked.

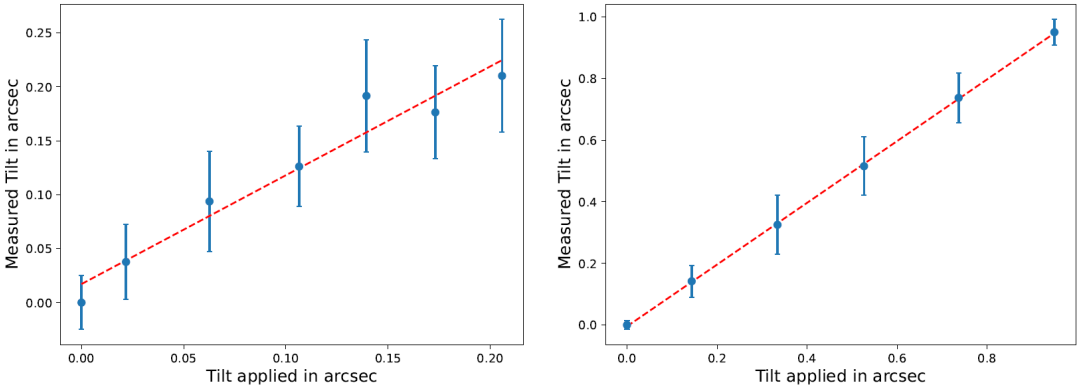

Figure 3.16: The measured vs applied tilt with step sizes of 0.021” (left) and 0.215” (right).

Table 3.7: Results of tilt measurement experiment carried out in the laboratory

Step Size	Fit Slope	RMS Error (in arc-sec)
0.021”	1.048	0.0148
0.107”	1.009	0.0164
0.215”	1.0908	0.0153

3.7.2.2 Results Related to Segment Defocus Measurement

To check the performance of the device for defocus measurements, the segment was mounted on a linear Thorlabs stage, and defocus was applied using different step sizes (2μm, 5μm and 10μm). For each case, the SH spots were recorded and the modal wavefront reconstruction was used to obtain the Zernike coefficients. Figure 3.17 shows the vector plots where the radial movement of the spots can be seen for different values of defocus errors. The Zernike coefficient Z_2^0 corresponds to the defocus aberration and this value was then converted to the longitudinal defocus of the segment (Mahajan, 2013). The measured longitudinal defocus can be directly compared with the applied defocus. Therefore, the measured values of defocus were then plotted against the applied values and a straight line was fitted to the data points (Figure 3.18). The slopes and the corresponding RMS values are given in Table 3.8. Again, considering that the RMS value characterizes measurement accuracy, we found that the average defocus can be measured with an accuracy of nearly 1.82μm, which is close to the predicted value of defocus measurement, as mentioned previously in Table 3.4. Here, we should note that the Thorlabs linear stage (model MTS25/M-Z8) used in this experiment is driven by a BLDC servo motor. And it can move the stage in any direction with a minimum achievable incremental movement of 0.05μm.

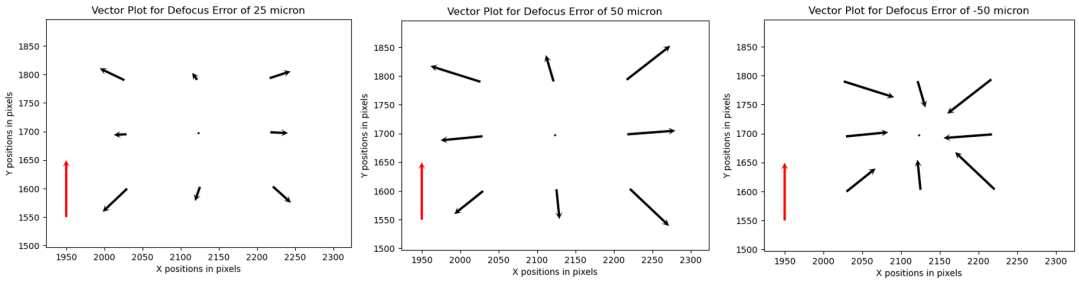

Figure 3.17: Vector plots showing the movement of primary mirror spots with respect to reference spot positions for defocus errors of 25μm(left), 50μm(center) and -50μm(right). Red arrow indicates a shift of 1 pixels (arrows scaled by 100 times).

Table 3.8: Experimental results for the defocus measurement

Step Size	Fit Slope	RMS Error (in μm)
2μm	1.22	1.686
5μm	1.05	1.82
10μm	1.05	1.955

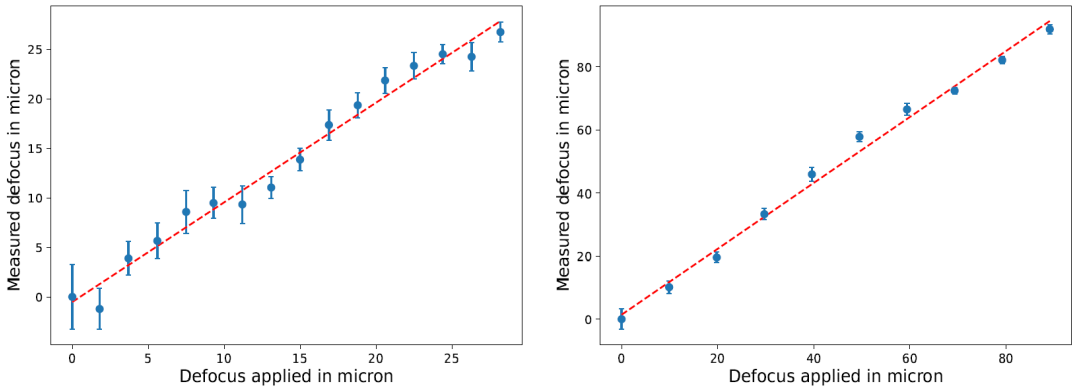

Figure 3.18: Measured vs Applied defocus for step sizes of 2μm(left) and 10μm(right).

3.8 Summary

The PSMT is a 1.3m aperture, seven-segment telescope being developed as a technology demonstrator for India's large optical-IR telescope project. A SH sensor-based alignment device has been designed and developed for the PSMT. The device helps in the tip-tilt correction and co-focusing of the mirror segments. It is designed to work primarily in two different modes: the SH mode and the imaging mode. After completion of the alignment procedure, the final image quality can be checked in the imaging mode. It also has a provision to conduct the Keck phasing experiment with one pair of mirror segments. To make the device cost-effective, only off-the-shelf components are used. The optical design and opto-mechanical analysis of the device were carried out using ZEMAX and SolidWorks software. Then, after careful design, fabrication, and assembly, the device went through extensive testing in the laboratory for tip-tilt and defocus measurements using a single small mirror segment. The device is found to outperform in laboratory tests and is expected to easily meet all the requirements of tip-tilt measurement and co-focusing when installed on the telescope. The segmented mirror telescope is the most preferred way to construct medium to large-size telescopes, in which the APS plays a vital role; from this work, we have shown that despite being a very important and essential instrument, an SH-based alignment tool can be easily built.

Chapter 4
Phasing With the Dispersed Fringe Sensor

Building a large affordable optical-NIR telescope (I): an alternate way to handle segmented primary mirror
Radhika Dharmadhikari, Padmakar Parihar, Annu Jacob, **Experimental Astronomy**, Volume 56, pages 569–604, (2023)

The Dispersed Fringe Sensor for coarse and fine phasing of mirror segments
Radhika Dharmadhikari and Padmakar Parihar, **Under Preparation**

4.1 Introduction

Co-phasing of mirror segments is an important task that ensures that the piston errors are reduced to the orders of a small fraction of the observing wavelength. To achieve the resolution equivalent to that of a monolithic primary mirror, the mirror segments must be co-phased. Multiple phasing techniques have been developed and demonstrated by different groups to achieve the phasing requirements. All of the existing phasing techniques have a substantial trade-off between their measurement range and accuracy. Hence, they are classified as coarse and fine phasing techniques (subsection 1.6.1). The coarse phasing techniques have a large measurement range (a few tens to hundreds of microns) but low measurement accuracy (of the order of $\lambda/10$). In contrast, the measurement range for the fine phasing techniques is limited to $\pm\lambda/4$, but they have very high accuracy (of a few nano-meters). Thus, all the existing telescopes are bound to use two different techniques for coarse and fine phasing of mirror segments.

The Dispersed Fringe Sensor (DFS) is one such phasing technique that is conventionally used for coarse phasing; however, recently Li, Wang, and Rao (2017) and Li and Wang (2022) have proposed that by opting a slightly different methodology, the DFS can also be used for fine piston measurements. Therefore, in addition to explor-

ing the classical coarse phasing scheme, we have also carried out extensive simulations and laboratory experiments on fine phasing using the DFS. In this chapter, we discuss the results obtained from the simulations and experimentation.

4.2 The DFS-Based Phasing

The dispersed fringe technique is primarily based on the principle of Rayleigh Interferometry. The Rayleigh Interferometry technique states that in presence of an Optical Path Difference (OPD) between two collimated beams, the PSF shows a splitting and the positions of the two peaks of the PSFs are a measure of the OPD (Wang, Zhu, and Cao, 2009). The DFS works on the same principle, however to enhance the capture range, it uses a broadband source and a dispersive element (such as a grating or grism (Smith et al., 2003; Shi et al., 2004a).

Figure 4.1 shows a schematic of the DFS based phasing system. The light from the telescope focal plane passes through a collimating lens giving a parallel beam which consists of a sub aperture mask that samples light from the inter-segment edges. Each sub aperture mask is followed by a prism which is responsible for deviating the light from each of these inter-segment regions so that the fringes formed by each inter-segment region are separated on the detector plane. After this a dispersion element (grating/grism) is used to introduce the wavelength dependent dispersion. Finally, an imaging camera is used to form DFS images on the detector plane.

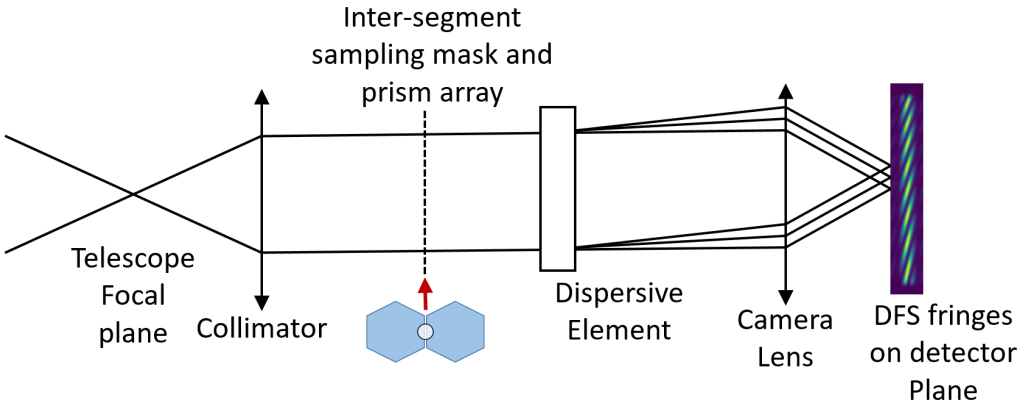

Figure 4.1: Schematic diagram illustrating the principle of DFS based segment phasing technique.

The resultant intensity pattern on the detector plane is a continuous source spectrum modulated by sinusoidal fringes. The frequency and tilt of these fringes are found to be proportional to the piston error. Under the zero piston error condition, DFS would give a continuous spectrum. The intensity distribution for the DFS fringes has been derived in Shi et al. (2004a) and is given by the Equation 4.1

$$I(\omega) = I_o(y)[1 + \gamma cos(2k\delta + \phi(y))] \tag{4.1}$$

where I_o is the amplitude, γ is the fringe visibility, k=$2\pi/\lambda$, δ=piston and $\phi(y)$ is a phase term that depends on where the fringe signal is extracted. Here ω is the position vector on image plane, with (x,y) as rectangular co-ordinates. To obtain the piston error, the intensity pattern of the recorded DFS fringes is fitted with the equation 4.1, considering I_o, γ , and δ are the three variable parameters. Few sample fringe images generated using the simulation are shown in Figure 4.2.

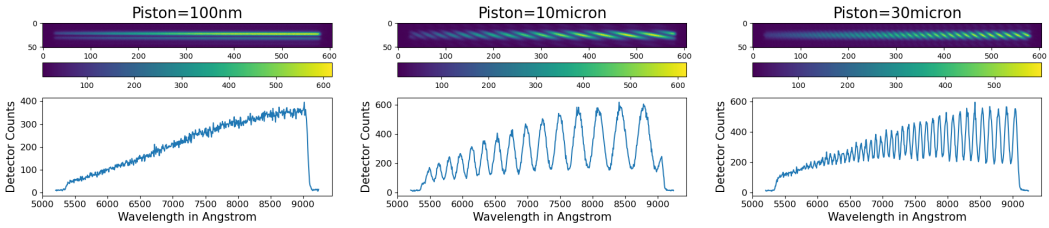

Figure 4.2: Simulated DFS fringe images for star magnitude=10 and exposure time=240sec with piston error of 100nm (left), 10μm (middle) and 30μm(right).

For a moderate value of piston, the DFS fringes have higher visibility, but as the piston error increases, the visibility value reduces. The visibility of the fringes is given as $((I_{max}-I_{min})/(I_{max}+I_{min}))$, where I_{max} and I_{min} are the maximum and minimum fringe intensity values. Thus, due to reduced visibility, the measurement accuracy of DFS reduces with increasing piston error. Similarly, when the piston error reduces to a small fraction of the wavelength, the fringe modulation decreases and we obtain nearly one fringe, for such a case, again the least square fitting accuracy would reduce, thus reducing the piston measurement accuracy. The case of both, small piston and large piston is shown in Figure 4.2. This problem can be resolved to some extent by using the higher wavelength range, i.e moving from visual to NIR-band when coarse phasing is required and using the lower blue spectra when fine phasing is required. These problems and their solutions are discussed in detail in the further sections.

4.3 Simulations on DFS-Based Phasing

As explained in chapter 2, we want to test the feasibility of APS, using our simulations. Hence, in addition to alignment, the APS should be capable of providing precise measurements of very small piston errors (of the order of a few fractions of the wavelength). In our simulations we have attempted to check the feasibility of DFS based segment phasing using the APS.

4.3.1 Simulation Methodology

In the simulation platform, a sampling aperture shape is created for the given inter-segment gap and the piston error δ is applied as phase error = $\pm 2k(\delta/2)$ for each of

the inter-segment regions. As a next step, the atmospheric effect is incorporated on to the aperture by generating the moving phase screen. Further, the monochromatic PSFs are generated for each wavelength by taking the Fourier Transform of this aperture. In order to generate dispersed fringe spectrum, wavelength dependent PSFs are shifted spatially along the dispersion direction by following the grating dispersion law. The Python code developed for DFS simulation is similar to the code used for the alignment and co-focusing simulations. The generation of a monochromatic PSF is same as explained in subsection 2.4.1 as well as in the Figure 2.4. The parameters such as the stellar magnitude, stellar spectral type, sampling aperture diameter, exposure time, Fried parameter, telescope parameters (including the re-imaging optics), grating dispersion and detector specifications are given as input to the simulation code. While generating the dispersed fringe spectrum, effect of chromatic variation of the atmospheric extinction, grating efficiency and the detector QE are also taken into account. Then, all kind of noises such as photon noise, sky background noise, detector readout, PRNU and dark noises are also added into spectral images of DFS. Figure 4.3 shows a DFS image generated using the simulation code for a piston error of 10μm.

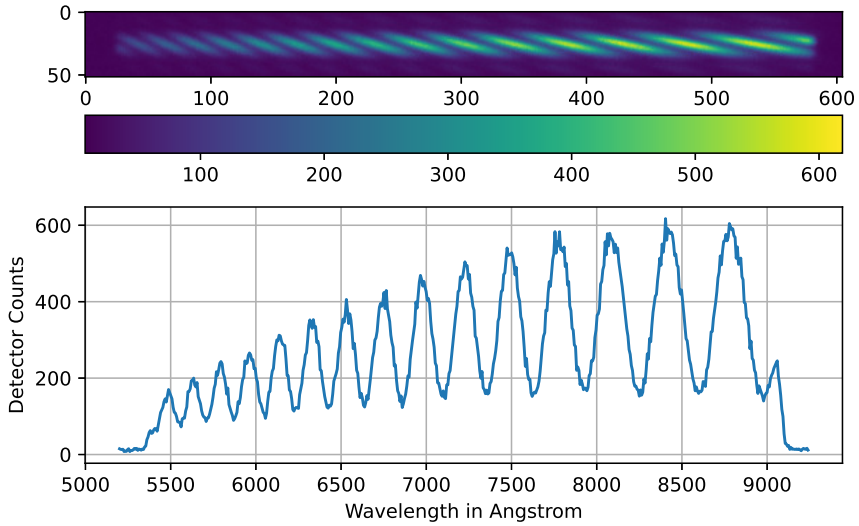

Figure 4.3: Simulated DFS fringe image for star magnitude=10 and exposure time=240sec with piston error of 10μm.

It is important to note that the DFS fringe spectrum is a combination of the source spectrum (which strongly depends on the stellar temperature), atmospheric extinction coefficient, detector QE, grating efficiency and the piston error. Thus, to measure the piston error accurately, the intensity modulations due to all the other

factors need to be nullified. This is achieved by dividing the DFS fringe spectra by a calibration spectra, which is a continuum spectra obtained from the same system under zero piston condition. Practically, to get the zero piston spectra, the sampling aperture is placed at the center of the segment, instead of the inter-segment gap, hence it mimics the zero piston condition (Figure 4.4).

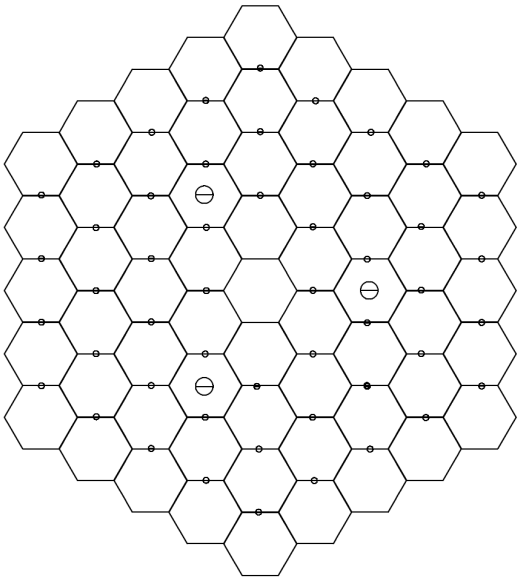

Figure 4.4: Placement of sub-aperture masks for DFS based co-phasing. Aperture diameter of 10cm is used for sampling light from inter-segment edges. For the purpose of calibration, additional three samples are also taken from the center of segment with 30cm aperture diameter.

4.3.2 Effect of Aperture Diameter and Exposure Time on Fringe Visibility

In the DFS scheme, the fringe visibility strongly influences the precision of the piston measurement. The visibility of the fringes is given as $((I_{max} - I_{min})/(I_{max} + I_{min}))$, where I_{max} and I_{min} are the maximum and minimum fringe intensity values. The effect of orientation of the grism with respect to inter-segment region on the visibility is a well studied problem (Shi et al., 2004a,b) and should be taken care of while designing the DFS optics (discussed later in subsection 4.4.4). Whereas, effect of aperture size and exposure time on the visibility is poorly known. In order to boost SNR it is advantageous to use larger aperture. Therefore, we have attempted to explore effect of aperture size on the fringe and its visibility. All the parameters chosen for the phasing related simulations are given in the Table 4.1.

Figure 4.5 shows the variation of fringe visibility against the aperture size. From the figure it is quite apparent that increase in the aperture diameter leads to rapid decrease in the fringe visibility. The fringe visibility which was initially 60% for 10cm aperture and 15^{th} magnitude star, becomes nearly 10% when aperture is enlarged to

Table 4.1: Parameters used in the Monte Carlo Simulations for co-phasing using the DFS technique

Parameter	Value
Wavelength Range	530-900nm
Aperture Diameter	10cm
Camera focal length	75mm
Image scale on detector plane	0.268arc-sec/pixel
Grating groove density	300 lines/mm
Linear Dispersion	6.667A°/pixel
Stellar temperature	3500K (K type star)
Seeing	1arc-sec @ 500nm

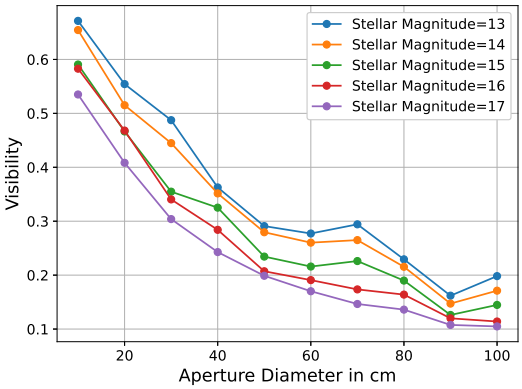

Figure 4.5: Variation of DFS fringe visibility with increasing aperture size, for different stellar magnitudes (Piston=10μm, exposure time=60sec).

almost full segment. In order to understand the cause of reduction in the visibility, we generated monochromatic PSFs for varying aperture size, without atmospheric seeing effect and compared its normalised radial intensity plots (shown in Figure 4.6). It was found that with increasing aperture diameter, the secondary peak of the PSF started diminishing and for largest aperture it almost disappears, leaves only the main peak. Furthermore, from our simulations we found that even in absence of any piston error, for an ideal circular aperture the intensity value of the secondary peak starts reducing as the aperture size increases. Since for DFS the fringe pattern is formed by systematic merging of the primary and secondary peaks for different wavelengths, thus when the aperture size increases the secondary peak intensity is reduced, resulting in to visibility degradation. Additionally, when fine phasing is considered, the secondary peak value plays an important role in piston measurement (subsubsection 4.3.4.2) and hence using a large aperture might degrade the piston measurement accuracy. Thus, the optimum sampling aperture of diameter 10cm can be used as it maximizes the visibility as well as SNR.

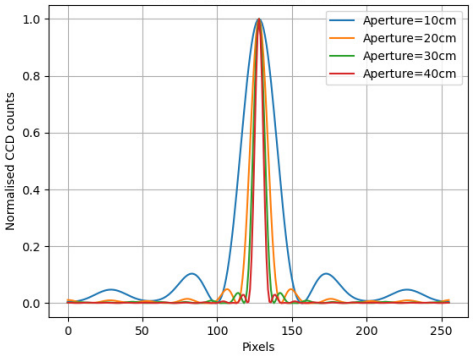

Figure 4.6: Normalised intensity plots for ideal PSFs for varying aperture diameters for zero piston error and wavelength=530nm.

Another important factor that contributes to the visibility is the image motion, thus in the short exposure domain, as the exposure time increases the image motion increases and hence it must reduce the visibility. In the long exposure domain the visibility would remain constant for all exposures. This is confirmed through simulations by measuring the fringe visibility for varying exposure times over the range of 5ms to 100s for a piston error of 10μm and 10cm aperture diameter. For this case we only need to understand the variation of visibility with exposure time, hence we considered a zero magnitude star so that the signal is sufficient even for 5ms exposure time.

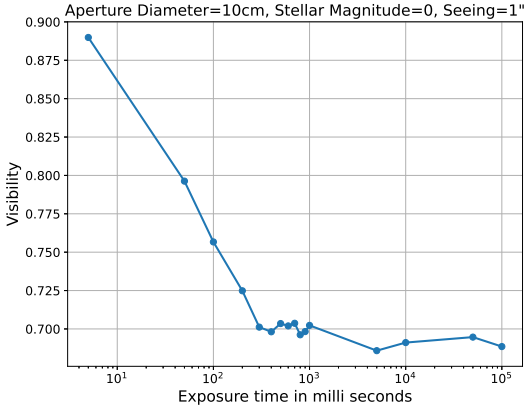

Figure 4.7: Variation of DFS fringe visibility with increasing exposure time (Piston=10μm).

Figure 4.7 shows that within the short exposure domain, the visibility constantly falls from about 0.88 to 0.7 with increasing exposure time and then saturates within the range 0.68 to 0.7 in the long exposure domain, as expected. Thus having a shorter exposure is advantageous but at the same time for the fainter stellar magnitudes in the short exposure domain the signal will be too weak and hence no fringes will be obtained. Thus, for the APS we will have to choose the longer exposures of the order

of a few minutes. From our exploration we found that shorter exposure (few milli-seconds) will have 15-20% better visibility than longer exposure. Though using shorter exposure is advantageous as far as fringe visibility is concerned, however, extracting piston errors using relatively faint star is only possible when long exposure is used.

4.3.3 Effect of Atmospheric Seeing

After confirming upon the basic properties affecting the DFS fringe visibility, we concluded that the aperture size must be kept small (diameter = 10cm for our case) and exposure needs to be longer. Thus we carry out the Monte-Carlo simulations for varying stellar magnitudes to estimate the obtainable value of SNR with the moderate seeing of 1arc-sec. Figure 4.8 shows the plots for DFS fringes along the dispersion direction for the central row with varying stellar magnitude and exposure time. From the intensity plots we see that for higher SNR (SNR values are given in the Table 4.2) the fringe modulation is easily visible but as the SNR reduces for fainter stars, the fringe intensity modulation gets dominated by the noise. For 15^{th} magnitude the fringes are barely distinguishable, whereas, for 16^{th} magnitude star, noise supersedes the signal. The simulated fringe images are for piston=10μm. As the piston error increases, the visibility will further reduce and extraction of piston values will be subjected to larger errors. Thus, to achieve good SNR, the DFS based co-phasing system must work with relatively brighter stars (brighter than 14^{th} magnitude) with an exposure time of 2 to 3 minutes. To estimate the piston measurement accuracy we perform curve fitting on the DFS fringe intensity pattern which is explained in the next section.

Table 4.2: SNR values for DFS fringes along central row and enhanced signal (All DFS simulations done for a piston error of 10μm)

	SNR for Central Row for exposure time of			SNR for Enhanced Signal for exposure time of		
Magnitude	60s	120s	240s	60s	120s	240s
13	37.56	58.66	87.96	111.62	172.92	253.04
14	17.25	27.98	43.08	54.25	87.20	130.32
15	7.38	12.24	19.26	24.08	39.89	60.68
16	3.02	5.09	8.09	10.08	16.98	26.13
17	1.21	2.06	3.29	4.10	6.96	10.78

4.3.4 Extraction of Piston Values From DFS Spectrum

The DFS is considered to be a phasing scheme which usually provides segment piston errors less precisely over a large range with moderate accuracy (Shi et al., 2003; Smith

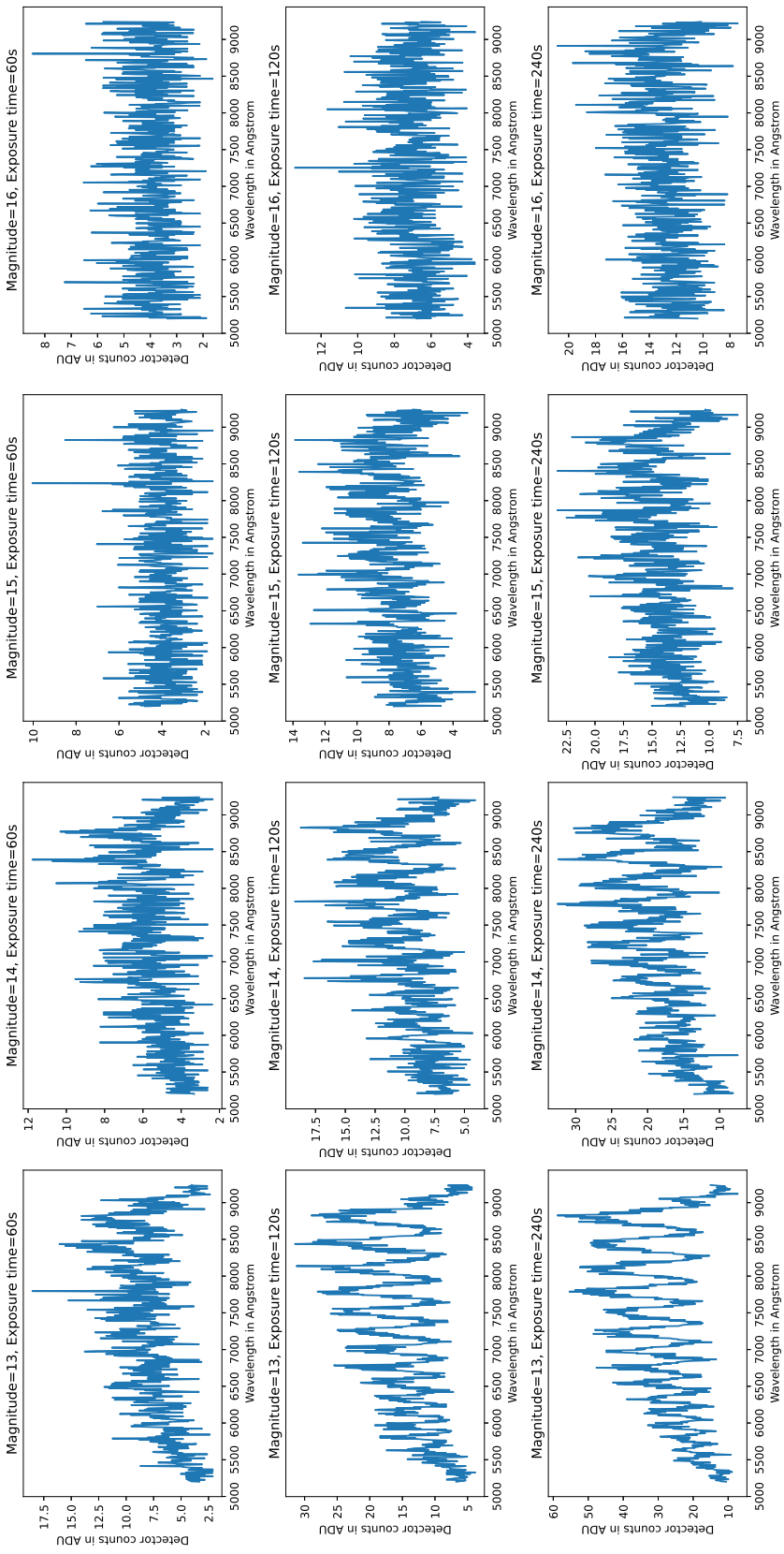

Figure 4.8: DFS fringe plots along dispersion direction for stellar magnitudes of 13 to 16 with exposure time=60sec (top row), 120sec (center row) and 240sec (bottom row).

et al., 2003). However, recent developments have shown that this technique is not only applicable to large piston errors, but it can also be used to measure fine piston errors and provide the accuracy required for diffraction-limited imaging (Zhao and Cao, 2011; Li, Wang, and Rao, 2017). In the subsequent sub-sections we have explored two different methodologies to recover piston errors (δ), one for large ($\delta > \lambda/4$) and another one for small ($\delta < \lambda/4$) errors.

4.3.4.1 Measurement of Medium to Large Piston Errors

The intensity distribution for the DFS fringe spectrum has been derived in Shi et al. (2004a) and is given by the Equation 4.1. For DFS, the resultant intensity pattern on the detector plane is a continuous spectrum modulated by sinusoidal fringes. The frequency of the fringe as well its tilt strongly depends on the piston error. In order to obtain the piston error, the intensity pattern of the recorded DFS fringes is fitted for the Equation 4.1, considering three variables, I_o, γ, δ. The curve fitting is usually carried out on the central row having the highest intensity. Since the DFS fringe spectrum is strongly modulated by wavelength dependent stellar source as well as instrument throughput, hence to remove these spectral features from the modulation due to segment phase error, we first divide the DFS fringe spectra by the normalised spectrum of zero piston error. Unlike the fringe spectrum, the zero piston error spectrum is obtained by sampling the light from the center of a few segments. Table 4.2 gives the SNR values for the central row of the DFS fringes.

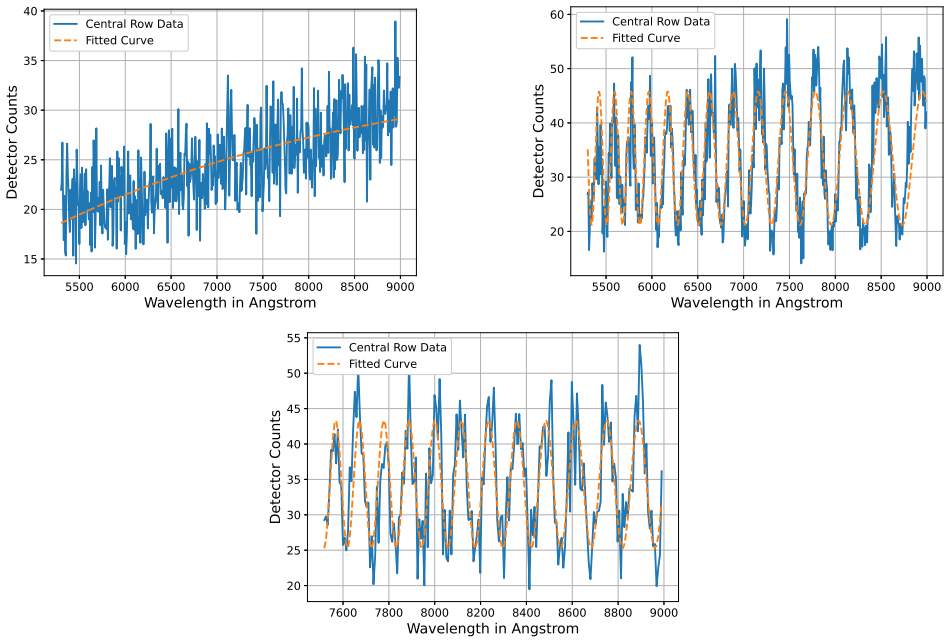

Figure 4.9: DFS fringe intensity plots after curve fitting for central row with piston errors of 100nm (left), 10μm (middle), and 30μm (right). For 30μm piston DFS fringe windowing is used.

Figure 4.9 shows the curve fitting applied on the central row and Table 4.3 gives the extracted piston errors from the simulated DFS spectra. From Table 4.3 it is clear that the achieved phasing accuracy is not acceptable even in case of the 13^{th} magnitude star with 240s exposure. Thus, we apply a signal enhancement technique that can help to improve the DFS fringe intensity signal and hence increase the measurement accuracy. Since the DFS signal not only lies on the central row, but it is spread over multiple rows in the spectrum, hence the signal from multiple rows is added up together to get the enhanced signal, thus improving the SNR. Unlike the usual spectra, multiple rows for the DFS spectra cannot be added directly. The rows are shifted optimally along the dispersion direction such that the intensity peaks match for each row, and then the intensity values are added to get the enhanced signal values.

Table 4.3: Piston extraction from fringes using curve fitting for star with 13^{th} magnitude and 240s exposure time

Applied Piston	Measured Piston Using Central row	Measured Piston using Enhanced Signal	Error for Central row	Error for Enhanced Signal
0.1μm	0.284μm	0.259μm	0.184μm	0.159μm
10μm	8.951 μm	9.375μm	-1.049μm	-0.624μm
30μm	28.128μm	28.417μm	-1.872μm	-1.583μm

Figure 4.10 shows the DFS fringe intensity plots for the enhanced signals for varying stellar magnitudes and exposure time. Similar to the central row, we also use curve fitting for the summed rows having the enhanced signal which is shown in Figure 4.11.

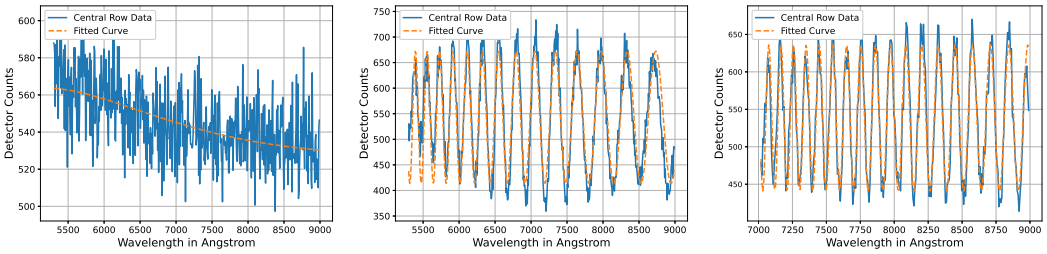

Figure 4.11: DFS fringe intensity plots after curve fitting for enhanced signal with piston errors of 100nm (left), 10μm (middle), and 30μm (right). For 30μm piston DFS fringe windowing is used.

A comparison of the extracted piston values for the central row and the summed rows (Table 4.3), clearly shows that the SNR plays an important role in the curve fitting, the fitting accuracy is higher in case of the enhanced signal as compared to the single central row. It can also be observed that for larger piston errors (30μm in our case), the fitting accuracy degrades due to reduction in the fringe visibility, similar is the case for lower piston errors (piston$< \lambda/4$), where the number of fringes is only

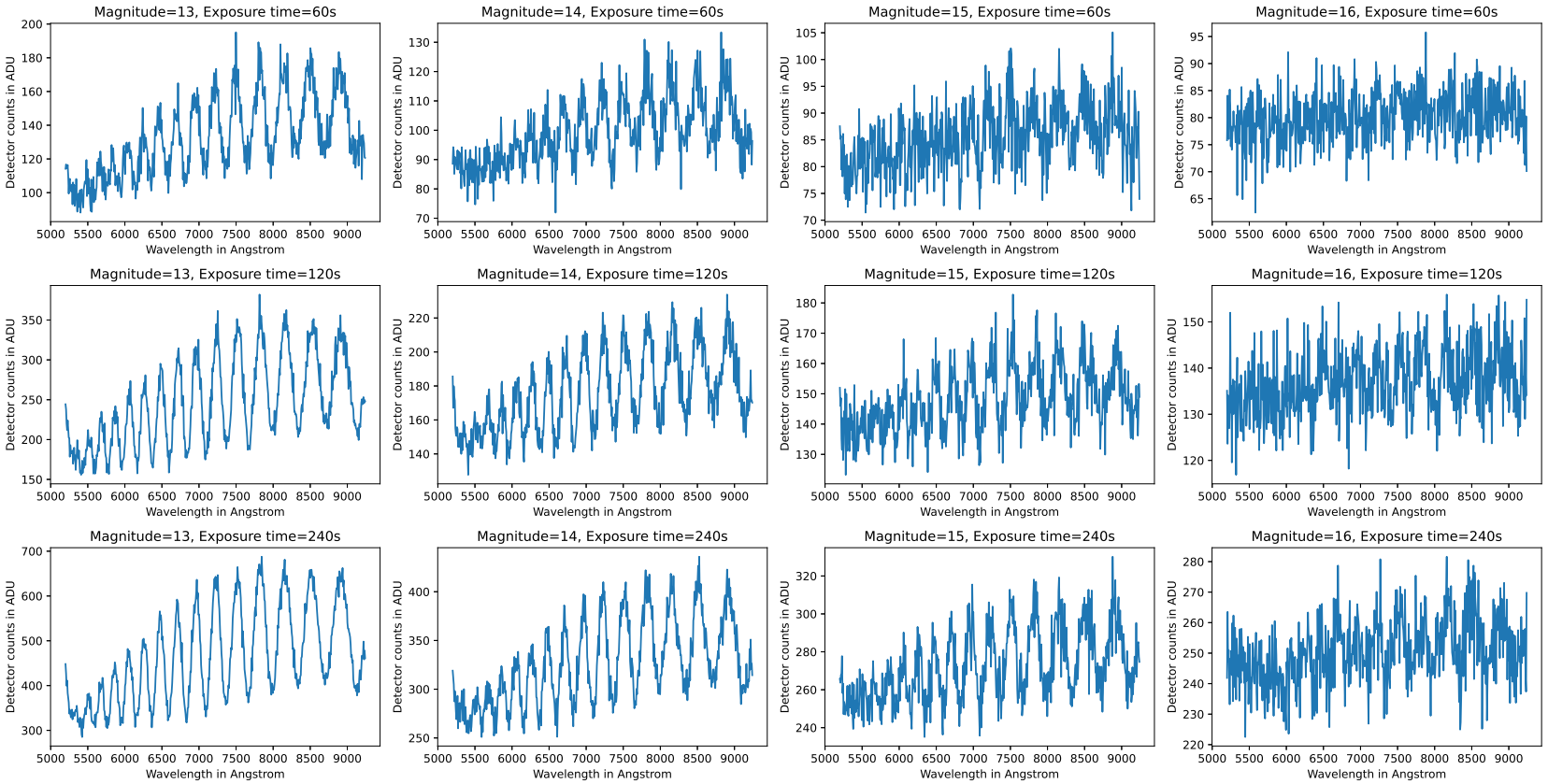

Figure 4.10: DFS fringe plots for enhanced signal for stellar magnitudes of 13 to 16 with exposure time of 60sec (top row), 120sec (middle row) and 240sec (bottom row).

one, and hence the fitting accuracy is very low. To handle the lower piston errors using DFS, different techniques are being developed, one such technique is described in the next subsection.

4.3.4.2 Measurement of Small Piston Errors: the DFA-LSR Technique

In case of lower piston errors, i.e. $\delta < \lambda/4$, only small fraction of the fringe is available and the DFS signal primarily resides in the spectral continuum modulation. As we have discussed earlier, in addition to piston error, the DFS continuum signal is highly affected by wavelength dependent instrumentation throughput variation and hence, by using curve fitting method it is almost impossible to get precise piston measurements, as required for diffraction-limited telescope. To measure small piston errors there are other techniques such as the Main Peak Position (MPP) method (Zhao and Cao, 2011) and the Dispersed Fringe Accumulation based Left Subtract Right (DFA-LSR), which relies on extraction of piston error using the information coded into DFS intensity distribution perpendicular to the dispersion direction (Li, Wang, and Rao, 2017). Since MPP method is highly dependent on calibration and it requires higher SNR (Li, Wang, and Rao, 2017), therefore, we preferred to use the DFA-LSR scheme for our simulation which is best suited for piston errors $< \lambda/4$.

In the DFA-LSR technique, the intensity values are added along the direction perpendicular to the dispersion (Figure 4.12).

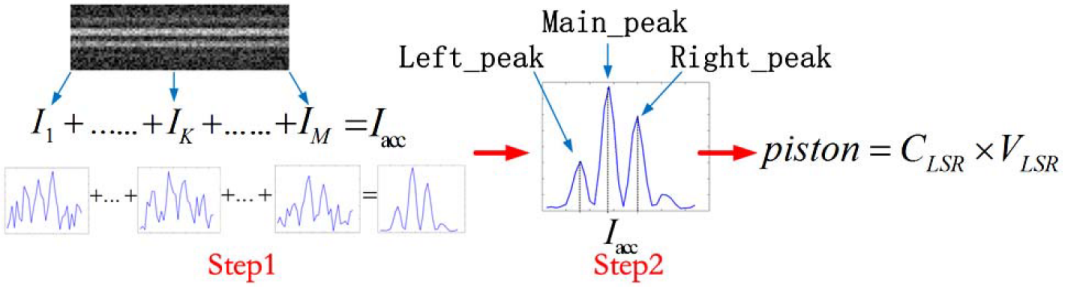

Figure 4.12: Implementation of the DFA-LSR technique. *Credit:* Li, Wang, and Rao (2017).

The obtained intensity profile has three peaks, the ratio of intensity of these three peaks varies with piston errors and this is used for piston measurements. Figure 4.13 shows the intensity profiles for varying piston errors of zero to $\lambda/2$ obtained through simulations.

For zero piston error, the intensity profile has a central peak with two side peaks, as the piston error increases, the central peak value reduces, whereas the secondary peak value starts increasing. At a piston error of $\lambda/4$, two peaks of equal intensity are obtained. Thus, the ratio of these intensity peaks can be related to the piston error. Li, Wang, and Rao (2017) has defined this quantity as the V_{LSR} which can be

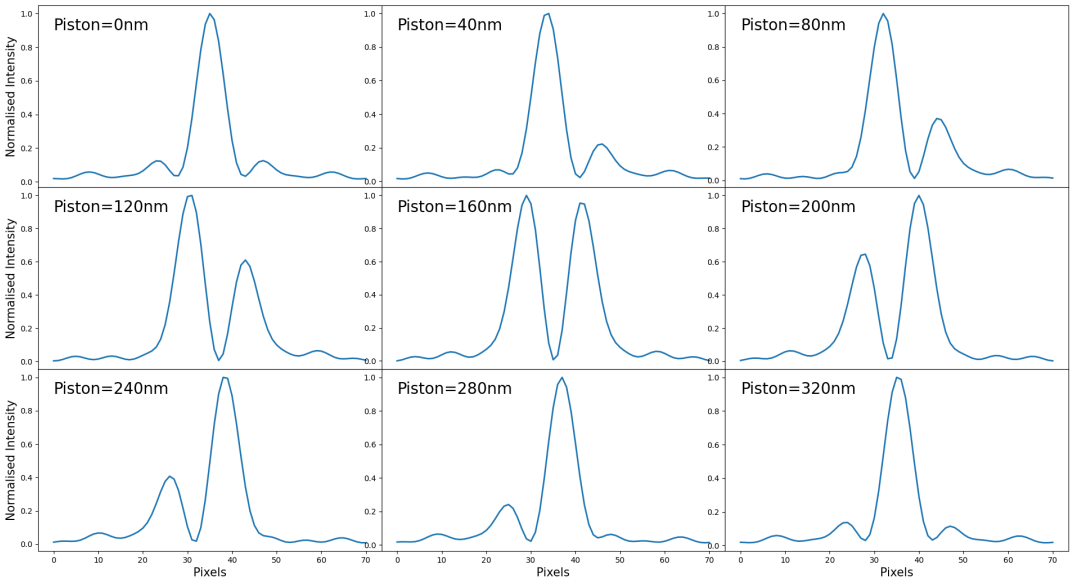

Figure 4.13: Plots showing normalised intensity profiles along Y-axis for different piston errors.

calculated as,

$$V_{LSR} = \begin{cases} \frac{L_p - R_p}{M_p - I_{min}} & L_p > 0, R_p > 0 \\ \frac{L_p - I_{min}}{M_p - I_{min}} & L_p > 0, R_p = 0 \\ \frac{-(R_p - I_{min})}{M_p - I_{min}} & L_p = 0, R_p > 0 \\ 0 & L_p = 0, R_p = 0 \end{cases} \tag{4.2}$$

where I_{min} is the image background of the fringe after accumulating the dispersed fringe. L_p, R_p and M_p are the maximum values of the left peak, right peak, and main peak, respectively. The piston error can be obtained by multiplying the V_{LSR} value with a calibration constant (C) which can be easily obtained through modelling or simulations.

$$Piston(\delta) = CV_{LSR} \tag{4.3}$$

The variation of the peak intensity pattern follows a repeatability due to the cyclic nature of phase at every π phase error, thus, giving a cyclicity of $\lambda/2$ in piston error.

Thus, by applying the DFA-LSR technique, piston errors lesser than $\lambda/4$ can be measured using the DFS. Using our simulations for realistic conditions, we verified the use of DFA-LSR and we found that although, traditionally, the DFS is assumed to be a coarse phasing technique, but by changing the piston extraction methodology from curve fitting (for coarse piston) to DFA-LSR (for fine piston), the DFS technique itself, can be used for coarse as well as fine phasing of segments (Li, Wang, and Rao, 2017; Li and Wang, 2022; Dharmadhikari, Parihar, and Jacob, 2023).

We have used DFA-LSR technique on simulated dispersed fringe spectra subjected

to piston errors of 10-200nm. The variation of the applied and recovered piston error (through simulations) is shown in Figure 4.14 and the values are listed in Table 4.4. The maximum measurement error is approximately 6nm which is well within the phasing requirement of the telescope (section 2.3). Thus, for large piston errors the curve fitting technique is used which acts like a coarse phasing scheme that brings down the piston error to the realm of DFA-LSR technique ($\delta < \lambda/4$). Then, further the fine phasing can be achieved by using the DFA-LSR technique.

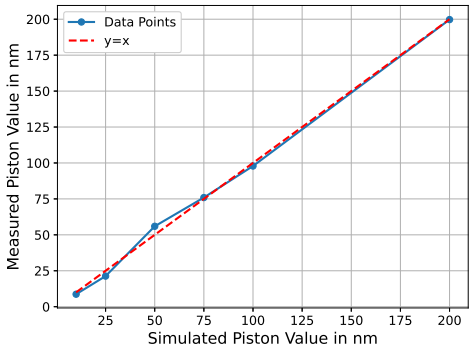

Figure 4.14: Piston measurement using DFA-LSR technique (through simulations).

Table 4.4: Piston extraction from fringes using DFA-LSR for star with 10^{th} magnitude and 240s exposure time

Applied Piston (in nm)	Measured Piston (in nm)	Error (in nm)
10	8.70	-1.30
25	21.29	-3.71
50	55.95	5.95
75	75.93	0.93
100	97.87	-2.13
200	199.74	-0.25

4.3.4.3 A Case Study on the DFS

The measurement error values reported in Table 4.3 are very pessimistic and suggest the attaining the required co-phasing accuracy with the proposed APS will be difficult with faint stars but if we employ the iterative approach for piston measurement with suitable extraction method then measurement accuracy of a few nanometers can be achieved. Here we consider an example case where the initial piston error is δ_0=30μm and it is brought down within a range of 5nm by performing four consecutive measurements.

Figure 4.15 shows the simulated fringe images at each stage of iterative measurement (the simulated fringes are for 13^{th} magnitude star with exposure time of 240

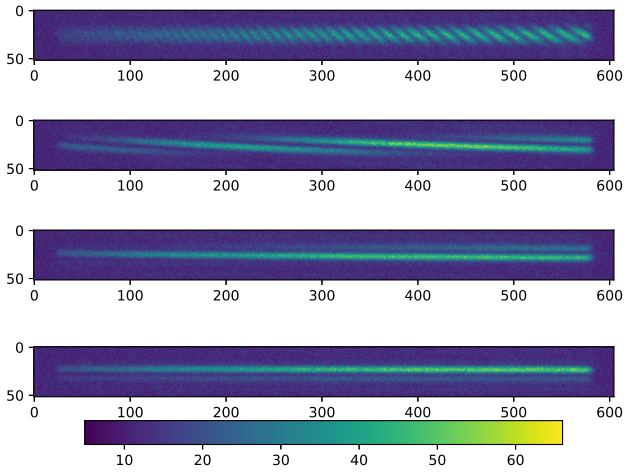

Figure 4.15: Iterative process of piston measurement using DFS: Simulated Fringe images for i) δ_0=30μm ii) δ_1=1.5834μm iii) δ_2=305.9172nm and iv) δ_3=69.4455nm.

seconds and 1arc-sec seeing). For the 30μm piston, we apply the signal enhancement technique as well as DFS fringe windowing (Shi et al., 2003) where, only a part of the DFS spectrum that has higher visibility (700 to 900nm), is used. Then the curve fitting method is used which gives a residual error of δ_1=1.5834μm. Next, we generate the fringe image for 1.58μm piston and apply curve fitting to the central row of the fringe, the obtained measurement error for this stage was δ_2= 305.91nm. Again, we generate the next fringe image for δ_2 and perform curve fitting on the central row. The obtained measurement error is now δ_3=69.44nm falling within $\delta < \lambda/4$ domain. Hence, at this stage DFA-LSR technique mentioned in subsubsection 4.3.4.2 is used. The final measurement error obtained is 5.13nm which is well within the phasing requirements. Figure 4.15 and Figure 4.16 show the simulated fringes as well as intensity plots obtained for all four stages of iteration. From this case study it is clear that DFS alone can handle the coarse as well as fine phasing of the segments by using the iterative measurement process. The values obtained are well within the phasing requirements for diffraction limited imaging, however, in addition to simulation we need to experimentally test and verify it. Thus, extensive laboratory experiments were performed for the DFS based phasing, which are discussed in detail in section 4.4.

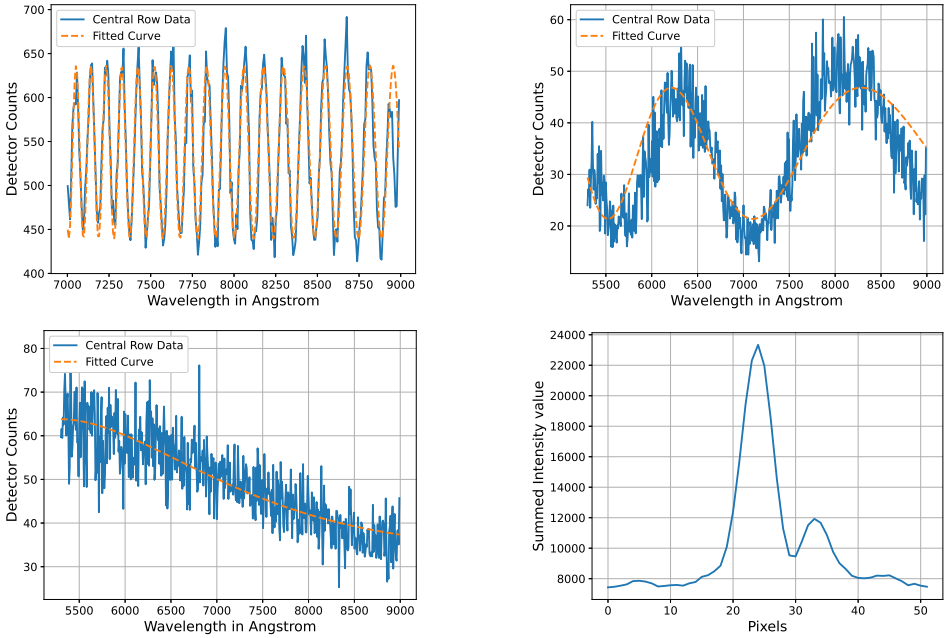

Figure 4.16: Iterative process of piston measurement using DFS: i) Curve fitting for δ_0=30μm (top-left) ii) Curve fitting for δ_1=1.5834μm (top-right) iii) Curve fitting for δ_2=305.9172nm (bottom-left) iv) Summed intensity values for DFA-LSR with δ_0=69.4455nm (bottom-right).

4.4 Laboratory Experiments on DFS

To understand the working of DFS and test its performance under practical situations, we designed a laboratory experiment. As far as the coarse piston measurements using DFS is concerned, it is a well established technique. However, the primary motivation behind conducting the experiment on DFS was to confirm and validate fine phasing using the DFA-LSR scheme as proposed by Li, Wang, and Rao (2017) as discussed in subsubsection 4.3.4.2.

4.4.1 Optical Setup Details

The schematic diagram for the laboratory setup of DFS is given in Figure 4.17, and the actual setup is shown in Figure 4.18. The DFS experiment requires a broad-band light source, hence we use an optical fiber based tungsten source from Thorlabs. A narrow-band filter with 650nm central wavelength and 10nm band width is used with the source. The light from the source is coupled to the optical set up through a 10μm optical fiber, which acts as a point source for the system. This light is then collimated using an achromatic doublet lens (150mm focal length). And then, the collimated beam is directed towards the mirror segments using a beam splitter. The mirror segments are two plane mirrors with $\lambda/8$ surface quality. These mirrors are

mounted on tip-tilt mounts to adjust the x and y-tilt of the mirrors. One of these mirrors is kept stationary and the other one is mounted on a linear actuator which is required for applying the piston error between the two segments. The reflected light from the mirrors, again passes through the beam splitter, which transmits it further to the aperture mask. The aperture mask is a circular opening that cuts down the 50mm collimated beam size to 10mm. This light is then sent through a transmittive grating (300 lines/mm) and then a 400mm focal length camera lens is used to focus it onto the CMOS detector plane.

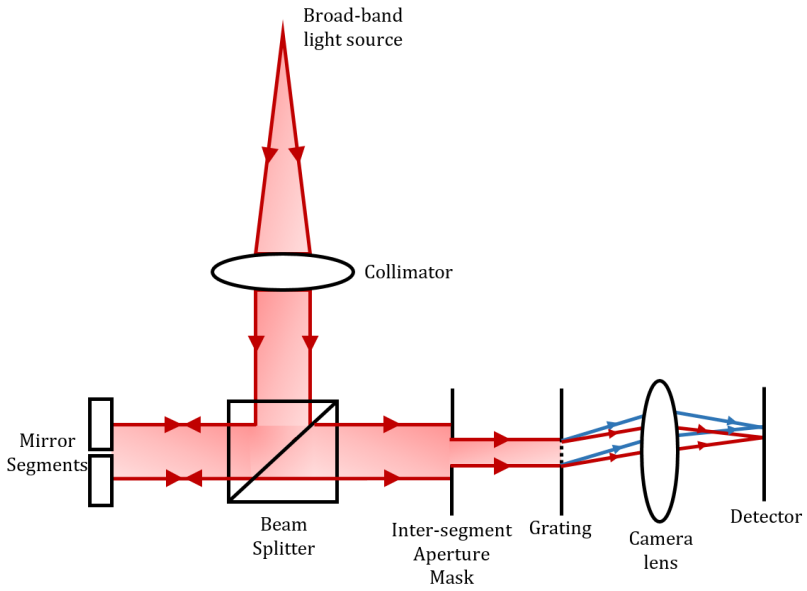

Figure 4.17: Schematic diagram for the laboratory setup for DFS experiment.

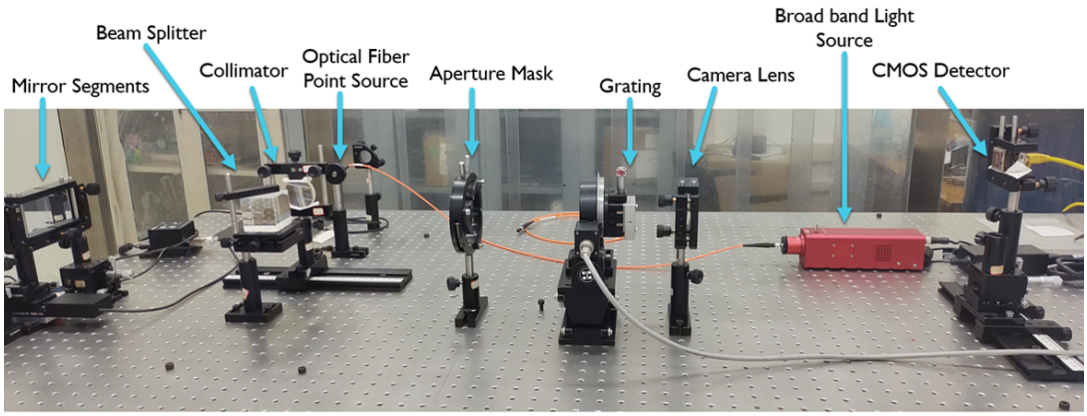

Figure 4.18: Laboratory setup for DFS experiment.

4.4.2 Coarse Phasing Experiment

4.4.2.1 The Setup

For the coarse phasing experiment, one of the mirrors is kept stationary and the other one is mounted on a Thorlabs linear stage, which can provide a minimum piston movement of 1micron. In order to know the actual movement of the mirror, we used a high precision optical encoder with a resolution of 1.2nm. The measured piston values were compared against the encoder values to get accurate results.

4.4.2.2 Procedure

To perform the coarse phasing experiment, we applied 15 steps (with varying step sizes: 1μm, 2μm, 5μm and 10μm) of piston error and at each step 15 DFS images were captured using a large format CMOS camera. For each set of data, we also captured the source spectra by blocking the light from one of the mirror segments. This source spectrum, is then used for the fringe calibration (Figure 4.19).

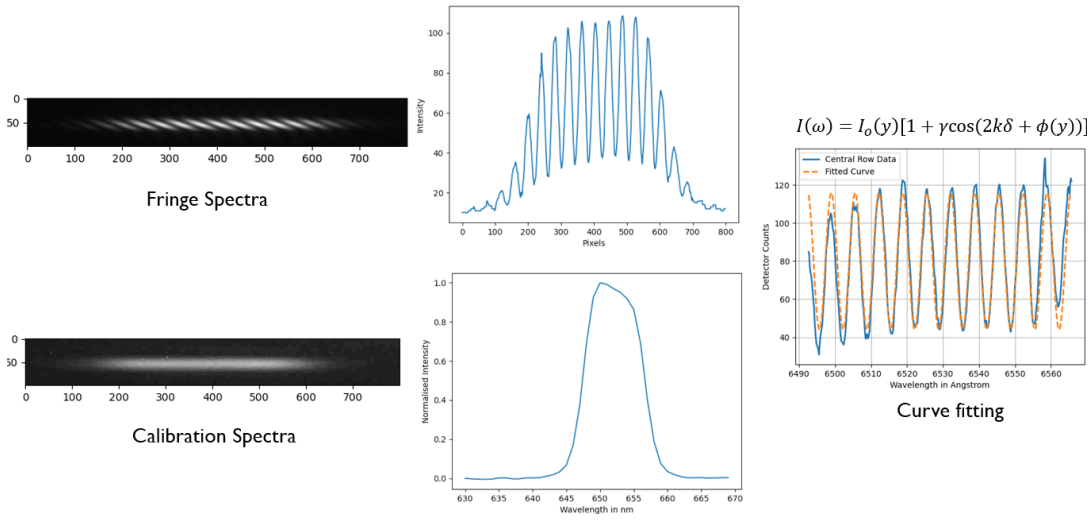

Figure 4.19: DFS calibration process: The fringe images (left), corresponding intensity plots (middle) and processed fringe intensity plot on which curve fitting is applied (right).

The captured fringe image is divided by the normalized calibration spectrum to remove the effects of the source intensity profile. The calibration spectra is also important for the wavelength calibration of the DFS fringes as it affects the curve fitting. For our experiment, the method adopted for the wavelength calibration is a very crude one, where, the starting and ending points of the intensity profile from calibration spectra are matched with that obtained from the theoretically calculated instrument response spectra. Although the method is very crude, but it is found to work quite well for DFS based phasing, as it does not require very precise wavelength

calibration. However, the wavelength calibration accuracy can be improved by using a source with multiple emission lines. Once the calibration process is completed, then the central row of the DFS fringes is extracted and the Equation 4.1 is fitted on this data to get the piston value.

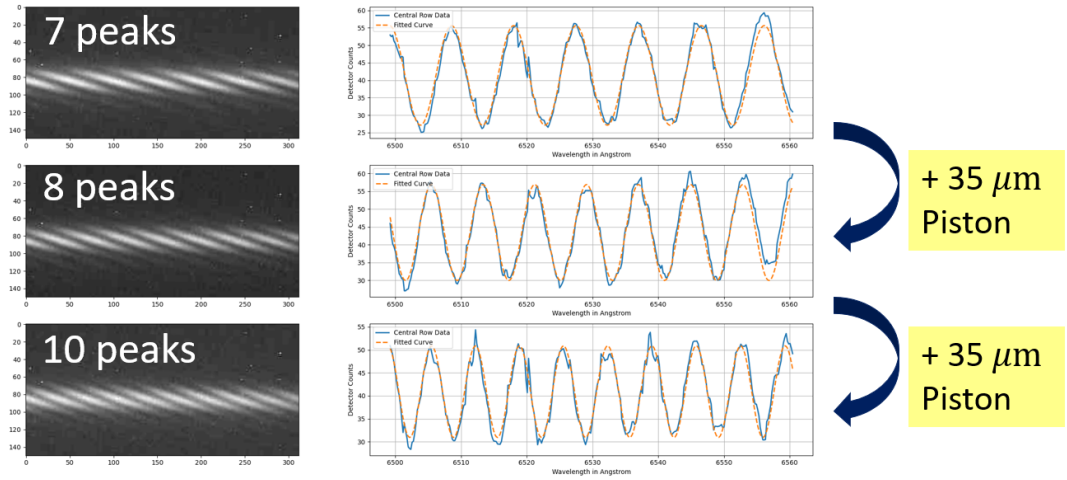

Figure 4.20: Illustration of basic principle of DFS: DFS fringe images for increasing piston errors captured in the laboratory experiment.

4.4.2.3 Coarse Phasing Results

To ensure its repeatability, the coarse phasing experiment was repeated multiple times with different step sizes (1μm, 2μm, 5μm and 10μm). For each case the differential piston measurements are compared against the applied piston values. The applied piston values are obtained from a high precision optical encoder mounted on the mirror set up. The measured values are plotted against the applied piston values and a straight line is fitted onto the data to get the slope and RMS error. Figure 4.20 shows the real fringe images and the intensity plots for increasing piston errors, where the increasing frequency of the DFS fringe is clearly visible, this illustrates the basic principle of DFS.

The plots for applied vs measured piston values for step sizes of 1μm, 2μm and 5μm are shown in Figure 4.21. On the applied vs measured piston values we apply a straight line fit to get the slope and RMS error. The obtained values for different step sizes are tabulated in Table 4.5.

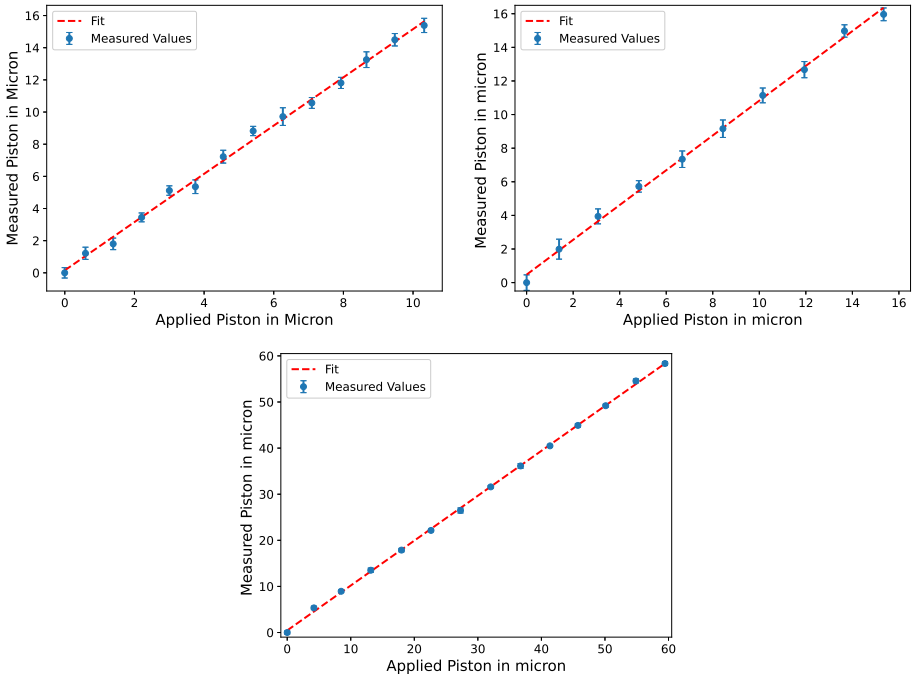

Figure 4.21: Plots for applied vs measured piston values for step size of 1μm (top-left), 2μm (top-right) and 5μm (bottom).

Table 4.5: Experimental results for the coarse phasing using DFS

Step Size	Fit Slope	RMS Error (in nm)
1 μm	1.021	386.252
2 μm	0.952	314.795
5 μm	0.935	591.375
10 μm	0.991	1209.089

From the coarse phasing experiment we have achieved a piston measurement accuracy of about 300nm ($< \lambda/2$). The DFS based phasing experiments conducted on sky for the Keck telescopes obtained a better accuracy of 142nm (Shi et al., 2004a) and DCATT experiment achieved an accuracy of 50nm with DFS (Shi et al., 2000). Similar results have been obtained by several other groups for the DFS based coarse phasing (Zhang et al., 2011; Kopon et al., 2016). The coarse phasing experiments have been performed earlier by several groups and our experimental findings match well with theirs. However, main motivation of this work is to perform the DFS-based fine phasing experiment to validate the DFA-LSR technique, which is discussed in the next sub-section.

4.4.3 Fine Phasing Experiment

Conventionally, DFS is considered to be a coarse phasing technique, that can measure piston errors $> \lambda/4$ but our simulations have shown that DFS can also be used for fine phasing by using the DFA-LSR technique. Thus, we performed the DFS based fine phasing experiment to validate this technique.

4.4.3.1 The Setup

To conduct the fine phasing experiment, we need to apply piston errors of the order of a few nano-meters, which requires a nano-positioning actuator. Due to unavailability of a nano-actuator in our laboratory, we developed a Voice Coil Motor (VCM) based nano-actuator in house at IIA. A VCM based, high precision, custom designed actuator was developed earlier by Deshmukh et al. (2018). Hence, we decided to design and fabricate a smaller version of the same actuator, so that it can be used in the fine phasing experiment for DFS. The basic principle of the actuator design and its electronic control is based on the design mentioned in Deshmukh et al. (2018). Figure 4.23 shows the VCM based nano-actuator, specially designed for the fine phasing experiment, on which the mirror segment is mounted. To know the precise movement of the actuator, a high precision optical encoder was mounted on the nano-actuator.

4.4.3.2 Stability Tests of Nano-actuator

An initial round of fine phasing experiment was conducted with the laboratory setup, but the measured piston values were found to be inconsistent with the applied values. Hence, we conducted extensive stability tests on the nano-actuator and the mirror system to understand and eliminate the source of error. For this test, images are captured when the actuator is stationary. A total of 15 sets of images are captured. The stability test is conducted for two conditions:

1. With nano-actuator in off condition
2. With nano-actuator powered on in closed loop

Since the optical encoder is highly sensitive to temperature changes, hence for each of the experiment sets, the temperature variations are also recorded. For each of the above cases, the DFS fringe images are used to get the piston value and these values are then compared against the encoder values. Ideally, the optically measured values (using DFS) must match with the encoder values for both the conditions.

Multiple sets of data were recorded for each case and it was found that when the nano-actuator is powered off, the encoder values and the optically measured DFS piston values both show nearly a same drift of about 55nm (Figure 4.22 top panel). Whereas, when the nano-actuator is on and works in closed loop, in that case we

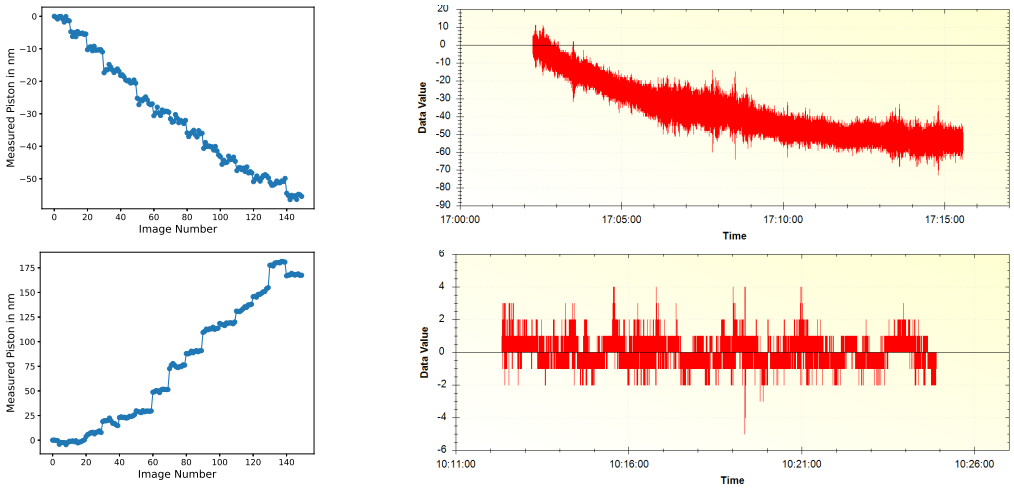

Figure 4.22: Plots for measured piston values using DFS (left) and encoder values (right) for nano-actuator working in off condition (top panel) and nano-actuator working in closed loop condition (bottom panel).

see that the actuator constantly maintains its position within ±5nm but the optically measured piston values shows a large drift of about 150nm (Figure 4.22 bottom panel).

From this experiment we concluded that the large difference in the encoder vs the optically measured values might be arising due to the placement of the optical encoder. The encoder was not placed on the mirror, instead it was close to the actuator because the encoder data is also fed as input to the close loop electronic control system for the actuator. The placement of the encoder can be seen in the Figure 4.23.

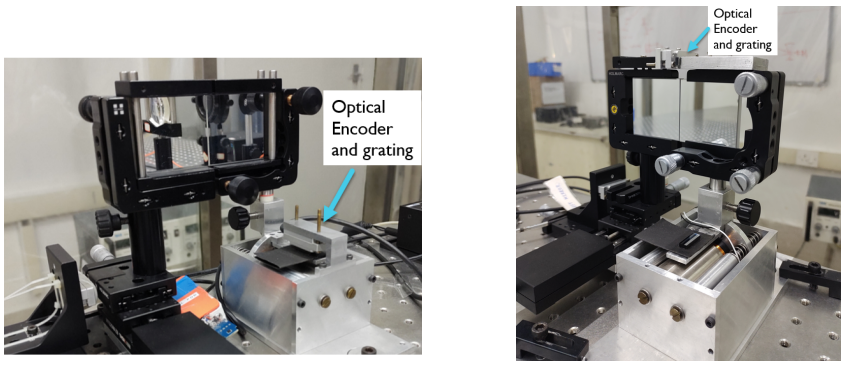

Figure 4.23: Segmented mirrors mounted on nano-actuator with optical encoder placed on the nano-actuator (left) and modified placement of optical encoder on mirror mounts (right).

Therefore, the mirror mounts were modified such that the encoder and grating could be mounted as close to the mirrors as possible (Figure 4.23), so that the actual relative movement of the mirrors could be recorded by the encoder. Using the upgraded set up, we found that the stability problem was resolved and system started

working as expected. Hence, the fine phasing experiment was then performed, the details of which are discussed in the subsequent sections.

4.4.3.3 Procedure

For the fine phasing experiment, the experimental procedure adopted is same as that for the coarse phasing case, however, the piston extraction method is different. After the image processing is completed, the DFA-LSR technique is used to extract the piston errors. Unlike for the coarse phasing case (where the intensity along x direction is used for curve fitting), the DFA-LSR scheme uses the DFS fringe intensity patterns along the interference direction (y-axis in our case). Therefore, to generate the intensity profile along y direction, intensity values along x direction are summed up together. This gives an intensity profile along the y direction with three peaks (Figure 4.12). The quantity V_{LSR} (Equation 4.2) can be obtained from the intensity profiles and further corresponding piston error can be calculated by multiplying the V_{LSR} value with the calibration constant.

4.4.3.4 Calculation of Calibration Constant for the Experiment

As per Equation 4.3 the piston error is obtained by multiplying the V_{LSR} value with a calibration constant. Therefore, to get accurate piston measurements, it is important to know the calibration constant correctly. Thus, we used our Python-based simulation to quantify the calibration constant. Considering all the experimental parameters, the DFS fringe images were simulated for piston errors of 0 to $\lambda/2$. The obtained intensity profiles are shown in Figure 4.13. For each of the fringe images, the V_{LSR} values were calculated and they were plotted against the piston value to get a plot as shown in Figure 4.24. A straight line curve is fitted to the V_{LSR} values

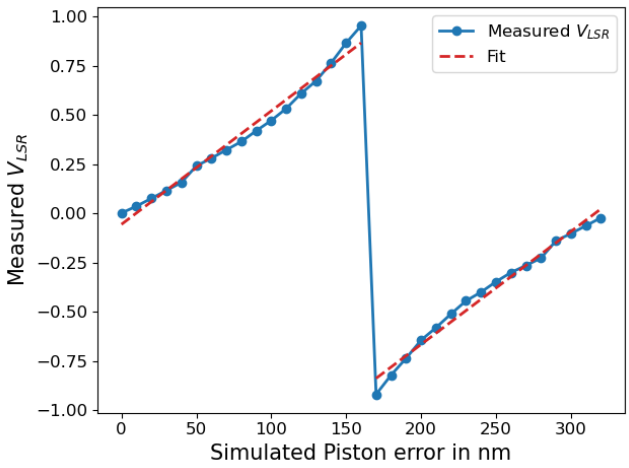

Figure 4.24: Calculation of DFA-LSR calibration constant using simulations.

and the calibration constant is obtained as the inverse of the slope value. From this process we found that the calibration constant value for our experimental setup will be 181.036. This value has been later used on the experimental data to obtain the measured piston values for the fine phasing experiment.

4.4.3.5 Fine Phasing Results

The fine phasing experiment was performed multiple times to ensure the repeatability of the experiment. In each case, a step size of 20nm was applied and 30 images were captured at each step. The DFA-LSR technique was applied on the captured image data (Figure 4.25) to get the measured piston values. The variation of intensity peaks for the experimental data is shown in Figure 4.26. It can be clearly seen that the experimental intensity profiles match quiet well with the simulated intensity profiles. For each of the images the V_{LSR} value is calculated and then the calibration constant is used to get the corresponding piston errors (Figure 4.27). Figure 4.27 shows the $\lambda/4$ cyclicity of the V_{LSR} value, hence the measurement range of the DFA-LSR technique is limited to $\pm\lambda/4$ piston errors. A straight line curve is fitted on each of the data sets to get the slope as well as the RMS error (Figure 4.28). The average slope for all the experiments is found to be 1.08 and the RMS error is about 2.52nm.

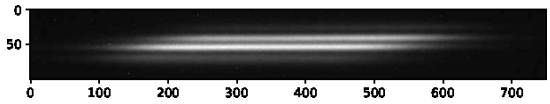

Figure 4.25: Captured fringe image of the fine phasing experiment.

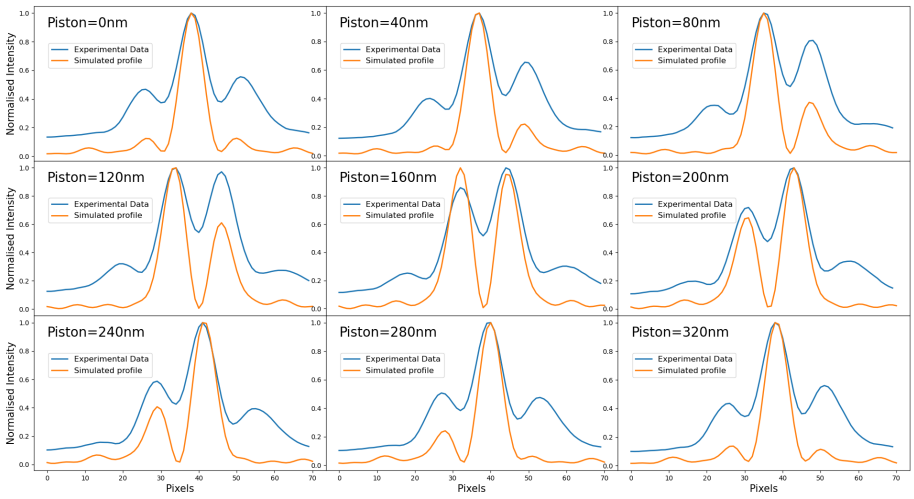

Figure 4.26: The variation of intensity plots with piston errors. The plots obtained form experimental data are over plotted with the simulated intensity profiles.

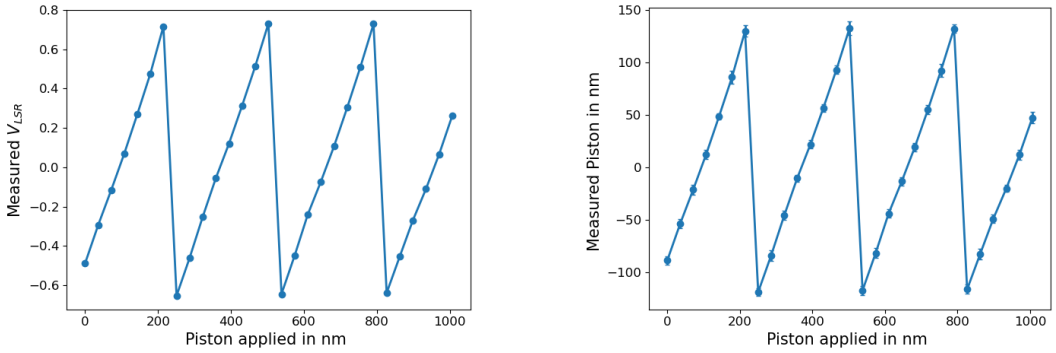

Figure 4.27: Variation of V_{LSR} with applied piston (top) and variation of measured vs applied piston value (bottom).

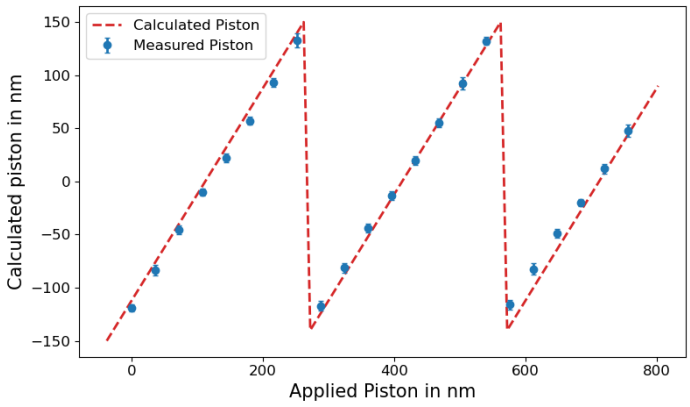

Figure 4.28: Variation of applied vs measured piston errors.

Another experiment that used the DFA-LSR technique was performed by Li and Wang (2022), where they achieved a piston measurement accuracy of 5nm using the DFA-LSR technique. The measurement accuracy achieved in our experiment not only agrees with previous study but it is better. From this experimental study, we confirm that indeed DFA-LSR scheme can be used for fine phasing of any segmented mirror telescope. From the simulations and experimentation we have shown that by using suitable piston extraction methods, DFS alone, can be used for coarse as well as fine phasing of segmented mirrors.

4.4.4 Handling Visibility Problem Using Dove Prism

The DFS samples light from the inter-segment regions and then a grating is used to get the dispersed spectra. However, in case of segmented mirrors, the segments are normally hexagonal in shape, hence there are three possibilities of orientation between

the inter-segment gap and the grating direction. These are zero degrees, $+60^o$ and -60^o. The zero degree is the case when the inter-segment gap is perfectly aligned with the grating grooves, this is the ideal alignment for the DFS system, where the visibility is found to be maximum. However, as the orientation angle between the inter-segment gap and the grating changes the visibility of the DFS fringes reduces. Since the visibility of DFS fringes affects the curve fitting process, hence, it can lead to reduced measurement accuracy. Therefore, to understand the severity of the orientation problem and its effect on the measurement accuracy, we have performed a laboratory experiment.

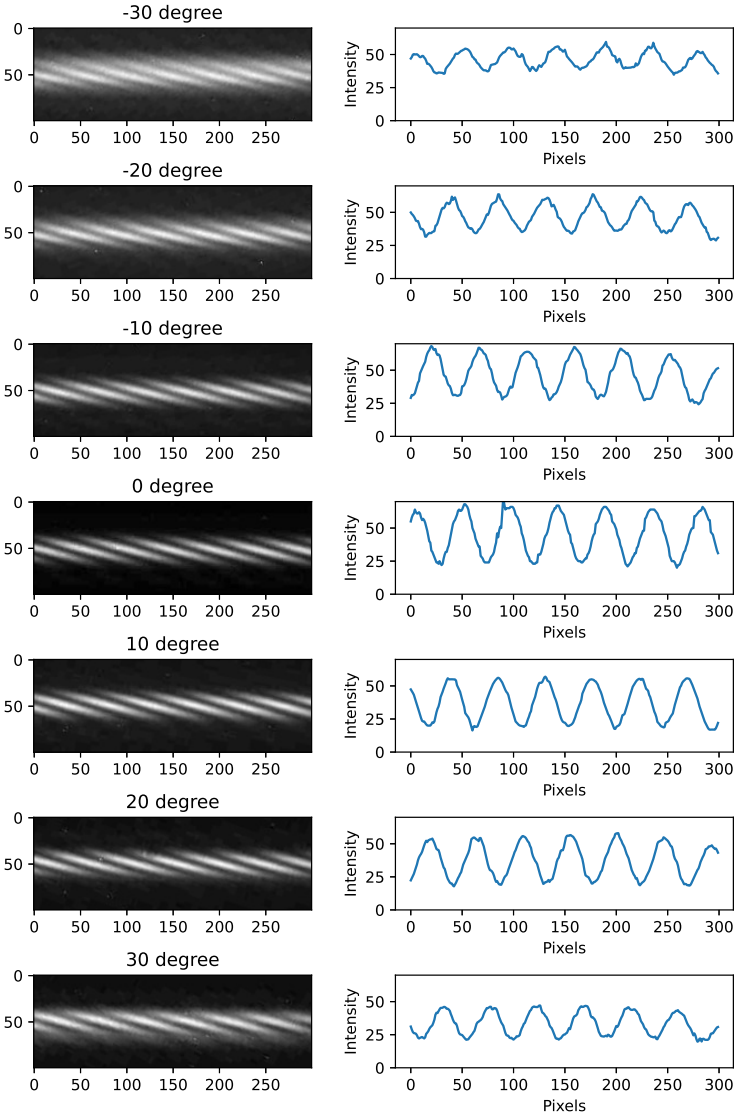

Figure 4.29: DFS fringe images and their intensity plots for different angle of orientations of the grating.

To perform the experiment the grating was mounted on a motorised rotational stage from Holmarc. Thus, the grating orientation with respect to the inter-segment gap could be changed as per our requirement. To test how visibility changes with the orientation, a fringe image was captured for different angular orientations of the grating. Figure 4.29 shows the captured fringe images and the intensity plots along the central row of the fringes for grating orientation of 0^o, $\pm 10^o$, $\pm 20^o$ and $\pm 30^o$. The degradation in the fringe visibility can be clearly seen in the fringe images as well as the intensity plots. This visibility degradation issue can be solved by introducing a Dove prism before the grating. The basic property of dove prism is that when the incident beam is parallel to its base, then the output image is inverted. Thus, by rotating the Dove prism the image can also be rotated. We use this property of the Dove prism to counteract the effect of the grating orientation angle. The Dove prism is introduced in our DFS set up just before the grating so that the collimated beam sampled from the inter-segment region first goes through the Dove prism. By rotating the Dove prism, we can align the light coming from the inter-segment gap with the grating and hence the visibility can be maintained for different grating orientations. Figure 4.30 shows the DFS experimental setup and the positioning of the Dove prism for the Visibility correction experiment.

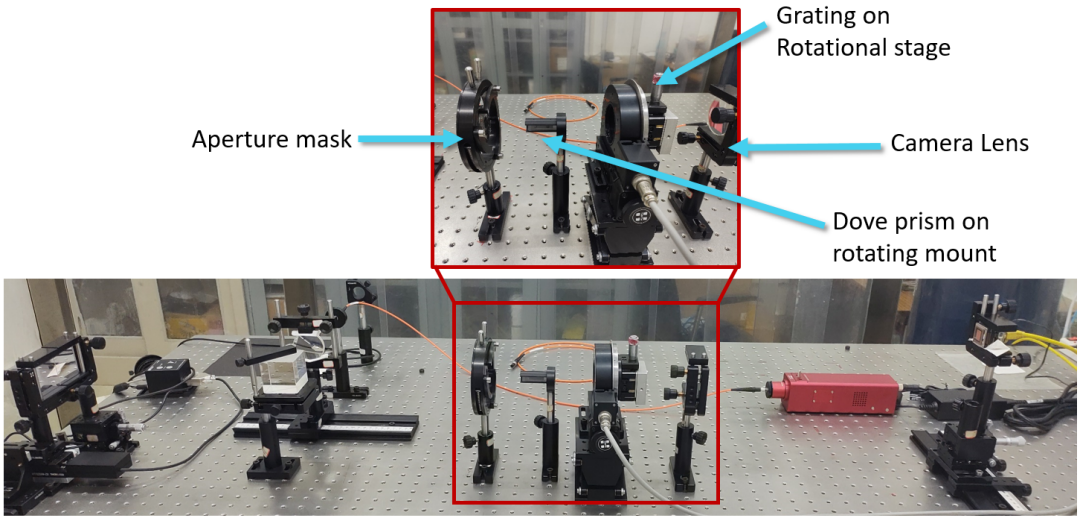

Figure 4.30: DFS experimental set-up for visibility correction experiment using Dove prism.

Figure 4.31 shows the central row intensity plots for fringes captured at different grating orientations, with and without dove prism. Table 4.6 shows the variation of measured visibility values with the grating angle, with and without using the dove prism. From the Figure 4.31 we can see that for 60^o grating orientation the fringe modulation is completely vanished and piston measurement would be impossible in this case. However after introducing the dove prism, the fringe modulation is restored

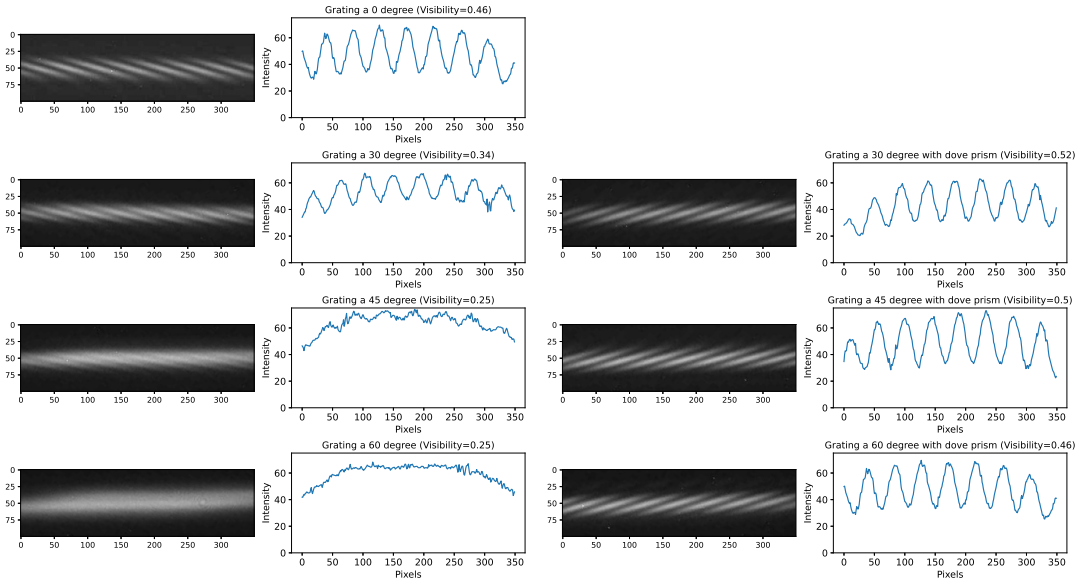

Figure 4.31: DFS fringe images and their intensity plots for different angles of orientation of the grating without dove prism (left) and with dove prism (right).

and the improvement in fringe visibility is clearly noticeable. Therefore, from our experiments, we have shown that the visibility degradation problem, that arises due to a mismatch between inter segment gap and grating orientation, can be resolved by introducing a simple Dove prism in the DFS setup.

Table 4.6: Visibility values for various grating orientations

Grating Orientation	Visibility without Dove Prism	Visibility with Dove Prism
0^o	0.58	-
30^o	0.34	0.52
45^o	0.25	0.5
60^o	0.24	0.46

4.5 Summary

The diffraction-limited imaging performance is only possible for a segmented mirror telescope when its mirror segments are precisely phased. And hence co-phasing of segmented mirror telescopes is one of the most critical tasks. Through extensive simulations, we have explored the possibility of using DFS for coarse as well as fine phasing. Further, from the simulation studies on the DFS, we found that while im-

plementing practically, the DFS scheme can be subjected to three major problems. Firstly, the large capture range of DFS is affected by its visibility. Secondly, fine phasing can not be achieved by the conventional curve fitting method of piston extraction. The third issue is linked to the hexagonal shape of the mirror segments, which causes visibility reduction when piston measurements of multiple inter-segment regions are carried out simultaneously. The first problem has been studied very well by several groups (Shi et al., 2003; Zhang and Xian, 2020). In this work, we have mainly focused on the second and third problems. Through extensive simulations and laboratory experimentation, we have shown that the same DFS device can be used to measure small piston errors, for fine phasing. A phasing accuracy of 2-3nm has been achieved in our laboratory experiments. Further, to address the problem with the simultaneous piston measurements, we proposed to use a Dove prism as a beam rotator. We performed the laboratory experiments for this and found that the Dove prism can be used successfully to counteract the effect of the $\pm 60^o$ orientation angles, thus improving the fringe visibility for all three orientations. Through extensive simulations and experimentation, we have demonstrated that the DFS can be used for both coarse and fine phasing of any segmented mirror telescope.

Chapter 5
Optical Transfer Function Based Alignment and Phasing

Simulation and experimental study of the OTF based alignment and phasing of segmented mirrors
Radhika Dharmadhikari and Padmakar Parihar **Proc. SPIE 13094, Ground-based and Airborne Telescopes X, 1309427 (28 August 2024)**

5.1 Introduction

The Optical Transfer Function (OTF) is defined as the Fourier transform of the PSF, which consists of two components: the magnitude, called the Modulation transfer function (MTF), and the phase, called the Phase Transfer Function (PTF). The MTF is related to the contrast of the PSF, and the PTF gives the wavefront phase. Hence, the OTF contains information about the wavefront error introduced in terms of the tip-tilt and piston errors. The use of OTF for measuring segment tip-tilt and phase errors was introduced in Baron et al. (2008) and Guerri et al. (2010), where the phase component of the OTF (i.e., PTF) was used to measure piston errors with high accuracy of nearly 10nm. However, this technique suffers from phase wrapping problems and could measure piston errors $< \lambda/4$ and hence is found to be suitable only for fine phasing. Later on, Jiang and Zhao (2016) and Simar, Stockman, and Surdej (2015) found that the secondary peak of the MTF is strongly correlated with the piston error. Hence, this property can be utilized to measure the segment piston errors with an extended measurement range of up to 200microns. As a part of the current thesis work, through simulations and experimentation, we have explored the possibility of using the OTF for measuring both coarse and fine piston errors present in any segmented mirror telescope.

5.2 OTF for Segment Alignment and Phasing

The optical layout of the OTF-based phasing scheme is shown in the Figure 5.1. The light from any point source, such as a star, is re-imaged after the telescope focal plane using a collimator and a camera lens. A band pass filter and a mask are placed in the collimated beam. The sampled light is focused on the detector plane to get the PSF. In order to measure the segment tip-tilt and piston errors using the OTF, the light must be sampled from a pair of sub-aperture masks as shown in the Figure 5.1. Without any steering optics such as prism/lenslet, OTF allows simultaneous measurement of piston errors from a large number of segments (Zhang et al., 2023).

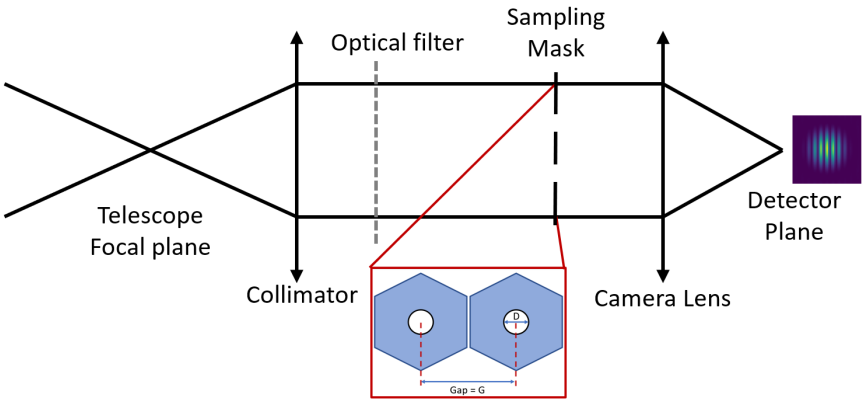

Figure 5.1: Optical layout for OTF based tip-tilt and piston measurements. Inset: the sampling aperture mask.

The observed PSF pattern on the detector plane (u,v) is given by Equation 5.1. The complete derivation for Equation 5.1 can be found in Jiang and Zhao (2016).

$$PSF(u,v,\lambda) = \frac{D^2 {J_1}^2(\pi D\sqrt{u^2+v^2})}{u^2+v^2}\left[1+cos\left(\frac{2\pi}{\lambda}p - 2\pi uG\right)\right] \tag{5.1}$$

where, p is the piston error, D is the sampling aperture diameter, G is the gap between the sub-apertures, J_1 is the first order Bessel function, u=x/(λf) and v=y/(λf), f is the focal length of the camera lens. Equation 5.1 contains two terms, the first term corresponds to the diffraction effect, and the second term is the interference term. From Equation 5.1 we see that the interference term is affected by the piston value p. In the next step, this PSF is Fourier transformed to get the OTF. The OTF is a complex quantity that consists of real and imaginary parts. The magnitude of the OTF forms the MTF, whereas the phase term forms the PTF. Both of these terms contain information about the tip-tilt and piston errors of the mirror segments.

5.2.1 OTF for Tip-Tilt Measurements

The PTF gives the wavefront phase map; hence, it is highly sensitive to the segment tip-tilt errors, so, in addition to fine phasing, it can also be used to co-align the mirror segments. By deriving the gradient/slope of the phase map, one can very precisely measure segment tip-tilt errors. A detailed description of the tip-tilt measurements using this method can be found in Baron et al. (2008); Guerri et al. (2010) and Yu and Zhao (2018). However, in this thesis, we have briefly explored the measurement of tip-tilt errors using the PTF. The tip-tilt simulations are carried out without considering noises or external effects. Figure 5.2 shows a plot of the applied and recovered segment tilt error when segments are free from piston error. From this simulation, we find that the OTF can also be very effectively used to derive the tip-tilt errors of the segments; however, in this thesis, we focus on the use of OTF for phasing of mirror segments. In the subsection 5.3.4, we explore the presence of the crosstalk between the tip-tilt and piston errors.

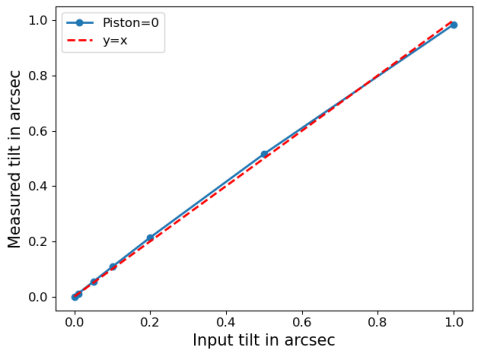

Figure 5.2: Measurement of tip-tilt errors using PTF under zero piston error condition.

5.2.2 OTF for Phasing

Using OTF for phasing a segmented mirror telescope was first introduced by Baron et al. (2008), where the phase part of the OTF (PTF) was utilized for piston measurements. It was noticed that for very small values of piston errors, the MTF almost remained invariant, whereas PTF showed a strong dependence on the piston error. However, this method of piston measurement using PTF suffered from a phase wrapping problem, due to which the measurement range was limited to $\pm\lambda/4$. Thus, the PTF can be used only for fine phasing of mirror segments. However, for large piston errors, instead of using the PTF, if the MTF is considered, then the effect of piston errors becomes measurable (Equation 5.1). In the case of large piston errors, as the piston error increases, the PSF starts blurring, or the contrast of the PSF reduces. The MTF is also called the contrast transfer function, which means that the MTF

value represents the contrast of the PSF. Thus, blurring of the PSF in the presence of piston errors directly affects the MTF. If we consider two segment sub-apertures having piston errors, then the simulated PSF for this case is shown in Figure 5.3. The blurring of PSF is clearly seen with increasing piston errors. The magnitude of the Fourier transform of the PSF is the MTF. In this case, the obtained MTF has a central peak and two secondary peaks (bottom panel in Figure 5.3).

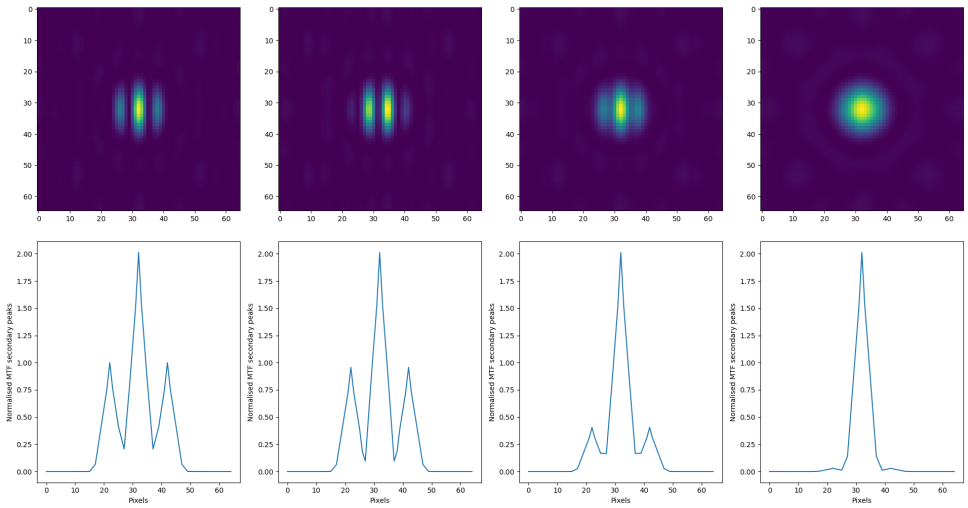

Figure 5.3: Simulated PSF for piston errors of 0, 10, 50 and 100micron respectively (top panel). Normalised intensity plots for corresponding MTF, showing the diminishing secondary peak (bottom panel).

The intensity of the central main peak remains unaffected by the piston errors. However, the intensity of the secondary peaks reduces as the piston error increases. The intensity of the secondary peak is maximum for zero piston error, therefore, it is used to normalise the MTF. The variation of the normalised secondary peak intensity value against piston error is shown in Figure 5.4. The normalised secondary peak value reduces with increasing piston error and it follows a Gaussian trend. The measurement range of this technique is limited to the coherence length of the filter ($\lambda^2/2\Delta\lambda$). For piston errors larger than the coherence length, the PSF becomes completely blurred, and the normalised secondary peak value of the MTF becomes close to zero. This sets the upper limit for the piston error measurement range. The variation of the normalised secondary peak value with piston error follows a Gaussian function. Hence, the peak value can be translated to the corresponding piston error by fitting a Gaussian function. By using different filters with varying coherence lengths, the piston measurement range and accuracy can be varied. Figure 5.4 shows the variation of MTF secondary peak values with piston errors for three different filters with a central wavelength of 632nm and band widths of 2nm, 40nm, and 316nm. For each of these cases, the coherence length (and hence the measurement range) is

100μm, 5μm, and 632nm, respectively. For the coarse phasing, using a narrow band-pass filter (2nm band width) the MTF-based piston measurement works well, giving a measurement accuracy in the order of <1μm. In principle, by making use of a very wide band-pass filter, the MTF itself can be used to measure small piston errors ($< \lambda$); however, fortunately, the PTF shows a strong dependence on the segment piston error and hence, can provide very precise measurement of small phase errors (Baron et al., 2008; Guerri et al., 2010). So, by using magnitude and phase parts of the same OTF, one can precisely measure piston errors, starting from a few nanometers to hundreds of microns. The use of PTF for fine phasing has been described in detail in the subsection 5.3.3.

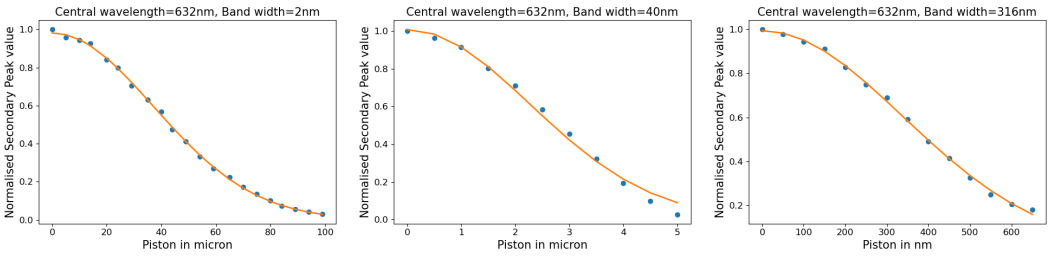

Figure 5.4: Plots showing variation of normalised secondary peak value of the MTF against piston errors, under ideal condition for different band-pass filters. Filter band width=2nm with measurement range=100micron (left), filter band width=40nm with measurement range=5micron (middle) and filter band width=316nm with measurement range=632nm (right).

5.3 Simulations on OTF-Based Phasing for India's Large Segmented Mirror Telescope

Theoretically, the OTF scheme can be used for segment phasing for the coarse and fine piston error measurements; however, under practical conditions, several external factors may affect the measurement accuracy. Therefore, it is important to understand the effects of external parameters on the performance of the OTF-based phasing. We have developed a Python-based simulation code that includes all the significant external disturbances, such as the stellar magnitude, atmospheric turbulence and extinction, sky and moon background, transmittivity losses, and detector noises. The simulation code can generate the PSF for any given telescope + APS. We used this code to understand the effects of exposure time, atmospheric seeing, sampling aperture size, and the aperture gap on the OTF-based phasing results. For ideal conditions, the effects of sampling aperture diameter and the aperture gap have been discussed in detail in Zhang et al. (2023) and Zhao and Zeng (2017). The simulation methodology and the results obtained are discussed in the subsequent subsections.

5.3.1 Simulation Methodology

To test the feasibility of the OTF-based phasing scheme, we use our Python code, which generates realistic images of a telescope by incorporating all possible contributors, like light loss due to atmospheric extinction and telescope + instrument optics, smearing of the image due to atmospheric seeing, noises getting injected in the image/spectrum from all different sources. The working of the code is the same as that described in subsection 2.4.1. The parameters, such as the star magnitude, exposure time, the sampling aperture diameter, telescope focal length, telescope F-number, reimaging optics focal lengths, sky brightness magnitude, object-moon separation, phase of the moon, the atmospheric Fried parameter (r_o), detector specifications (pixel size, quantum efficiency, dark current, detector temperature, read out noise) are given as input to the system. Using these parameters, we first generate a synthetic stellar image. The image blur due to the dynamic atmosphere (seeing effect) is introduced by generating random and moving phase screen using the Python package AOtools(Townson et al., 2019). Finally, we introduce various noises, such as photon noise, sky background noise, and detector noises. Since the atmospheric phase screen and all other sources of noise are random in nature, hence to get realistic values, we used Monte Carlo Simulations. The simulated PSF images are then Fourier transformed to get the OTF, which has two components, the MTF and PTF that are used for further analysis. For each round of simulation, two sets of PSFs are generated, one with the piston error and another one with zero piston error, which will be used for MTF secondary peak normalisation. For the simulations, we have considered a 10m class R-C design-based segmented telescope (section 2.2). The optical parameters used for the APS are listed in Table 5.1.

5.3.2 Simulations on Coarse Phasing

Using our Python-based simulations, we studied the effects of various external parameters on coarse phasing, which involves the use of MTF for piston measurements. We have studied the effects of stellar magnitude, exposure time, sampling aperture size, and atmospheric seeing on the MTF-based piston measurements.

5.3.2.1 Effect of Stellar Magnitude

The most important parameter that decides the SNR is the magnitude of the observed star; hence, we start our simulations with varying stellar magnitudes for aperture size of 10cm and gap of 40cm. The obtained results are shown in Figure 5.5. For fainter stars, the deviation from the Gaussian curve is observed to be higher; hence, measurement errors will be significant. Thus, from these simulations, we conclude that OTF measurements can only be made for high SNR case. The results shown here are for an exposure time of 100ms; hence, by increasing the exposure time, fainter stars

Table 5.1: Parameters used in OTF related simulations

Parameter	Value
APS parameters:	
Collimator focal length	600mm
Camera focal length	127.63mm
Sub-aperture sampling diameter (D)	10cm
Sub-aperture Gap (G)	40cm
Filter Band width	2nm
Filter center wavelength	632.8nm
Atmospheric Parameters:	
Seeing	1arc-sec @ 500nm
Wind speed	9.5m/s
Sky Brightness	21.28 magnitude/$arc-sec^2$
Object-moon separation	45^o
Moon Phase	Full Moon (ψ= 0^o)
Lens Transmittivity	75% per lens
(assuming achromatic doublet lens)	
Detector:	
Pixel size	$15.0\mu m$
Quantum Efficiency	85%
Temperature	243.0K
Dark Noise	0.03 e^- per pixel/second
Read out noise	2.3 e^- per pixel
Detector gain	2

can also provide the desired accuracy. The effect of exposure time is discussed in the next subsection.

5.3.2.2 Effect of Exposure Time

The exposure time is another important parameter that strongly influences the SNR and, hence, can affect the accuracy of the piston measurement. We use centroiding to find the MTF secondary peaks; hence, the variation in exposure time can affect the centroiding accuracy, especially under low SNR conditions. Thus, we used our simulations to study the variation of MTF peak values with exposure time. The variation of the normalised MTF secondary peak values with exposure time for varying piston errors is shown in Figure 5.5. From the results, it is observed that the normalised peak intensity does not show much change with exposure time for a bright star; however, in the case of fainter stars of 7^{th} and higher magnitudes, we see that increasing the exposure time gives the peak values close to the ideal Gaussian curve. Due to high computational time, we restricted our simulations to 100ms exposure. However, from

our long exposure simulations for DFS section 4.3, we know that, by increasing the exposure time, even fainter stars of 11-12th magnitude can be used for MTF-based phasing.

5.3.2.3 Effect of Aperture Size

In the previous subsections, we found that a higher SNR gives better measurement accuracy. Hence, another way of increasing the SNR is to increase the sampling aperture diameter. However, the sampling aperture diameter and the gap must be chosen carefully such that the MTF secondary peaks do not merge with the center peak (Zhang et al., 2023). For the MTF secondary peaks to be separated, the minimum gap must be 2 times the aperture diameter; hence, with the segment size of 1.44 m, the largest possible aperture diameter is 60cm with a 120cm gap. We generate the simulation results for this case and compare them with the aperture diameter of 10cm. Figure 5.5 shows the comparison of these two cases for different stellar magnitudes.

Again, we see that for bright stars, there is no effect of changing the aperture diameter; however, for faint stars, we see that increasing the aperture diameter gives larger deviations from the ideal Gaussian and hence would give larger measurement errors; this effect can be attributed to the atmospheric seeing which is considered to be 1arc-sec (10cm approximately) in this case, hence for the larger diameter 60cm and gap of 120cm, the two apertures effectively experience two completely incoherent parts of the atmosphere. Hence, the PSF is completely distorted, thus giving large deviations from the ideal Gaussian curve. The next section describes the results for different seeing conditions.

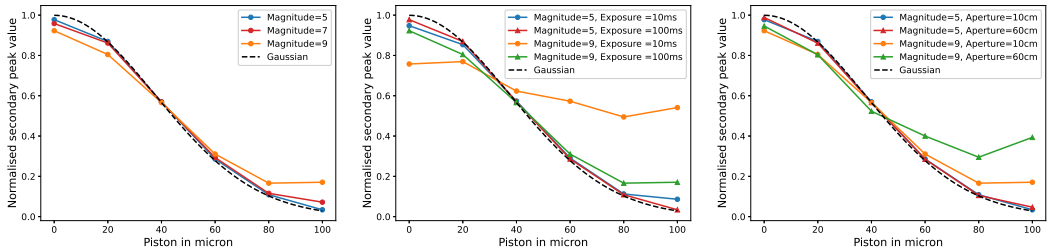

Figure 5.5: Variation of normalised secondary peak value of the MTF against piston error for different stellar magnitude (left), exposure time (middle) and aperture size (right).

5.3.2.4 Effect of Atmospheric Seeing

The atmospheric seeing is characterised by the Fried parameter (r_o). For the seeing limited case, the PSF obtained has a FWHM of $0.98\lambda/r_o$. Another important effect that atmospheric seeing introduces is the image motion. Thus, when starlight is used for piston measurements using the OTF-based phasing, the effects of atmospheric

seeing would blur the PSF. To understand the effect of seeing on the OTF-based measurements, we simulated the PSFs for two different seeing conditions of 0.5arc-sec and 1arc-sec. Figure 5.6 shows the variation of normalised MTF secondary peak value with the seeing for aperture size of 60cm. Here, we see that for all three stellar magnitudes, the peaks closely follow the Gaussian curve when the seeing is good (0.5arc-sec), whereas for a seeing of 1arc-sec, we start finding the large deviations, especially for the fainter magnitude.

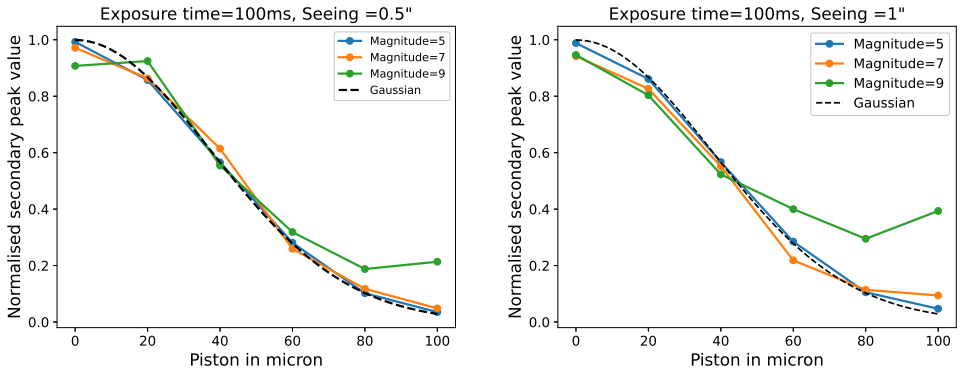

Figure 5.6: Variation of normalised secondary peak value of the MTF with piston error for atmospheric seeing of 0.5arc-sec and 1arc-sec for different stellar magnitudes.

5.3.3 Simulations on Fine Phasing

From the results shown in all of the above sub-sections, it is clear that the MTF can provide accurate measurements for the piston under coarse piston regime (piston error$> \lambda$). Further, by selecting a suitable broad-band filter, with a small coherence length, the measurement accuracy of MTF can be improved to a few fractions of the wavelength. A piston measurement accuracy of this order is good enough to phase the segments of a telescope aiming to deliver diffraction-limited imaging in the near-infrared wavelength. However, for optical wavelength, a phasing accuracy of less than 10nm is desired for diffraction-limited imaging, hence the PTF can be used. The PTF is found to be much more sensitive, and hence it is a better diagnostic tool to measure piston errors falling under fine phasing regime ($< \pm\lambda/4$) (Baron et al., 2008; Guerri et al., 2010). In the wavefront phase map, the presence of the piston error can be directly visualised as a phase offset. Figure 5.7 shows the wavefront phase map obtained using the PTF for a piston error of 120 nm, which consists of the central map and two side maps; the two side maps correspond to the phase error between the two segment sub-apertures. The wavefront phase can be directly converted to piston error by multiplying with the factor ($\lambda/4\pi$). However, this technique shows a cyclicity of $\lambda/4$ due to phase wrapping and hence can only measure piston errors smaller than $\lambda/4$. Figure 5.7 shows the variation of measured piston values with input

piston values for ideal simulations. The $\lambda/4$ cyclic behaviour can be clearly seen from the plot in Figure 5.7.

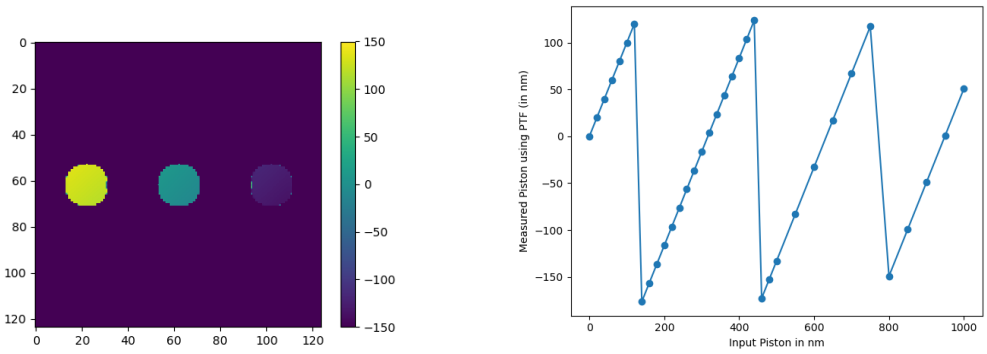

Figure 5.7: The simulated wavefront phase map (PTF) for piston error of 120nm (left). Plot showing variation of derived piston values against applied piston values (right).

The simulations for the ideal case show that it is possible to use the PTF for segment phase measurements; however, it is important to understand the working of this technique under realistic conditions. Hence, we used our realistic simulations to generate the PSFs for very small piston errors in the fine phasing domain, and then used the PTF to measure the piston errors. We considered two cases, one for a high SNR with a stellar magnitude of 5 and the second for a lower SNR with a stellar magnitude of 11. For both of these cases, the exposure time was varied from the short exposure range to the long exposure case, i.e., from 5ms to 500ms, and the results were compared for both cases. For each of these cases, we considered three different seeing conditions of 0.5arc-sec, 1arc-sec, and 1.5arc-sec. The obtained results are shown in Figure 5.8.

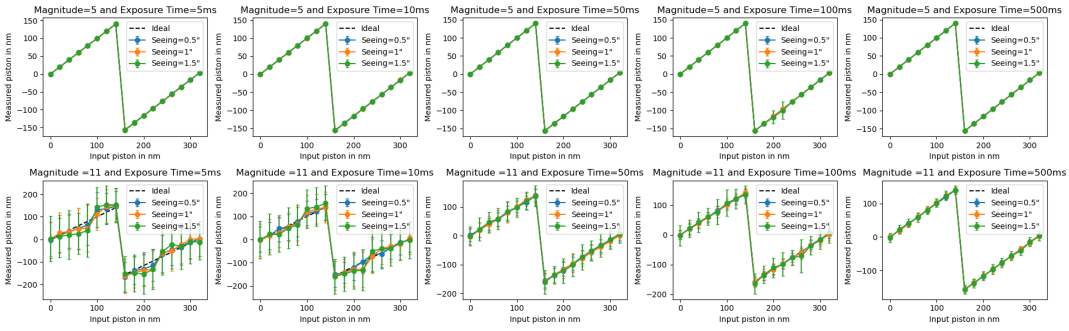

Figure 5.8: Plot showing variation of derived piston values (using PTF) against input piston values for the stellar magnitude of 5 (top row) and 11 (bottom row) for varying exposure time and atmospheric seeing.

Figure 5.8 shows that for higher SNR, i.e. 5^{th} magnitude star, the effects of seeing and exposure time are negligible on the measurements. However, for lower SNR

case with 11^{th} magnitude star, the measurement errors are initially very high with short exposure. As expected, the measurement errors are found to be reducing with increasing exposure time. For the longest exposure time of 500ms, we see that the measurement accuracy of the order of 10-20nm can be achieved with 11^{th} magnitude star. Whereas a 5^{th} magnitude star, even with short exposure time, we can bring down the piston measurement error to just a few nanometer. Hence, it would be advantageous to use a bright star with high SNR for fine phasing case to achieve better phasing accuracy.

5.3.4 Simulations on Cross Talk Between Tip-Tilt and Piston Measurements

Since OTF is highly sensitive to the tip-tilt errors present on the segment, it is important to understand how the piston measurements would get affected when segments are subjected to tip-tilt errors of different orders. Therefore, to explore this cross-talk, we have carried out simulations for the ideal case. The parameters used in these simulations are the same as mentioned in Table 5.1, but the ideal situation, without any external factors/noises, is considered here. We first start with the coarse phasing case, where the MTF secondary peak value is used for piston measurements. In addition to the piston error, tilt errors varying from zero to 1arc-sec have been introduced on both segments and the normalised MTF peak value is derived for each case. Figure 5.9 shows the variation of MTF secondary peak values with piston error in the presence of different values of segment tilt errors. With increasing tilt values, we see slight deviations from the ideal Gaussian curve. The same exercise is repeated for tip, and we see that the tip and tilt errors both have nearly the same effect on piston measurements.

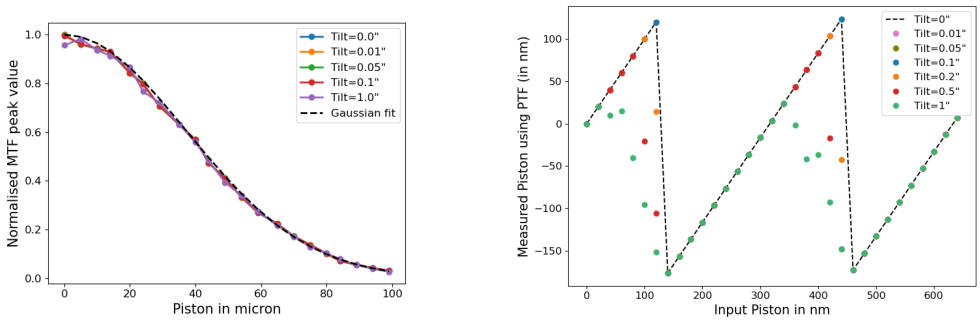

Figure 5.9: Variation of the normalised secondary MTF peak values against piston error in presence of different tilt errors (left) and effect of tilt errors on piston measurements derived using the PTF for the fine phasing case (right).

As done for the coarse piston measurements, we have also repeated the simulations for fine phasing, where the PTF is used for the piston measurement. Figure 5.9

shows the variation of measured piston value for different tilt errors. In this case, the diameter of the integration area on the phase map is considered to be 5 pixels. However, we have also found that by reducing the diameter of the integration area, the effect of tilt error on the piston measurements can be significantly reduced. From Figure 5.9 it is seen that the piston measurements remain unaffected by tilt errors up to a value of 0.1arc-sec; beyond this, the measured piston values start deviating from the ideal value. Similar to the coarse phasing case, here also we note that the tip and tilt errors both have nearly identical effects on piston measurements.

5.4 Laboratory Experiments on OTF-Based Phasing

We have carried out extensive simulations for the OTF-based phasing and found that for the coarse phasing condition, the MTF can be used for piston measurements. This technique remains insensitive to external parameters under high SNR conditions. Similarly, for fine phasing case, the PTF is expected to give the desired measurement accuracy of a few nano-meters. Therefore, we have also attempted to conduct laboratory experimentation on the OTF-based phasing technique so that the findings of the simulations can be practically verified.

5.4.1 Laboratory Setup

The laboratory setup for the OTF-based experiment is shown in Figure 5.10. As shown in Figure 5.4, the measurement range of MTF-based piston measurement depends on the coherence length of the light source. Hence, we use two types of sources as per the requirement: (i)Thorlabs broad-band tungsten light source with different filters and (ii) a diode LASER (635 nm) with a spatial filter to create a point source. The light from the point source goes through a 150mm focal length collimator, which gives a collimated beam of 50mm diameter. Using a beam splitter, the collimated beam is reflected towards two plane mirror segments. These mirrors are mounted on a high-precision linear actuator from Thorlabs. The custom-built nano-actuator allows very precise movement of the mirror segment along the optical axis, thus helping to introduce any desired piston error of the order of a few nanometers. The reflected light from the mirror segments returns to the beam splitter and is transmitted further towards a second beam splitter that splits the beam into two perpendicular arms. The light reflected from the beam splitter 2 is used for performing the OTF-based phasing (shown with a blue dotted line in Figure 5.10) while the transmitted light is used for the DFS (section 4.4) based phasing measurements (shown with a red dotted line in Figure 5.10). In the OTF arm, we have the aperture mask after the beam splitter 2. The aperture mask used here samples light from both the segments through two circular regions of 6mm diameter each. This light is then focused onto the detector plane of the CMOS camera using a 750mm focal length camera lens. The

recorded image of the PSF is then Fourier transformed to get the OTF, and then the MTF/ PTF can be used to derive the piston values. The specification of the optical setup used in the experiment is given in the Table 5.2. We conducted the laboratory experiments for three different filters, thus covering the complete measurement range of piston errors. For large piston errors of the orders of a few tens of microns, we use a LASER source which has a very narrow band width of around 2nm. This provides a measurement range of 100μm. Further, to reduce the measurement range and improve the accuracy, we move on to the broad-band tungsten light source. A filter with a 10nm bandwidth and 650nm central wavelength provides a measurement range of 20μm. For the fine phasing measurements, a Johnson-Bessel-R filter with a central wavelength of 630nm and bandwidth of 120nm is used. It provides a measurement range of 1.6μm. With all three filters, multiple sets of experiments are performed; the results of these phasing experiments are discussed in the subsequent section. The parameters of the filters used and their measurement range are tabulated in Table 5.3.

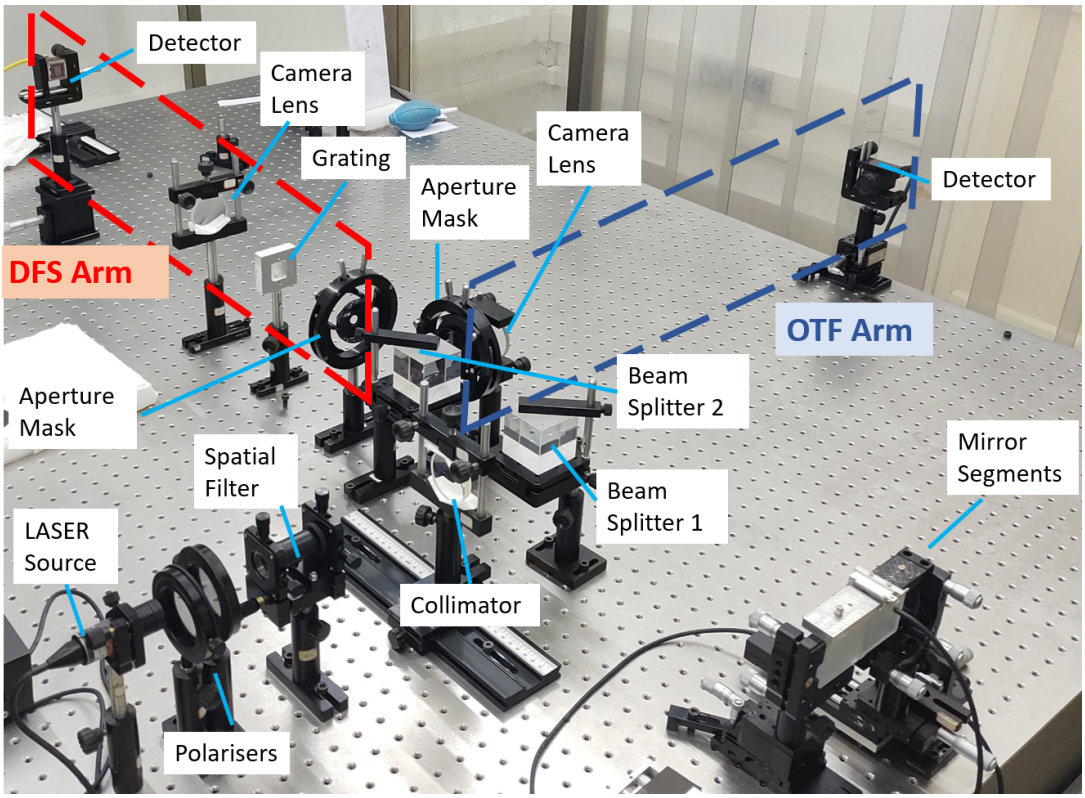

Figure 5.10: Laboratory experimentation setup for the OTF based phasing experiment.

Table 5.2: Details of the experimental setup

Parameter	Value
Source	Thorlabs Broad-band tungsten lamp and LASER (635 nm)
Point source	10micron pinhole
Collimator lens	150mm focal length achromatic doublet
Mirror segments	$\lambda/8$ surface quality Plane mirrors
Sampling aperture	6mm diameter, 12mm gap
Camera lens	750mm focal length achromatic doublet
Detector	3.45μm pixel size
Filters used	Narrow-band ($\lambda = 650$nm $\delta\lambda = 10$ nm)
	Johnson-Bessel-R ($\lambda = 630$nm $\delta\lambda = 120$nm)

Table 5.3: Band pass filters used for the OTF experiment

Filter	Central Wavelength (λ)	Band width ($\delta\lambda$)	Coherence length ($\lambda^2/2\delta\lambda$)
LASER	632nm	2nm	100μm
Narrow-band filter	650nm	10nm	21.25μm
Johnson-Bessel R filter	630nm	120nm	1.653μm

5.4.2 Experimentation Related Results

5.4.2.1 Piston Measurements with MTF

Before performing the experiment, it is important to estimate the measurement range of each filter by studying the variation of normalised MTF peak values against piston errors for the experimental setup. Therefore, using the simulations we first generate the PSFs as well as MTF for a large range of piston errors. This is done for each filter that we use in the experiment. The complete instrument response with the wavelength is considered in the simulations so that the calibration obtained is accurate. Further, the normalised MTF secondary peak values are plotted against corresponding piston errors (Figure 5.11).

Different methods can be adopted to convert the experimentally obtained MTF secondary peak values into piston errors. The most commonly used method is to use a Gaussian function derived from simulations (provided the wavelength-dependent throughput functions for all components are known precisely). Another more accurate method is to use an experimental calibration, where, we obtain the relation by fitting a higher-order polynomial to the normalised MTF secondary peaks obtained

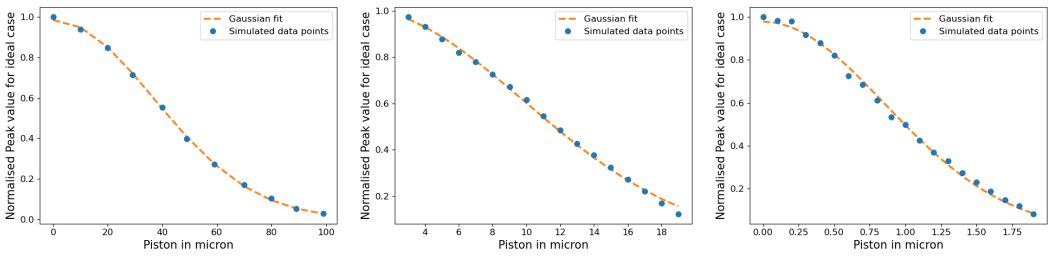

Figure 5.11: Variation of normalised MTF secondary peak values obtained from simulations for LASER (left), narrow-band filter (middle) and Johnson-Bessel R filter (right)

experimentally. We have tested with both the calibration schemes and finally used the polynomial fitting for our data to calibrate and extract the piston values.

For the normalisation, the peak values of the MTF must be known precisely for zero piston error. Our experimental setup has a provision for conducting experimentation on the DFS-based phase measurements (DFS arm shown in red color in Figure 5.10). So, we use DFS to identify the zero piston position for the mirror segments. The DFS technique is discussed in detail in chapter 4. At zero piston condition, the DFS fringes disappear entirely; hence, we get the continuous source spectrum. Thus, for each round of the experiment, before using the OTF, we first use the DFS fringe image to ensure the zero piston condition of the mirrors so that every time we start with the zero piston position and then apply a known piston error by moving one of the mirror segments. The experiment is conducted for three cases: (i) LASER, (ii) Narrow-band filter, and (iii) Johnson-Bessel R filter. For the LASER case, the piston is applied with a step size of 1μm; for narrow-band filter measurements, the step size is 500nm; and for the Johnson-Bessel R, a step size of 100nm is applied. By using an external high-precision optical encoder system, we ensure that the segment mounted on the linear actuator has indeed moved by the required amount of piston error that is introduced. At each position, 30 PSF images are recorded, these images are then Fourier transformed to get the MTF. Figure 5.12 shows an example of the experimentally recorded PSF image and its corresponding MTF obtained with a LASER source.

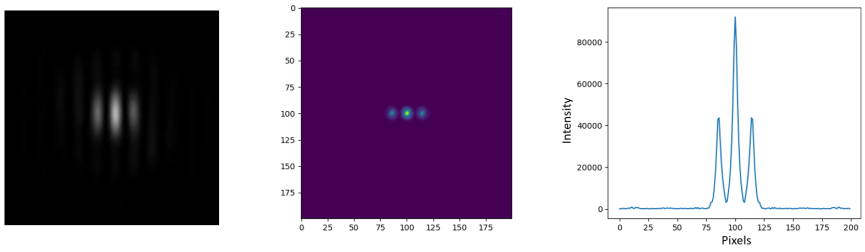

Figure 5.12: Experimentally observed PSF (left) and the corresponding MTF (middle) and the intensity plot of the MTF (right).

The MTF images are normalised with the secondary peak value of the first MTF image (zero piston). Then, the calibration curve is used to convert the obtained MTF peak values into corresponding piston values. Figure 5.13 shows an example of the variation of the experimental data for normalised MTF secondary peak values plotted against the applied piston values for the narrow-band filter. To have precise measurements, we fit a fourth-order polynomial to the obtained data set. Since we have multiple data sets for each filter, one data set is used for calibration. For the rest of the data sets, the same derived polynomial is used to convert the MTF secondary peak values into the corresponding piston.

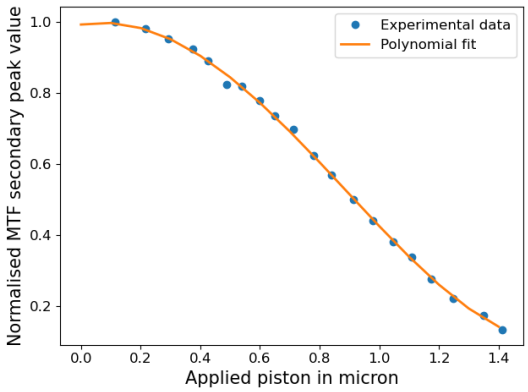

Figure 5.13: Variation of normalised MTF secondary peaks with applied piston values for experimental data for broad-band Johnson-Bessel-R filter and corresponding polynomial fit used for calibration.

The obtained piston value is compared against recorded encoder values to get measurement accuracy. The applied vs the measured piston values are plotted together, and a straight line is fitted onto the data. Figure 5.14 shows the plots for the applied vs. measured piston values; the red dashed line indicates a straight line fit. Ideally, the slope of this straight line should be one; the experimentally obtained slope values for each of these cases are tabulated in Table 5.4. Considering that the external optical encoder reads the applied piston error precisely, the scatter around the straight line can be attributed to the accuracy of the piston measurement. Table 5.4 gives the RMS values for each case. To ensure the repeatability of the experiment, the experiment was conducted multiple times; hence, the values given in Table 5.4 are the mean values of slope and RMS errors. From Table 5.4, it is clear that the measurement accuracy improves with the increasing bandwidth (and reducing measurement range) of the filter. Thus, the results confirm that by using different filters, very precise piston measurements can be carried out over a wide range (starting from a few microns, and then it can be reduced to a few tens of nanometers) using MTF. A similar practice is adopted at the Keck telescopes for broad-band phasing, where

a large bandwidth (200nm) filter is used to achieve the desired phasing accuracy of 30nm. Previously, using MTF, Simar, Stockman, and Surdej (2016) and Jiang and Zhao (2016) have reported piston measurement accuracy as good as ≈16nm, which is slightly better than ours (≈35nm). We believe that by using a larger bandwidth filter and by improving the experimental setup, the measurement accuracy can be even further improved for MTF-based measurements.

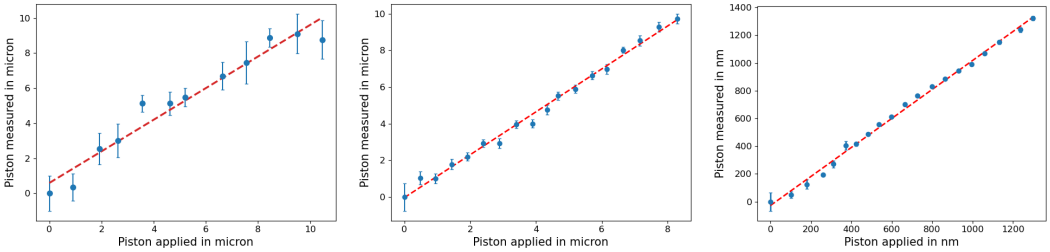

Figure 5.14: Plot showing experimentally measured piston values versus applied piston values with LASER source (left), Narrow-band filter (middle) and Johnson-Bessel R filter (right).

Table 5.4: Experimental results for the OTF-based phasing for piston measurements obtained using MTF

Filter used	Measurement Range	Fit Slope	RMS Error
LASER	$100\mu m$	0.9	700 nm
Narrow-band	$20\mu m$	1.17	328 nm
Johnson-Bessel R	$1.6\mu m$	1.096	35.145 nm

5.4.2.2 Piston Measurements with PTF

The MTF-based piston measurements gave a measurement accuracy of about 35nm with the Johnson-Bessel-R filter. However, the phasing requirement for the upcoming large telescopes is usually <10nm for diffraction-limited imaging. As discussed in subsection 5.3.3, our simulations suggest that PTF-based piston measurements can give an accuracy of <10 nm, hence for the same experimental data taken with Johnson-Bessel R filter, we now extract the piston using PTF for fine phasing. Figure 5.15 shows an example of the PTF of a PSF. It consists of three circular regions. The central region corresponds to zero phase, whereas the two side regions correspond to the two mirrors and hence show equal but opposite phase values. The wavefront phase map is obtained by taking any one of the circular regions on the side. The piston value is directly obtained from the circular phase map. The phase value is converted to piston by multiplying with $\lambda/4\pi$. The obtained piston values are then plotted against the applied piston values, where the 2π phase wrapping can be observed. On

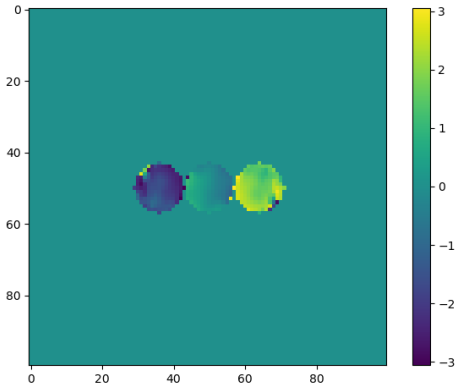

Figure 5.15: An example of the wavefront phase map (PTF) obtained from experimental data.

the observed data points, we fit the calculated cyclic piston values and obtain the RMS error for each cycle separately.

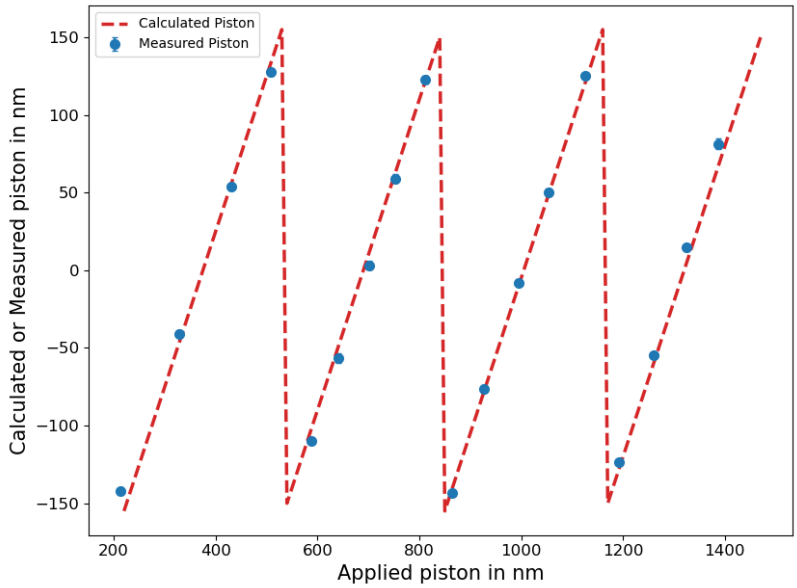

Figure 5.16: Experimental data showing the plot for applied vs measured piston values. The red dotted lines indicate the calculated piston values.

Figure 5.16 shows an example of the plot obtained for applied vs measured piston values. Here, we have four cycles; hence, we get four different values of RMS errors for each cycle. The experiment is repeated multiple times and Table 5.5 shows the RMS errors obtained for three best data sets.

Previously, Guerri et al. (2010) and (Baron et al., 2008) have reported a piston measurement accuracy of $\approx$ 11nm using PTF. For our experiments, we have achieved a piston measurement accuracy in the range of 1.5-18nm. This value can be further

Table 5.5: Experimental results for the OTF based phasing for piston measurements obtained using PTF (with Johnson-Bessel R filter)

Experiment Data set number	Cycle Number	RMS error	Mean RMS Error
Set 1	Cycle 1	8.022 nm	6.732 nm
	Cycle 2	6.434 nm	
	Cycle 3	2.644 nm	
	Cycle 4	9.831 nm	
Set 2	Cycle 1	1.460 nm	10.381 nm
	Cycle 2	17.881 nm	
	Cycle 3	11.802 nm	
Set 3	Cycle 1	10.419 nm	7.516 nm
	Cycle 2	4.213 nm	
	Cycle 3	6.188 nm	
	Cycle 4	4.005 nm	
	Cycle 5	5.659 nm	
	Cycle 6	14.611 nm	

improved by upgrading the experimental setup. For the current experimental setup, the actuator allows a minimum movement of 100nm; however, using a commercially available high-precision nano-actuator will allow us to have a larger number of data points in a single cycle, and hence we expect an improvement in the measurement accuracy.

5.5 Summary

In addition to the DFS, another phasing scheme we found very promising is based on the OTF. Again, through simulations, we first studied the use of OTF-based phasing under varying external conditions. The applicability of the MTF and PTF for coarse and fine phasing has also been studied through extensive simulations and laboratory experimentation. The experiment is performed with multiple filters so that a large range of piston errors can be covered. Initially, the MTF is used to extract the piston values, through which a measurement accuracy of 35nm is achieved. Whereas, from the PTF-based fine phasing scheme, we have achieved a piston measurement accuracy in the range of 1.5-18nm. The obtained accuracy values with our current setup are very promising and prove that OTF can be successfully used for coarse as well as fine piston measurements. We believe that upgrading the optical setup can further improve the phase measurement accuracy.

Chapter 6
Conclusion and Future Prospects

6.1 Summary

In today's era, segmented mirror technology has become a preferred choice for building large telescopes that enable higher resolution and sensitivity. Achieving the diffraction-limited resolution of these telescopes is only possible when their segments are aligned precisely. Several upcoming telescopes, such as the TMT, GMT, and ELT require alignment accuracy of sub-nanometers for high-contrast imaging applications such as direct imaging of exo-planets. Thus, developing high-precision wavefront sensing and control is an ongoing part of the research, and the APS is an inevitable part of it. Considering the India's upcoming large segmented mirror telescope, many technology development projects have been initiated at IIA. One critical aspect of the technology, which any segmented mirror telescope has to deal with, is linked to the precise alignment and phasing of its mirror segments. With the currently available schemes, the segment tip-tilt, focus, and phasing errors are measured using different techniques. Therefore, as a part of this thesis work, we have attempted to develop an efficient scheme that can be used to derive tip-tilt, defocus, and piston errors in one go with a relatively less complex instrument.

6.1.1 Chapter 2

We start with defining the alignment requirements for the proposed 10m class segmented telescope, working under seeing and diffraction-limited modes. From the ZEMAX analysis, we found that the tip-tilt error must be <0.03arc-sec for seeing-limited case, whereas, for diffraction-limited mode, it must be brought down to less than 0.01arc-sec. Similarly, for co-focusing, the ROC error must be less than 150μm for diffraction as well as seeing limited mode. The piston errors must be reduced down to less than 30nm for diffraction-limited imaging. Further, we have developed a very generic simulation code in Python, which is used to check the performance of

APS. The code can generate realistic images/spectra for any telescope + APS system. We have considered a SH wavefront sensor for the tip-tilt and defocus measurements, whereas, for phasing, we have chosen the DFS and OTF-based phasing schemes for our exploration. Using this simulation tool, we predicted the achievable values of tip-tilt, defocus, and piston measurement accuracies for the APS under realistic conditions. For a telescope working in the diffraction-limited regime, the desired co-aligning and co-focusing accuracy can be achieved using stars as faint as 15-16 magnitudes under good seeing conditions. Whereas for the seeing-limited mode, even fainter stars can provide the required accuracy.

6.1.2 Chapter 3

To get acquainted with the segmented mirror technology, a pilot project named PSMT has been initiated at IIA. It is a 1.3m size segmented telescope having seven hexagonal segments. The PSMT project is divided into two phases. Phase I, called the M1CS test-bed, aims to test the primary mirror control system. Whereas, in phase II (PSMT), a complete 1.3m aperture segmented mirror telescope is aimed to be developed. In both cases, we need to measure the segment tip-tilt and defocus errors precisely; therefore, as a part of this thesis work, we have designed and developed a SH sensor-based segment alignment device.

The SAD is designed to be used for the M1CS test-bed as well as for the PSMT. For the M1CS test-bed, the device will be placed at the ROC plane of the primary mirror, whereas for the PSMT, it will be placed at the Nasmyth focus of the telescope. The optical design and analysis of the device are done in ZEMAX, and only off-the-shelf components are used to minimise the cost. The device has two modes, the lenslet mode, and the imaging mode; the lenslet mode can be used for the fine tilt measurements using the SH spots, whereas the imaging mode uses a camera lens to get a single image, which can be used for coarse tilt measurements as well. Since the device has several electronic components, hence a custom-designed PSoC-based electronic controller is developed for controlling the LEDs, linear actuators, shutter as well as detector. Additionally, a Python-based GUI has also been developed to control all these operations remotely using the desktop and to analyse the SH spot images and get the segment tip-tilt and defocus errors.

After assembling the device, it has gone through extensive performance tests in the laboratory. The laboratory testing of the device is performed with a single segment of 10cm diameter, which will be used in the M1CS test-bed. Several experiments for tip-tilt and defocus measurements are performed, and the device is found to outperform. Although the device has performed exceptionally well in the laboratory environment, we expect there will be some degradation in the measurement accuracy when the device is used on-sky with the PSMT telescope.

6.1.3 Chapter 4

Phasing a segmented telescope to the required accuracy is one of the most challenging tasks of segmented mirror technology. Hence, the prime focus of this thesis is to explore several phasing schemes profoundly and identify one that can be suitably implemented on the proposed large telescope. We have started our exploration with the Dispersed Fringe Sensor (DFS) based phasing scheme. The DFS is a well studied phasing technique, conventionally used for coarse phasing (piston errors$> \lambda/4$) of mirror segments. In the presence of the piston error, the DFS gives fringed spectra. One can find the piston error by fitting the DFS equation on the intensity profile of the fringed spectra. However, for piston $< \lambda/4$, the fringe modulation nearly vanishes; hence, DFS cannot be used to measure very small piston errors. The recently developed DFA-LSR technique suggests that piston errors $< \lambda/4$ can also be measured using DFS. Instead of using the intensity along the dispersion direction, the DFA-LSR technique uses the intensity values perpendicular to the dispersion axis. This gives an intensity profile having three peaks. In the presence of piston errors, the ratio of the intensity of these peaks changes, and that can be related to piston error directly using a calibration constant. Under practical conditions, using our realistic simulations, we have tested the working of DFS for both coarse as well as fine phasing domains. We have also carried out extensive simulations to explore the effect of stellar brightness, atmospheric seeing, exposure time, aperture diameter, etc. on the performance of DFS-based phasing measurement. The simulations carried out using the DFA-LSR scheme suggest that a piston measurement accuracy of 6nm can be achieved with this method.

In order to verify our simulation results, we performed extensive laboratory experiments on the DFS. We start with the coarse phasing experiment, where a phasing accuracy of $< \lambda/2$ was achieved. Further experimentation was carried out to check the performance of the DFA-LSR-based fine phasing scheme. In the laboratory experiments, we measured the piston error as precisely as 2-3nm, which turned out to be the most accurate measurement ever done using the DFS phasing scheme.

Another experiment performed in the laboratory was to resolve the visibility issue with DFS, which arises when the inter-segment gap is not oriented along the direction of the grating groove. Since the mirror segments are hexagonal, the inter-segment gaps can have three possible orientations, at zero degree, $\pm 60°$. The change in orientation angle leads to a reduction in visibility; hence, simultaneous measurements of inter-segment edges are not possible. To resolve this issue, we tested the use of a Dove prism as a beam rotator. Using the Dove prism, the effect of misorientation of the inter-segment gap could be nullified, and hence, the fringe visibility can be restored even for $\pm 60°$ orientations. This was confirmed through our laboratory experiments.

Through realistic simulations complemented by laboratory experimentation, we

have demonstrated that DFS can be used for both coarse and fine phasing of mirror segments. However, one might face a few challenges while implementing this phasing technique on a real telescope. While dealing with the DFS scheme, we have identified a few limitations that must be addressed carefully to get the desired results on the telescope.

- DFS requires a large number of components, and hence, it might make the APS design complex when the complete telescope is considered.
- In order to implement DFS on the telescope, we must be able to measure the piston values of multiple inter-segment regions simultaneously. For this, DFS requires an array of prsims which is placed after the sub-aperture mask. The prism array deviates the beams from each inter-segment region into different directions. This ensures that the fringes formed by different inter-segment regions are well separated on the detector plane. This would increase the number of components significantly.
- A large detector would be required to measure all inter-segment regions simultaneously.
- The DFA-LSR technique is tested only in the laboratory, where it gives accuracy as good as 2-3nm. However, on-sky, the measurement accuracy might reduce due to several external factors such as SNR, atmospheric turbulence, telescope deformations, gravity, and wind effects.
- The use of Dove prism as a beam rotator for measuring multiple inter-segments simultaneously has been found to work well for coarse phasing case; however, for fine phasing where a single spectrum is present, we found that the visibility could not be retained.

6.1.4 Chapter 5

From our initial literature survey on segment phasing, in addition to DFS, we found the OTF-based phasing technique very promising. Therefore, we again utilized our Python-based simulation code to explore the OTF-based phasing scheme under realistic conditions. Similar to DFS, we studied the effects of stellar magnitude, exposure time, sampling aperture size, and atmospheric seeing on the MTF-based coarse piston measurements. The MTF-based phasing is best suited for coarse measurements; however, from our simulations, we have shown that, by successively using a set of different band-pass filters, one can improve the measurement accuracy, and the MTF-based phasing scheme itself can be used to phase the mirror segments with the required phasing accuracy (of less than 10nm). In addition to the MTF, fine phasing can be further improved with the help of PTF, which provides a very accurate measurement

of piston errors within 0 to $\lambda/4$ range. However, before switching from MTF to PTF-based phasing scheme, one needs to ensure that, by using an appropriate band-pass filter, the initially present large segment piston error has been brought down to the regime of $< \lambda/4$.

Since the PTF is found to be sensitive to both piston and tip-tilt errors, we have also conducted a simulation-based study in which the possible cross-talk between piston and tip-tilt measurements is explored. We found that when MTF is used for coarse piston measurement, the presence of segment tip-tilt error has a negligible effect on the accuracy of piston measurement. Whereas the fine phasing measurements, carried out using PTF, are found to be affected when segment tip-tilt errors are greater than 0.1arc-sec.

After performing an extensive simulation-based study on OTF-based phasing, we also performed laboratory experimentation on both coarse as well as fine phasing schemes. From the experimentation, we have demonstrated that using MTF, piston errors as large as tens to hundreds of microns can be measured with a sub-micron accuracy. We used three band-pass filters with different capture ranges and measurement accuracy. Using a large band-pass filter (Johnson R) with a small capture range, we have achieved a measurement accuracy of 35nm with the MTF scheme, which is good enough for diffraction-limited imaging. We have also used the PTF to extract the piston values from the same data set, and an accuracy of 1.5-18nm has been achieved. This measured accuracy is towards the lower side, and it can be improved further by upgrading the experimental setup.

Through our simulation and experimental studies, we have also identified a few limitations of the OTF-based phasing technique, which need to be considered while implementing this scheme on a segmented mirror telescope.

- Since the PTF is sensitive to wavefront errors, hence the inherent aberrations from the optical system need to be minimised before using this technique for alignment. Additionally, before performing the fine phasing measurements, the tip-tilt errors must be corrected.

- In order to measure piston errors from multiple inter-segment regions simultaneously, the placement of the sub-aperture mask is critical. It must be chosen such that the MTF secondary peaks from any two inter-segment regions do not overlap.

- Since the intensity of the MTF secondary peaks is used as a measure of the piston error, hence it is very important to maintain the source intensity uniformly throughout the measurements, as variations in the source intensity would modify the MTF secondary peaks, which would lead to erroneous measurements of piston error.

Based on our extensive simulations and experiments, we can compare the DFS and OTF-based phasing for their advantages and disadvantages. The Table 6.1 provides a comparison based on a few selected parameters that play an important role while implementing the technique on a realized telescope. For a better comparison, we have also included the two most robust phasing techniques used on the Keck telescope. We believe that OTF-based phasing is the best method because it provides both the desired measurement range and accuracy in a single observation, along with several advantages over other phasing schemes.

Table 6.1: Comparative analysis of DFS and OTF based phasing techniques based on our laboratory experiments. Shades of green colour indicate the advantages of the technique and orange colour indicate the limitations.

Phasing Technique	DFS	OTF	Keck Narrowband Phasing (Fine Phasing)	Keck Broadband Phasing (Coarse Phasing)
Source Type	Broad band source	Broad band with filters	Narrow-band	Broad band with filters
Number of components	Requires extra optical elements	No extra elements required	Requires extra optical elements	Requires extra optical elements
Measurement Range	100micron	100µm (depends on filter)	±λ/4	30µm
Measurement accuracy	2-3nm with DFA-LSR	1.5-18nm with PTF	6nm	30nm
Simultaneous measurements of multiple inter-segment regions	Requires extra optical elements	Possible (tested for maximum up to 37 segments)	Measures all intersegment regions simultaneously	Measures all intersegment regions simultaneously
Tip-tilt measurement capability	Not possible	Possible	Not Possible	Not Possible
Sensitivity to external disturbances *(based on our lab experiments)*	Least sensitive	Highly sensitive to source intensity fluctuations	Moderately sensitive to external vibrations	Moderately sensitive to external vibrations
Implementation on Segmented Mirror Telescope	Used on JWST for coarse phasing	Only few lab experiments conducted	Used on the Keck telescopes	Used on the Keck telescopes

Finally, through this thesis project, we have attempted to explore all three aspects of an APS using simulations and laboratory experimentation so that the knowledge and expertise gained can be implemented while developing the APS for India's upcoming Large Segmented Mirror Telescope.

6.2 Novelty of Thesis

This thesis has the following novel aspects:

- **Simulation code for generating the realistic images for any telescope + APS system:** A Python-based generic simulation code is developed, which is used to predict the achievable values of alignment accuracy under realistic conditions for varying external parameters.
- **Development of an Alignment device for the PSMT:** A SH sensor-based alignment device has been designed, developed, and tested through laboratory

experiments at IIA. The device will be used for the tip-tilt and defocus measurements of the PSMT.

- **Extensive experiments performed for fine phasing using DFS:** The DFA-LSR technique proposed by Li, Wang, and Rao (2017) and Li and Wang (2022) can be used for DFS-based fine piston measurements. This has been verified through our laboratory experiments, where we achieved an accuracy of 2-3nm.
- **Extensive experiments performed for phasing using OTF:** Piston measurement accuracy of 1.5-18nm has been achieved through the laboratory experiments for OTF-based phasing.
- **Use of single technique for coarse and fine phasing**: Existing telescopes use two different techniques for coarse and fine phasing of mirror segments. The above two experiments have shown that a single phasing technique can be used for coarse as well as fine phasing.

6.3 Future Scope

Through this work, we have tried to understand the co-alignment, co-focusing as well as co-phasing aspects of the APS through simulations and experiments. The Python-based simulation code currently considers most of the significant external sources of noise. However, it can be improved further by introducing the effects of gravity and wind-induced deformations, optical aberrations, and segment surface irregularities. An improved version of the code will help to understand the working of APS, especially in the fine phasing domain, where a precision of a few nanometers is required. The code can also be extended further to introduce higher-order Zernike terms on the segment so that not only tip-tilt and piston but also other surface aberrations of the segments can be studied.

We have performed extensive experiments on phasing for both DFS as well as OTF technique. The obtained results are very satisfactory. However, the experimental setup used is very crude. The results can be improved further by improving the experimental setup, mainly for the fine phasing experiments where nano-metric movement of the mirror is required. By using a high-precision piezo actuator, the values might show further improvement. While implementing the DFS practically on the telescope for fine piston measurements, an important parameter that can affect the measurement accuracy is the surface error of the mirror segment at the inter-segment region. Troy et al. (2018) have found that the Keck telescope segments can have RMS wavefront errors as large as 10nm in the inter-segment edge regions. This value might add a significant error to the DFS-based fine piston measurements. Hence, the

effect of edge errors and mirror reflectivity on DFS-based piston measurements can be studied through simulations.

Bibliography

Acton, D.S., Knight, J.S., Contos, A., Grimaldi, S., Terry, J., Lightsey, P., Barto, A., League, B., Dean, B., Smith, J.S., Bowers, C., Aronstein, D., Feinberg, L., Hayden, W., Comeau, T., Soummer, R., Elliott, E., Perrin, M., Starr, C.W.: 2012, Wavefront sensing and controls for the James Webb Space Telescope. In: Clampin, M.C., Fazio, G.G., MacEwen, H.A., Oschmann, J. Jacobus M. (eds.) *Space Telescopes and Instrumentation 2012: Optical, Infrared, and Millimeter Wave*, *Society of Photo-Optical Instrumentation Engineers (SPIE) Conference Series* **8442**, 84422H. DOI. ADS.

Acton, D.S., Knight, S., Carrasquilla, M., Weiser, N., Masciarelli, M., Jurczyk, S., Rapp, G., Mueckay, J., Wolf, E., Murphy, J., Carey, L., Coppock, E., Walker, C., Runnels, J., West, G., Wirth, G., Hicks, B., Melbourne, K., Gordon, M., Brown, B., Grimaldi, S., Sabatke, D., Wright, R., Coyle, L., Chonis, T., Whiteaker, K., Perrin, M., Comeau, T., Lajoie, C.-P., Hartig, G., Beck, T., Lallo, M., Regan, M., Telfer, R., Meléndez, M., Brady, G., Pueyo, L., Flagey, N., Kulp, B., Nelan, E., Brooks, K., Chayer, P., Osborne, S., Holfeltz, S., Sohn, T., Zielinski, T., Jurling, A., Bergkoetter, M., Bowers, C., Dean, B., Feinberg, L., Keski-Kuha, R., Kirk, J., McElwain, M.W., Howard, J.: 2022, Phasing the Webb Telescope. In: Coyle, L.E., Matsuura, S., Perrin, M.D. (eds.) *Space Telescopes and Instrumentation 2022: Optical, Infrared, and Millimeter Wave*, *Society of Photo-Optical Instrumentation Engineers (SPIE) Conference Series* **12180**, 121800U. DOI. ADS.

Alvarez, P., Rodríguez Espinosa, J.M., Sánchez, F.: 1998, The Gran Telescopio Canarias (GTC) project. *New Astronomy Reviews* **42**, 553. DOI. ADS.

Andersen, T., Ardeberg, A.L., Beckers, J., Goncharov, A., Owner-Petersen, M., Riewaldt, H., Snel, R., Walker, D.: 2003, The Euro50 Extremely Large Telescope. In: Angel, J.R.P., Gilmozzi, R. (eds.) *Future Giant Telescopes*, *Society of Photo-Optical Instrumentation Engineers (SPIE) Conference Series* **4840**, 214. DOI. ADS.

Anupama, G.C., Maheswar, G., Sriram, S., Sivarani, T., Parihar, P.S., Nagabhushan, S., Angchuk, D., Barway, S., Bhatt, B.C., Banyal, R., Basheer, A., Deshmukh, P., Divakar, D., Dorjai, T., Goswami, A., Govinda, K.V., Jorphail, S., Kamath, U.S., Kemkar, M.M., Mahay, T.T., Muneer, S., Muthumariappan, C., Ningombam, S.S., Pandey, G., Reddy, B.E., Sahu, D.K., Sandeep, D.S., Sethuram, R., Stalin, C.S., Subramanian, S., Tsewang, S., Subramaniam, A.: 2022, A 10-m class national large optical-IR telescope. *Journal of Astrophysics and Astronomy* **43**, 32. DOI. ADS.

Baron, F., Mocoeur, I., Cassaing, F., Mugnier, L.M.: 2008, Unambiguous phase retrieval as a cophasing sensor for phased array telescopes. *Journal of the Optical Society of America A* **25**, 1000. DOI. ADS.

Beckers, J.M., Ulich, B.L., Williams, J.T.: 1982, Performance of the Multiple Mirror Telescope (MMT). I - MMT The first of the advanced technology telescopes. In: Burbidge, G., Barr, L.D. (eds.) *International Conference on Advanced Technology Optical Telescopes*, *Society of Photo-Optical Instrumentation Engineers (SPIE) Conference Series* **332**, SPIE, 2. DOI. ADS.

Bely, P.Y.: 2003, *The Design and Construction of Large Optical Telescopes*, springer. DOI. ADS.

Bhattacharyya, J.C., Rajan, K.T.: 1992, Vainu Bappu Telescope. *Bulletin of the Astronomical Society of India* **20**, 319. ADS.

Bonoli, F.: 2018, Guido Horn d'Arturo and the first multi-mirror telescopes: 1932-1952 . *Mem. Soc. Astron. Italiana* **89**, 448. ADS.

Bradley, L., Sipőcz, B., Robitaille, T., Tollerud, E., Vinícius, Z., Deil, C., Barbary, K., Wilson, T.J., Busko, I., Günther, H.M., Cara, M., Conseil, S., Bostroem, A., Droettboom, M., Bray, E.M., Andersen Bratholm, L., Lim, P.L., Barentsen, G., Craig, M., Rathi, S., Pascual, S., Perren, G., Donath, A., Georgiev, I.Y., De Val-Borro, M., Kerzendorf, W., Bach, Y.P., Quint, B., Souchereau, H., Weaver, B.A.: 2021, astropy/photutils: 1.0.2, Zenodo. DOI.

Buckley, D.A.H., Charles, P.A., Nordsieck, K.H., O'Donoghue, D.: 2006, The Southern African Large Telescope project. In: Whitelock, P., Dennefeld, M., Leibundgut, B. (eds.) *The Scientific Requirements for Extremely Large Telescopes*, *IAU Symposium* **232**, 1. DOI. ADS.

Buous, S., Menzies, J., Gajjar, H.: 2008, SALT segmented primary mirror: commissioning capacitive edge sensing system and performance comparison with inductive sensor. In: Stepp, L.M., Gilmozzi, R. (eds.) *Ground-based and Airborne Telescopes II* **7012**, SPIE, 70123G. International Society for Optics and Photonics. DOI. URL.

Castro, J., Rosado, M., Siegel, B., Cardell, A., Pérez, A., Prieto, G.: 2024, COALA: a diurnal alignment and phasing instrument for GTC. In: Marshall, H.K., Spyromilio, J., Usuda, T. (eds.) *Ground-based and Airborne Telescopes X* **13094**, SPIE, 1309421. International Society for Optics and Photonics. DOI. URL.

Chanan, G., Troy, M.: 2018, Chromatic effects in narrowband phasing of the Keck Telescope segments: theory and numerical simulations. In: Marshall, H.K., Spyromilio, J. (eds.) *Ground-based and Airborne Telescopes VII*, *Society of Photo-Optical Instrumentation Engineers (SPIE) Conference Series* **10700**, 107001E. DOI. ADS.

Chanan, G.A., Nelson, J.E., Mast, T.S.: 1986, Segment alignment for the Keck Telescope primary mirror. In: *Advanced technology optical telescopes III* **Vol. 628**, 466. DOI.

Chanan, G., Ohara, C., Troy, M.: 2000, Phasing the Mirror Segments of the Keck Telescopes II: The Narrow-band Phasing Algorithm. *Applied Optics* **Vol. 39**, 4706. DOI.

Chanan, G.A., Nelson, J.E., Mast, T.S., Wizinowich, P.L., Schaefer, B.A.: 1994, W.M. Keck Telescope phasing camera system. In: Crawford, D.L., Craine, E.R. (eds.) *Instrumentation in Astronomy VIII*, *Society of Photo-Optical Instrumentation Engineers (SPIE) Conference Series* **2198**, 1139. DOI. ADS.

Chanan, G., Troy, M., Dekens, F., Michaels, S., Nelson, J., Mast, T., Kirkman, D.: 1998, Phasing the Mirror Segments of the Keck Telescopes: The Broadband Phasing Algorithm. *Applied Optics* **37**, 140. DOI. ADS.

Cubalchini, R.: 1979, Modal wave-front estimation from phase derivative measurements. *Journal of the Optical Society of America (1917-1983)* **69**, 972. ADS.

Cui, X., Su, D.-Q., Wang, Y.-N., Li, G., Liu, G., Zhang, Y., Li, Y.: 2010, The optical performance of LAMOST telescope. In: Stepp, L.M., Gilmozzi, R., Hall, H.J. (eds.) *Ground-based and Airborne Telescopes III*, *Society of Photo-Optical Instrumentation Engineers (SPIE) Conference Series* **7733**, 773309. DOI. ADS.

Dean, B.H., Aronstein, D.L., Smith, J.S., Shiri, R., Acton, D.S.: 2006, Phase retrieval algorithm for JWST Flight and Testbed Telescope. In: Mather, J.C., MacEwen, H.A., de Graauw, M.W.M. (eds.) *Space Telescopes and Instrumentation I: Optical, Infrared, and Millimeter*, *Society of Photo-Optical Instrumentation Engineers (SPIE) Conference Series* **6265**, 626511. DOI. ADS.

Deshmukh, P., Parihar, P., Mishra, D.S., Prakash, A., Kemkar, P.M.M.: 2016, A soft actuator for Prototype Segmented Mirror Telescope. In: Navarro, R., Burge, J.H. (eds.) *Advances in Optical and Mechanical Technologies for Telescopes and Instrumentation II* **9912**, SPIE, 991207. International Society for Optics and Photonics. DOI. URL.

Deshmukh, P.G., Mandal, A., Parihar, P.S., Nayak, D., Mishra, D.S.: 2018, Design, development, and validation of a segment support actuator for the prototype segmented mirror telescope. *Journal of Astronomical Telescopes, Instruments, and Systems* **4**, 014005. DOI. ADS.

Deshmukh, P., S., S., Chand, T., Kambhala, S., S., R., Joshi, R., Kumar, Y.B., Muthhar, M.: 2024, Design and simulation of 6.2m wide-field telescope for spectroscopic survey. In: Marshall, H.K., Spyromilio, J., Usuda, T. (eds.) *Ground-based and Airborne Telescopes X* **13094**, SPIE, 130941V. International Society for Optics and Photonics. DOI. URL.

Dharmadhikari, R., Parihar, P.: 2024, Simulation and experimental study of the OTF based alignment and phasing of segmented mirrors. In: Marshall, H.K., Spyromilio, J., Usuda, T. (eds.) *Ground-based and Airborne Telescopes X* **13094**, SPIE, 1309427. International Society for Optics and Photonics. DOI. URL.

Dharmadhikari, R., Parihar, P., Jacob, A.: 2023, Building a large affordable optical-NIR telescope (I): an alternate way to handle segmented primary mirror. *Experimental Astronomy* **56**, 569. DOI. ADS.

Dharmadhikari, R., Parihar, P., Ahmed, M.M.R., Venkatapathaiah, G.K., Kemkar, M.M., Kunjam, H.: 2024, Development of an alignment device for the Prototype Segmented Mirror

Telescope. *Journal of Astronomical Telescopes, Instruments, and Systems* **10**, 019002. DOI. ADS.

Dierickx, P., Beckers, J.-L., Brunetto, E., Conan, R., Fedrigo, E., Gilmozzi, R., Hubin, N.N., Koch, F., Le Louarn, M., Marchetti, E., Monnet, G.J., Noethe, L., Quattri, M., Sarazin, M.S., Spyromilio, J., Yaitskova, N.: 2003, The eye of the beholder: designing the OWL. In: Angel, J.R.P., Gilmozzi, R. (eds.) *Future Giant Telescopes*, *Society of Photo-Optical Instrumentation Engineers (SPIE) Conference Series* **4840**, 151. DOI. ADS.

El Hadi, K., Sauvage, J.-F., Dohlen, K., Fusco, T., Neichel, B., Marchis, F., N'Diaye, M.: 2016, Pupil phase discontinuity measurement: comparison of different wavefront sensing concepts. In: Marchetti, E., Close, L.M., Véran, J.-P. (eds.) *Adaptive Optics Systems V*, *Society of Photo-Optical Instrumentation Engineers (SPIE) Conference Series* **9909**, 990967. DOI. ADS.

Esposito, S., Devaney, N.: 2002, Segmented telescopes co-phasing using Pyramid Sensor. In: *European Southern Observatory Conference and Workshop Proceedings*, *European Southern Observatory Conference and Workshop Proceedings* **58**, 161. ADS.

Esposito, S., Pinna, E., Puglisi, A., Tozzi, A., Stefanini, P.: 2005, Pyramid sensor for segmented mirror alignment. *Optics Letters* **30**, 2572. DOI. ADS.

Gajjar, H., Menzies, J., Swiegers, J., Rozière, D., Courteville, A., Buous, S., Luong, B.: 2006, Results from the capacitive edge sensing system for the active alignment of the SALT primary mirror. In: Stepp, L.M. (ed.) *Ground-based and Airborne Telescopes* **6267**, SPIE, 626737. International Society for Optics and Photonics. DOI. URL.

Gilmozzi, R., Spyromilio, J.: 2008, The 42m European ELT: status. In: Stepp, L.M., Gilmozzi, R. (eds.) *Ground-based and Airborne Telescopes II*, *Society of Photo-Optical Instrumentation Engineers (SPIE) Conference Series* **7012**, 701219. DOI. ADS.

Gonsalves, R.A.: 1976, Phase retrieval from modulus data. *Journal of the Optical Society of America (1917-1983)* **66**, 961. DOI. ADS.

Guerri, G., Roose, S., Stockman, Y., Mazzoli, A., Surdej, J., Defise, J.-M.: 2010, First steps in the development of a piston sensor for large aperture space telescopes. In: Oschmann, J. Jacobus M., Clampin, M.C., MacEwen, H.A. (eds.) *Space Telescopes and Instrumentation 2010: Optical, Infrared, and Millimeter Wave*, *Society of Photo-Optical Instrumentation Engineers (SPIE) Conference Series* **7731**, 773154. DOI. ADS.

Gutiérrez, C.M., Torres, M., Oria, A., Fernández-Valdivia, J.J., Arnold, D., Copley, D., Copperwheat, C., de Cos Juez, J., Franco, A., Fan, Y., García Piñero, A., Harvey, E., Jermak, H., Jiang, X., Knapen, J.H., McGrath, A., Ranjbar, A., Rebolo, R., Smith, R., Steele, I.A., Wang, Z., Wu, X., Xu, D., Xue, S., Yuan, W., Zheng, Y.: 2021, The 4 m New Robotic Telescope Project: An Updated Report. In: *Revista Mexicana de Astronomia y Astrofisica Conference Series*, *Revista Mexicana de Astronomia y Astrofisica Conference Series* **53**, 8. DOI. ADS.

Hasan, S.S.: 2014, In: Padmanabhan, T. (ed.) *Growth of Optical Astronomy in India*, Springer India, New Delhi, 111. ISBN 978-81-8489-998-6. DOI. URL.

Jacob, A., Parihar, P., James, M.K.: 2020, Creating a large aspheric primary mirror using spherical segments. *Experimental Astronomy* **50**, 51. DOI. ADS.

Jacob, A., Parihar, P., Divakaran, S., James, M.K.: 2018, Aligning and phasing segmented mirror telescope with the pyramid sensor. In: Marshall, H.K., Spyromilio, J. (eds.) *Ground-based and Airborne Telescopes VII*, *Society of Photo-Optical Instrumentation Engineers (SPIE) Conference Series* **10700**, 107001G. DOI. ADS.

Jiang, J., Zhao, W.: 2016, Phasing piston error in segmented telescopes. *Optics Express* **24**, 19123. DOI. ADS.

Johns, M.: 2006, The Giant Magellan Telescope (GMT). In: Stepp, L.M. (ed.) *Ground-based and Airborne Telescopes*, *Society of Photo-Optical Instrumentation Engineers (SPIE) Conference Series* **6267**, 626729. DOI. ADS.

Kopon, D., McLeod, B., van Dam, M.A., Bouchez, A., McCracken, K., Catropa, D., Podgorski, W., McMuldroch, S., Conder, A., Close, L., Males, J., Morzinski, K., Norton, T.: 2016, On-sky demonstration of the GMT dispersed fringe phasing sensor prototype on the Magellan Telescope. In: Marchetti, E., Close, L.M., Véran, J.-P. (eds.) *Adaptive Optics Systems V*, *Society of Photo-Optical Instrumentation Engineers (SPIE) Conference Series* **9909**, 990946. DOI. ADS.

Kumar, M.S., Narayanamurthy, C.S., Kumar, A.S.K.: 2013, Focal length measurement of microlens array for Shack-Hartmann wavefront sensor using interferometer. *Optical Engineering* **52**, 124103. DOI. ADS.

Kurita, M., Kino, M., Iwamuro, F., Ohta, K., Nogami, D., Izumiura, H., Yoshida, M., Matsubayashi, K., Kuroda, D., Nakatani, Y., Yamamoto, K., Tsutsui, H., Iribe, M., Jikuya, I., Ohtani, H., Shibata, K., Takahashi, K., Tokoro, H., Maihara, T., Nagata, T.: 2020, The Seimei telescope project and technical developments. *Pub. Astron. Soc. Japan* **72**, 48. DOI. ADS.

Li, Y., Wang, S.: 2022, Robust dispersed fringe sensing for all-stage cophasing. *Optics and Lasers in Engineering* **159**, 107187. DOI. ADS.

Li, Y., Wang, S., Rao, C.: 2017, Dispersed-fringe-accumulation-based left-subtract-right method for fine co-phasing of a dispersed fringe sensor. *Applied Optics* **Vol. 56**, 4267. DOI.

Mahajan, V.N.: 2013, *Optical imaging and aberrations, part III: wavefront analysis*, SPIE. ADS.

Mahajan, V.: 2013, Optical Imaging and Aberrations, Part III: Wavefront Analysis (SPIE, 2013), Vol. *PM221*, 88.

Nagata, T., Kurita, M.: 2020, Seimei 3.8-m Telescope has been commissioned. In: Marshall, H.K., Spyromilio, J., Usuda, T. (eds.) *Ground-based and Airborne Telescopes VIII*, *Society of Photo-Optical Instrumentation Engineers (SPIE) Conference Series* **11445**, 114451T. DOI. ADS.

Nelson, J., Sanders, G.H.: 2006, TMT status report. In: Stepp, L.M. (ed.) *Ground-based and Airborne Telescopes*, *Society of Photo-Optical Instrumentation Engineers (SPIE) Conference Series* **6267**, 626728. DOI. ADS.

Nelson, J.E., Mast, T.S., Faber, S.M., of California, U., of Technology, C.I.: 1985, *The Design of the Keck Observatory and Telescope*, Caltech.

Orlov, V.G., Cuevas, S., Garfias, F., Voitsekhovich, V.V., Sanchez, L.J.: 2000, Co-phasing of segmented mirror telescopes with curvature sensing. In: Sebring, T.A., Andersen, T. (eds.) *Telescope Structures, Enclosures, Controls, Assembly/Integration/Validation, and Commissioning*, *Society of Photo-Optical Instrumentation Engineers (SPIE) Conference Series* **4004**, 540. DOI. ADS.

Oswalt, T.D., McLean, I.S.: 2013, *Planets, Stars and Stellar Systems, Volume 1: Telescopes and Instrumentation*, Springer. DOI. ADS.

Palunas, P., MacQueen, P.J., Booth, J.A., Calder, R., Fowler, J.R., Shetrone, M.D., Odewahn, S.C., Segura, P., Wesley, G.L., Damm, G., Martin, J., Odoms, P.S.: 2006, Imaging performance of the Hobby-Eberly Telescope. In: Stepp, L.M. (ed.) *Ground-based and Airborne Telescopes* **6267**, SPIE, 62673V. International Society for Optics and Photonics. DOI. URL.

Parihar, P., Deshmukh, P., Jacob, A., Kumar, V., Goudar, A., Sriram, S., Nagabhusan, S., Amitkumar, S., Govinda, K.V., Sandeep, D.S., Kemkar, P.M.M., Anupama, G.C.: 2018, Prototype segmented mirror telescope: a pathfinder of India's Large Optical-NIR telescope project. In: Marshall, H.K., Spyromilio, J. (eds.) *Ground-based and Airborne Telescopes VII*, *Society of Photo-Optical Instrumentation Engineers (SPIE) Conference Series* **10700**, 107001A. DOI. ADS.

Pizarro, C., Arasa, J., Laguarta, F., Tomas, N., Pinto, A.: 2002, Design of an interferometric system for the measurement of phasing errors in segmented mirrors. *Applied Optics* **41**, 4562. DOI. ADS.

Ragland, S., Gers, L.: 2022, A phase retrieval technique to measure and correct residual segment piston errors of large aperture optical telescopes. In: Marshall, H.K., Spyromilio, J., Usuda, T. (eds.) *Ground-based and Airborne Telescopes IX*, *Society of Photo-Optical Instrumentation Engineers (SPIE) Conference Series* **12182**, 1218209. DOI. ADS.

Ramsey, L.W., Adams, M.T., Barnes, T.G., Booth, J.A., Cornell, M.E., Fowler, J.R., Gaffney, N.I., Glaspey, J.W., Good, J.M., Hill, G.J., Kelton, P.W., Krabbendam, V.L., Long, L., MacQueen, P.J., Ray, F.B., Ricklefs, R.L., Sage, J., Sebring, T.A., Spiesman, W.J., Steiner, M.: 1998, Early performance and present status of the Hobby-Eberly Telescope. In: Stepp, L.M. (ed.) *Advanced Technology Optical/IR Telescopes VI*, *Society of Photo-Optical Instrumentation Engineers (SPIE) Conference Series* **3352**, 34. DOI. ADS.

Schroeder, D.J.: 1987, *Astronomical optics*, Science Direct. ADS.

Sharma, T.K., Parihar, P., Banyal, R.K., Dar, A.A., Kemkar, P.M.M., Stanzin, U., Anupama, G.C.: 2017, An automated extinction and sky brightness monitor for the Indian Astronomical Observatory, Hanle. *Mon. Not. Roy. Astron. Soc.* **470**, 1091. DOI. ADS.

Shi, F., Redding, D., Lowman, A., Basinger, S., Bowyers, C., Davila, P., Wilson, M., Norton, T., Boucarut, R., Petrone, P.: 2000, DCATT Dispersed Fringe Sensor: Modeling and Experimenting with the Transmissive Phase Plates. In: Smith, E., Long, K. (eds.) *Next Generation Space Telescope Science and Technology*, *Astronomical Society of the Pacific Conference Series* **207**, 510. ADS.

Shi, F., Redding, D.C., Lowman, A.E., Bowers, C.W., Burns, L.A., Petrone, I. Peter, Ohara, C.M., Basinger, S.A.: 2003, Segmented mirror coarse phasing with a dispersed fringe sensor: experiments on NGST's Wavefront Control Testbed. In: Mather, J.C. (ed.) *IR Space Telescopes and Instruments*, *Society of Photo-Optical Instrumentation Engineers (SPIE) Conference Series* **4850**, 318. DOI. ADS.

Shi, F., Chanan, G., Ohara, C., Troy, M., Redding, D.C.: 2004a, Experimental Verification of Dispersed Fringe Sensing as a Segment Phasing Technique using the Keck Telescope. *Applied Optics* **Vol. 43**, 4474. DOI.

Shi, F., Redding, D.C., Green, J.J., Ohara, C.M.: 2004b, Performance of segmented mirror coarse phasing with a dispersed fringe sensor: modeling and simulations. In: *Optical, Infrared, and Millimeter Space Telescopes* **Vol. 5487**, 897. DOI.

Simar, J.F., Stockman, Y., Surdej, J.: 2015, Single-wavelength coarse phasing in segmented telescopes. *Applied Optics* **54**, 1118. DOI. ADS.

Simar, J.F., Stockman, Y., Surdej, J.: 2016, Smart co-phasing system for segmented mirror telescopes. In: Hall, H.J., Gilmozzi, R., Marshall, H.K. (eds.) *Ground-based and Airborne Telescopes VI*, *Society of Photo-Optical Instrumentation Engineers (SPIE) Conference Series* **9906**, 99065F. DOI. ADS.

Smith, E.H., Vasudevan, G., Reardon, R.D., Bernier, R., Triebes, K.J.: 2003, Coarse phasing of a segmented mirror using a dispersed fringe sensor. In: *IR Space Telescopes and Instruments*, *SPIE Conf Series* **4850**, 469. DOI.

Surdej, I., Yaitskova, N., Gonte, F.: 2010, On-sky performance of the Zernike phase contrast sensor for the phasing of segmented telescopes. *Applied Optics* **49**, 4052. DOI. ADS.

Surendran, A., Parihar, P.S., Banyal, R.K., Kalyaan, A.: 2018, Development of a Lunar Scintillometer as part of the national large optical telescope site survey. *Experimental Astronomy* **45**, 57. DOI. ADS.

Tokovinin, A.: 2001, AO tutorial at CTIO.

Townson, M.J., Farley, O.J.D., Orban de Xivry, G., Osborn, J., Reeves, A.P.: 2019, AOtools: Adaptive optics modeling and analysis toolkit. ADS.

Troy, M., Chanan, G., Colavita, M., Martinek, S.J.: 2018, Interferometric characterization of Keck segment edge errors. In: Marshall, H.K., Spyromilio, J. (eds.) *Ground-based and Airborne Telescopes VII*, *Society of Photo-Optical Instrumentation Engineers (SPIE) Conference Series* **10700**, 107000M. DOI. ADS.

Voitsekhovich, V.V., Bara, S., Orlov, V.G.: 2002, Co-phasing of segmented telescopes: A new approach to piston measurements. I. Optical concept. *Astron. Astrophys.* **382**, 746. DOI. ADS.

Wang, S., Zhu, Q., Cao, G.: 2009, Dispersed Rayleigh interferometer. In: *4th International Symposium on Advanced Optical Manufacturing and Testing Technologies: Optical Test and Measurement Technology and Equipment* **Vol. 7283**. DOI.

Wirth, A., Gonsiorowski, T., Roberts, J., Bruno, T.L., Swiegers, J., Gajjar, H., Swat, A.: 2004, Developing and testing an optical alignment system for SALT"s segmented primary mirror. In: *Ground-based Telescopes* **Vol. 5489**, 892. DOI.

Wolf, M.J., Palunas, P., Booth, J.A., Ward, M.H., Wirth, A., Wesley, G.L., O'Donoghue, D., Ramsey, L.W.: 2003, Mirror Alignment Recovery System (MARS) on the Hobby-Eberly Telescope. In: Oschmann, J.M., Stepp, L.M. (eds.) *Large Ground-based Telescopes*, *Society of Photo-Optical Instrumentation Engineers (SPIE) Conference Series* **4837**, 714. DOI. ADS.

Yu, D., Zhao, W.: 2018, Phasing error detection for segmented telescopes. In: Wang, Y., Kidger, T.E., Tatsuno, K. (eds.) *Optical Design and Testing VIII*, *Society of Photo-Optical Instrumentation Engineers (SPIE) Conference Series* **10815**, 108150G. DOI. ADS.

Zhang, L., Zhao, W., Zhao, Y., Liu, J., Chu, C.: 2023, Non-redundant MTF distribution method for sensing multi-piston simultaneously in segmented telescopes. *Optics Communications* **530**, 129182. DOI. ADS.

Zhang, Y., Xian, H.: 2020, Coarse co-phasing method based on slope of visibility-enhanced dispersed fringe pattern for segmented telescope. *Optics Communications* **459**, 124998. DOI. ADS.

Zhang, Y., Liu, G.-R., Wang, Y.-F., Li, Y.-P., Zhang, Y.-J., Zhang, L., Zeng, Y.-Z., Zhang, J.: 2011, An experimental indoor phasing system based on active optics using dispersed Hartmann sensing technology in the visible waveband. *Research in Astronomy and Astrophysics* **11**, 1111. DOI. ADS.

Zhao, W., Cao, G.: 2011, Active cophasing and aligning testbed with segmented mirrors. *Optics Express* **Vol. 19**, 8670. DOI.

Zhao, W., Zeng, Q.: 2017, Simultaneous multi-piston measurement method in segmented telescopes. *Optics Express* **25**, 24540. DOI. ADS.